RICHTMYER–MESHKOV INSTABILITY OF SHOCK-INDUCED DOUBLE-LAYER GAS CYLINDERS

XIN LI

PhD

The Hong Kong Polytechnic University

2025

The Hong Kong Polytechnic University

Department of Aeronautical and Aviation Engineering

Richtmyer–Meshkov Instability of Shock-induced Double-layer Gas Cylinders

Xin Li

A thesis submitted in partial fulfilment of the requirements
for the degree of Doctor of Philosophy

June 2025

CERTIFICATE OF ORIGINALITY

I hereby declare that this thesis is my own work and that, to the best of my knowledge and belief, it reproduces no material previously published or written, nor material that has been accepted for the award of any other degree or diploma, except where due acknowledgement has been made in the text.

_____(Signed)

____Xin Li___ (Name of student)

Abstract

Richtmyer-Meshkov (RM) instability arises due to the baroclinic and pressure perturbation mechanisms when a perturbed density interface is impulsively accelerated. The perturbation on the interface will result in the generation of secondary instabilities and the formation of massive small-scale vortices, which in turn cause turbulent mixing. RM instability in inert and reactive gas mixture finds widespread applications in various engineering fields, including dust cloud explosions, scramjet engines and multiphase combustion in propulsion systems.

The evolution of an inert double-layer gas cylinder under various Mach numbers and Atwood numbers is studied numerically. Regarding the effects of varying Mach numbers (M = 1.27, 1.5, 1.7, and 2.1), a bulge is generated near the upstream pole of the outer cylinder due to the impingement of a reflected shock wave, which promotes the formation of an upstream jet for $M \geq 1.5$. At a higher Mach number, the evolution of the jet is suppressed under the influence of a higher pressure upstream of the jet head. The compressibility effects are quantified by the widths and heights of the gas cylinders. The mechanism behind vorticity evolution is investigated using the vorticity transport equation. The dilatation and baroclinic terms play a dominant role in the dynamics of vorticity production. Higher Mach numbers amplify the dilatation, baroclinic and viscosity terms, thereby promoting the development of RM instability. In terms of Atwood number effects, two types of gas layer configurations are considered: an A/B/A-type gas layer (where the densities in the surroundings, gas ring, and inner cylinder are denoted as A, B, and A) and an A/B/C-type gas layer (where the densities in the surroundings, gas ring, and inner cylinder are denoted as A, B, and C). The Atwood number is associated with nonlinear acoustic effects, and the sign of A results in a significant variation in the wave patterns. For the scenarios of A/B/A-type gas layer (A_1 = 0.50, 0.39, 0.19, and −0.20, where A_1 is the Atwood number for the first layer), the development of vortex pairs slows down with the decreasing Atwood numbers when $A_1 > 0$. The widths and heights of the outer and inner cylinders keep steady at a later phase of the evolution. Vortex pairs emerge and propagate in both upstream and downstream directions from the outer interface for $A_1 = -0.20$. For the scenarios of A/B/C-type gas layer (A_2 = −0.50, −0.25, −0.06, 0.06 and 0.17, where A_2 is the Atwood number for the second layer), secondary vortex pairs emerge at the downstream interface of the outer cylinder following the interaction of a high-pressure triple point with the downstream interface, while a downstream jet is formed due to

the generation of a notably higher-pressure zone after the transmitted shock wave traverses the convergence point when $A_2 < 0$. Higher Atwood numbers amplify the dilatation, baroclinic and viscosity terms and induce RM instability for $A_1 > 0$, while the increase in the magnitude of the Atwood number in the inner gas cylinder primarily enhances vorticity transport during the stage when the first transmitted shock passes through the inner cylinder. The net circulation can be predicted by the linear superposition of Samtaney and Zabusky (SZ) and Picone and Boris (PB) models. Analysis of the mean mass fraction histories of the outer and inner cylinders shows that increased mixing of ambient gas into the gas ring leads to the dilution of SF_6 and promotes gas mixing as the Mach number and the magnitude of Atwood number rises, especially when the incident shock wave passes over the gas cylinder.

The evolution of a reactive double-layer gas cylinder under various Mach numbers and radius ratios is studied numerically. Regarding the effects of varying Mach numbers (M = 2.13, 2.3,2.5 and 2.9), a deflagration wave is initiated, propagating at subsonic speed and reaching the UI_1 in the long-term evolution at Mach 2.13. As the Mach number increases, the ignition time occurs earlier, followed by a detonation wave. The incident shock wave ignites the gas mixture at the upstream pole of the outer cylinder at higher Mach numbers. The distributions of pressure, temperature, and hydrogen mass fraction at the reaction front suggest that deflagration-to-detonation transition (DDT) occurs after ignition at Mach numbers of 2.3 and 2.5. The evolution of the gas cylinder is analyzed quantitatively by evaluating the transverse bubble diameter and bubble area. Combustion completeness is used to quantitatively describe the ignition process. Regarding the molecular mixing fraction, the slope of curves in the inert scenarios rises with increasing Mach numbers, as stronger shock intensities enhance vorticity production and accelerate the growth of RM instability. The reactive scenarios exhibit different behaviours, where the mixing fraction is generally suppressed due to vortex cancellation. Regarding the effects of varying radius ratios (λ = 0.25, 0.5 and 0.75), a hot spot forms near the downstream interface of the outer cylinder due to high pressure and temperature from the triple point. When λ increases to 0.75, a second hot spot appears near the upstream interface of the inner cylinder. The distribution of pressure, temperature, and hydrogen mass fraction at the reaction front indicates that DDT occurs after the generation of the first hot spot. Following the second hot spot, a detonation wave propagates upstream towards the outer interface. Intense heat release following ignition causes an expansion in the outer diameter and the area of the gas ring, while compressing the inner diameter and inner gas area. Detonation results in a more rapid increase in combustion completeness compared to deflagration, which quantifies the ignition process. Regarding

vorticity and mixing fraction, the magnitude of net vorticity decreases, and its rate of decrease slows after ignition as the radius ratio increases. Additionally, the mixing fraction for the outer interface increases with increasing radius ratios in both reactive and inert gas cylinders but remains lower in reactive cylinders compared to inert counterpart after ignition.

List of Publications

Journal articles:

[1] **Li, X.**, Hao, J., Wen, C. Y., & Fan, E. (2024). "Effects of Mach and Atwood numbers on the shock-induced evolution of a double-layer gas cylinder." *Physics of Fluids*, *36*(2).

[2] **Li, X.**, Hao, J., Wen, C. Y., & Fan, E. (2024). "Role of Atwood number in the shock-induced evolution of a double-layer gas cylinder. " *Physics of Fluids*, *36*(8).

[3] **Li, X.**, Hao, J., Fan, E., Uy, K. C. K., Shao, X., & Wen, C. Y. (2025). "Evolution of shock-induced reactive and inert double-layer gas cylinders." *International Journal of Hydrogen Energy*, *109*, 1064-1080.

[4] **Li, X.**, Hao, J., & Wen, C. Y. & Shao, X. "Effects of Mach numbers on inert and reactive shock-induced double-layer gas cylinders." (in preparation)

Conferences:

[1] **Li, X.**, Hao, J., & Wen, C. Y. "Evolution of shock-accelerated multi-layer gas cylinder with different Mach numbers." *The 34th International Symposium on Shock Waves*, July 16 – 21, 2023, Daegu, South Korea.

[2] **Li, X.**, Hao, J., & Wen, C. Y. "Numerical simulation of the shock-accelerated double-layer gas cylinder at different Atwood numbers." *The 2nd International Symposium on Advances in Aerodynamics*, Dec 9 – 12, 2023, Guangzhou, China.

[2] **Li, X.**, Hao, J., & Wen, C. Y. "Evolution of reactive shock-induced double-layer gas cylinder." *The 13th National Conference on Fluid*, Aug 9 – 13, 2024, Harbin, China. (in Chinese)

Acknowledgements

First and foremost, I would like to express my heartfelt gratitude to my supervisor, Prof. Jiaao Hao. Prof. Hao possesses profound expertise and exceptional research capabilities. Throughout my doctoral studies, he has provided invaluable guidance and unwavering support. From the initial confusion on the research path to gradually clarifying the research direction and achieving certain results, Prof. Hao has consistently offered patient and professional explanations, as well as insightful and constructive suggestions. His mentorship has been instrumental to my academic and professional development.

I am also deeply grateful to my co-supervisor, Professor Chih-Yung Wen. Prof. Wen is a scholar of great depth and integrity, with gentle demeanor and patient guidance. His concept of work-life balance has alleviated much of my anxiety in research. I sincerely appreciate his valuable feedback during group meetings and his thoughtful care and encouragement in daily life. It is my great fortune to have encountered these two supervisors in my doctoral career.

I would also like to extend my sincere appreciation to Dr. E Fan, Dr. Chun Kit Uy, Dr. Zongnan Chen, Dr. Cheng Li, Dr. Xin Li, Dr. Xu Liu, and Xinke Shao for their kind support and assistance in my research. I am likewise thankful to Patrick, Athena, Guoqin Zhao and other friends in GH034, Yifeng Chen, Jiachen Lu, Ziming Song and other friends in QR813 for the camaraderie and joyful moments we shared, which enriched my PhD experience.

Finally, I owe my deepest thanks to my parents and my boyfriend. Your unconditional love, steadfast support, and enduring understanding have been my greatest source of strength throughout this journey. I am truly grateful for your presence in my life.

Table of Contents

List of Figures

List of Tables

Nomenclature

$a_1,\ a_2$	The amplitude growth rates of different interfaces
$a_{1,0},\ a_{2,0}$	The initial amplitude of different interfaces
a_0	The initial amplitude
A	Atwood number
A_1	Atwood number for the first layer
A_2	Atwood number for the second layer
$A_c,\ A_t$	The modified Atwood numbers based on the layer thickness
$A_{f,m}$	The pre-exponential factor
$B_{f,m}$	The temperature exponent
B	Bubble
c_0	The sound speed of the ambient air
C	The mass fraction of SF_6 at each grid within the gas cylinder
C_{outer}	The normalized mean mass fraction of SF_6 of the gas ring
C_{inner}	The normalized mean mass fraction of SF_6 of the inner cylinder
C_j	The molar concentration of each species
$C_{p,i}$	The species isobaric heat capacity
d	The diameter of the inner gas cylinder
D	The diameter of the outer gas cylinder
D_i	The species diffusion coefficient
D_{ij}	The binary diffusion coefficient
DP	The normalized quantity derived from the pressure gradient, $1 - e^{-\frac{50\times\nabla p}{1\times10^{10}}}$
E	The total energy per unit volume
$E_{f,m}$	The activation energy
f	The grid solution
f_{exact}	The continuum value at zero grid spacing
F_s	A factor of safety
$\boldsymbol{F},\ \boldsymbol{G}$	The inviscid fluxes
$\boldsymbol{F}_v,\ \boldsymbol{G}_v$	The viscous fluxes
$g_1,\ g_2$	Functions independent of the grid spacing

h_i	The species enthalpy
h	The height of the inner cylinder
H	The height of the outer cylinder
I	Acoustic impedance
$J_{i,x}, J_{i,y}$	The species mass diffusion in the x and y directions
k	Wave number
$k_{f,m}, k_{b,m}$	Forward and backward rate coefficients
$K_{c,m}$	The equilibrium constant
$m_{\mathrm{H_2}}$	The mass of H_2
$m_{\mathrm{H_2},0}$	The initial mass of H_2
L_0	The initial thickness of a fluid layer
M	Mach number
M_{r}	Mach number of the reflected shock wave
M_{ij}	The equivalent molecular mass of the binary mixture
MW_i	The species molecular weight
n_r	Number of elementary reactions
n_s	Number of species
p	Pressure
p_0	The pre-shocked pressure of the ambient air
p_0'	The post-shocked pressure of the ambient air
$P_{\omega,\mathrm{dil}}$	The spatially integrated dilatation term
$P_{\omega,\mathrm{bar}}$	The spatially integrated baroclinic term
$P_{\omega,\mathrm{vis}}$	The spatially integrated viscous term
$q_x,\ q_y$	Thermal conduction in the x and y directions
r	Radius of the inner cylinder
R	Radius of the bubble
$R_1,\ R_3$	Density ratios
R_u	Universal gas constant
S_i	The species entropy
S_{inner}	The normalized area where the mass fraction of SF_6 within the inner cylinder is greater than 0.01
S_{outer}	The normalized area where the mass fraction of SF_6 within the

	gas ring is greater than 0.01
$\boldsymbol{S}_c$	The chemical source term
t	Physical time
T	Temperature
u, v	The velocities in the x and y directions
u_s	The velocity of the incident shock wave
u_{t1}	The velocity of the transmitted shock wave
u_1'	The post-shock velocity behind the incident shock wave
u_2'	The post-shock velocity behind the transmitted shock wave
$\vec{U}$	Velocity
$\boldsymbol{U}$	The conservative variable
V'	Flow velocity behind the shock
$VF_1,\ VF_2$	The volume fraction of SF_6 in the gas ring and the inner cylinder
w	The width of the inner cylinder
w_l	The growth of the layer width
$w_{l,0}$	The average initial layer width
W	The width of the outer cylinder
W_i	The velocity of the incident shock wave
W_i'	The velocity of the first transmitted shock wave
W_t	Velocity of the transmitted shock wave
W_r	Velocity of the reflected shock wave
z	The grid refinement ratio
Z_1	Compression factor, $1 - \Delta u_1/u_s$
Z_2	Compression factor, $1 - \Delta u_2/u_{t1}$
Z_L	Compression factor, $1 - \Delta u_1/u_{t1}$
α	The angle between the incident shock wave and the interface
γ	Specific heat ratio
γ_0	The specific heat ratio of the ambient air
γ_1	The specific heat ratio of the gas within the bubble
Γ	Circulation
Γ_r	The third body efficiency on the reaction rate
δI	Acoustic impedance mismatch

ΔG_m^0	The change in Gibbs free energy
$\Delta u_1,\ \Delta u_2$	The jump speed of different interfaces
ε	The relative error of quantity f
$(\varepsilon/k)_i$	Lennard-Jones potential parameter for species i
η	The combustion completeness
κ	The thermal conductivity of the mixture
κ_i	The thermal conductivity of each species
λ	Radius ratio
μ	The mixture viscosity
$v_{m,i}^f$	The stoichiometric coefficients of the reactants of each reaction
$v_{m,i}^b$	The stoichiometric coefficients of the products of each reaction
ξ	$\tanh(Z_L k L_0)$
ρ	Density
ρ_A	The densities of the ambient gas
ρ_B	The densities of the gas inside the bubble
ρ_i	The density of each species
ρ_a	The pre-shocked density of the ambient air
ρ_a'	The post-shocked density of the ambient air
ρ_b	The pre-shocked density of the gas in the bubble
$\rho_1,\ \rho_2,\ \rho_3$	The densities of different layers
σ_i	The molecular collision diameter
σ_{ij}	The average collision diameter
Σ	Mixing fraction
τ	A nondimensional time
τ'	A nondimensional time for the first transmitted shock reaches upstream interface of inner cylinder
τ_{ij}	The viscous stress component
Y_i	The species mass fraction
X_i	The species molar fraction
$\vec{\omega}$	Vorticity
$\dot{\omega}_i$	The species of chemical mass production
$\Omega_{\mu,i}$	The collision integral

$\nabla\rho$	Density gradient
∇p	Pressure gradient

Abbreviations

DDT	Deflagration-to-detonation transition
DI_1	Downstream interface of the inner cylinder
DI_1	Downstream interface of the inner cylinder
DTS	Diffracted transmitted shock wave
DTS_2	Second diffracted transmitted shock wave
FPS	Free-precursor shock wave
GCI	Grid Convergence Index
hpz	High-pressure zone
HT_1, HP_1	First high-temperature and high-pressure
HT_2, HP_2	Second high-temperature and high-pressure
HT_3, HP_3	Third high-temperature and high-pressure
HT_4, HP_4	Fourth high-temperature and high-pressure
HLL	Harten-Lax-van Leer
HLLC	Harten-Lax-van Leer Contact
ICF	Inertial confinement fusion
IS	Incident shock wave
ISBI	Inert shock-bubble interaction
KH instability	Kelvin–Helmholtz instability
Merged-$shock_1$	First merged shock wave
Merged-$shock_2$	Second merged shock wave
MS	Mach stem
MUSCL	Monotone upstream-centered scheme for conservation law
PLIF	Planar Laser-Induced Fluorescence
QP	Quadruple point
RDS	Refracted diffracted shock wave

REW	Reflected expansion wave
RM instability	Richtmyer-Meshkov instability
RRW	Reflected rarefaction wave
RS	Reflected shock wave
RS_1	First reflected shock wave
RSBI	Reactive shock-bubble interaction
RSS_4	Reflected S_4
RT instability	Rayleigh–Taylor instability
scramjet	Supersonic combustion ramjet
sl	Slip lines
SBI	Shock-bubble interaction
STP	Standard temperature and pressure
TP	Triple point
TRS	Transmitted reflected shock wave
$TRSS_4$	Transmitted reflected S_4
T_1RS_1	First transmitted reflected shock wave
T_2RS_1	Second transmitted reflected shock wave
TS_3	Third transmitted shock wave
WENO	Weighted Essential Non-Oscillation reconstruction
1-D	One-dimensional
2-D	Two-dimensional
3-D	Three-dimensional

CHAPTER 1 Introduction

1.1. Background

RM instability occurs when a perturbed density interface is impulsively accelerated by a shock wave [1], [2], [3]. The perturbation at the interface initially undergoes linear growth, which is then followed by the development of characteristic vortex, spikes, and bubble structures. As instability evolves, a mushroom-shaped structure emerges on the spike, accompanied by mass, momentum, and energy transport across the interface. Eventually, the flow transitions into turbulence. The fundamental flow features of the RM instability are illustrated in Figure 1-1, which shows the interaction between a planar shock wave and a heavy–light interface with a single-mode perturbation [3].

As a fundamental flow phenomenon, RM instability also has extensive relevance to various engineering applications, holding significant importance in inertial confinement fusion (ICF) on a scale of millimeters [4], scramjet engines on a scale of a few meters [5], and supernova explosions on the scale of the sun [6].

The interaction between a shock wave and a gas bubble (SBI) is a canonical setup for studying RM instability, involving a broad spectrum of angles between the pressure gradient and density gradient. Depending on whether the gas is inert or reactive, SBI can be further categorized into ISBI and RSBI. The evolution of both ISBI and RSBI induces shock refraction, reflection and diffraction, resulting in complex wave structures that are strongly influenced by the initial conditions.

In this work, numerical methods are conducted to explore the impacts of initial conditions, such as Mach numbers, Atwood numbers and radius ratios on the evolution of ISBI and RSBI configurations, thereby offering theoretical insights of RM instability in engineering applications.

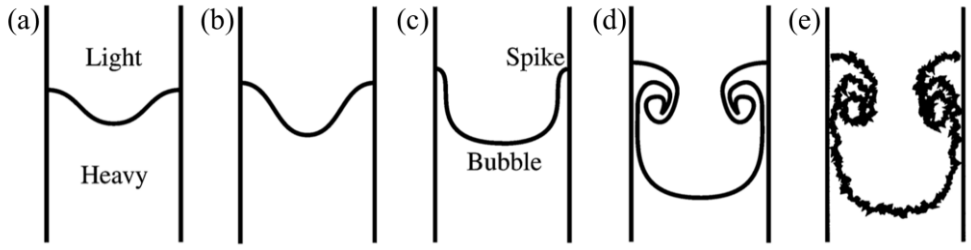

Figure 1-1. The fundamental flow features of a single-mode perturbation from Brouillette [3]. (a) Initial configuration; (b) Linear growth;(c) Spike and bubble development;(d) Roll-up of spike;(e) Emergence of small-scales and turbulent mixing.

1.2. Physics of SBI

1.2.1. Vorticity production and transport

After the planar shock wave interacts with the bubble, misalignment between the density and pressure and gradients leads to the deposition of baroclinic vorticity, inducing the generation of vortex pairs. Vorticity is mathematically defined as the curl of the velocity:

$$\vec{\omega} \equiv \nabla \times \vec{U} \tag{1-1}$$

Taking the curl of the momentum equation for a compressible flow, one obtains the vorticity transport equation, given as:

$$\frac{D\vec{\omega}}{Dt} = (\vec{\omega} \cdot \nabla)\vec{U} - \vec{\omega}(\nabla \cdot \vec{U}) + \frac{1}{\rho^2}(\nabla\rho \times \nabla p) + \nu\nabla^2\vec{\omega} \tag{1-2}$$

The right-hand side of this equation consists of several terms, each representing a specific physical process. The first term, $(\vec{\omega} \cdot \nabla)\vec{U}$, is the vortex-stretching term, which is essential for the discussion of three-dimensional turbulence and mixing. This term describes the stretching, turning, and tilting of vortex lines by gradients in the velocity field. Vortex stretching reflects the principle of conservation of angular momentum, decreasing the moment of inertia of fluid elements composing a vortex line and increasing their angular speed. The vortex-stretching and vortex-tilting term is absent in 2-D models, in which ω is perpendicular to the flow. The second term, $\vec{\omega}(\nabla \cdot \vec{U})$, represents the vortex dilatation term, which is significant only in highly compressible fluids. The third term, $\frac{1}{\rho^2}(\nabla\rho \times \nabla p)$, is the baroclinic term, representing the rate of vorticity generation due to baroclinicity in the flow. This term highlights that the misalignment of local pressure and density gradients leads to the generation of vorticity in the flow field. The last term, $\nu\nabla^2\vec{\omega}$, represents the rate of change of ω due to molecular diffusion of vorticity.

For the scenario of 2-D SBI with a weak incident shock wave, the vortex-stretching term $(\vec{\omega} \cdot \nabla)\vec{U}$ is negligible. Similarly, the vortex dilatation term $\vec{\omega}(\nabla \cdot \vec{U})$ is insignificant due to the weak compressibility of the flow. The short evolution time of the interface and the low fluid viscosity also renders the viscous diffusion term $\nu\nabla^2\vec{\omega}$ negligible. Therefore, equation (1-3) can be simplified as:

$$\frac{\mathrm{D}\vec{\omega}}{\mathrm{D}t} = \frac{1}{\rho^2}\nabla\rho \times \nabla p \tag{1-3}$$

As a result, after the shock wave interacts with the perturbed interface, the misalignment between the density gradient and pressure gradient leads to the baroclinic vorticity deposited at the interface, which is the main source of vorticity in the flow field.

1.2.2. Nonlinear acoustic effects

Nonlinear-acoustic effects refer to the refraction, reflection, and diffraction of incident shock waves over bubbles, caused by the curvature of the bubble interface and the acoustic impedance mismatch at the interface. Under the impact of the acoustic impedance mismatch at the bubble interface, the bubble can behave like a diverging or converging lens [7]. The acoustic impedance, defined as $I = \rho c$, is the product of the density of the gas and the sound speed (c) in that medium. It represents the constant proportionality between the impressive velocity and applied pressure [8]. The difference in acoustic impedance between two media is referred to as the impedance mismatch, denoted by $\delta I = I_2 - I_1$.

Figure 1-2 illustrates the influence of bubble interface curvature on shock refraction patterns under two different impedance mismatch scenarios. Figure 1-2(a) shows the shock refraction pattern for convergent geometry ($\delta R > 0$), where the transmitted shock wave presents a concave profile and propagates behind the unrefracted IS. The reflected wave under these conditions is a shock wave. Figure 1-2(b) depicts the refraction pattern for a divergent configuration ($\delta R < 0$), where the reflected wave is a rarefaction. t small incidence angles, regular refraction occurs, with the incident and transmitted waves intersecting the interface at the same point. As the incidence angle increases, various forms of irregular refraction emerge [9], [10].

The effect of acoustic impedance mismatch on the shock refraction pattern is limited to the early stage of evolution. As the interaction evolves over several shock-passage times, the bubble morphology becomes primarily governed by vortical motion. In this work, the Atwood number is employed to quantify the density ratio across the bubble interface, which is given by:

$$A = \frac{\rho_B - \rho_A}{\rho_B + \rho_A} \tag{1-4}$$

For the gas pairs considered here, $A > 0$ denotes convergent geometry ($\delta R > 0$), while $A < 0$ corresponds to divergent geometry ($\delta R < 0$). However, as noted by Thompson [8], convergent refraction may still occur even when $A < 0$, and vice versa under certain atypical thermodynamic conditions.

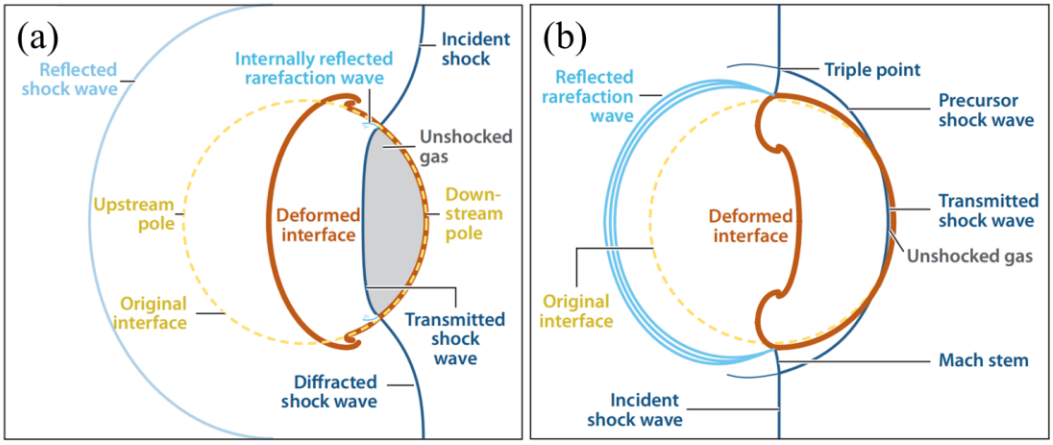

Figure 1-2. Schematic representation of shock-bubble interaction flow field and shock refraction patterns for (a) convergent geometry and (b) divergent geometry [11].

1.2.3. Shock focusing phenomena

Figure 1-3 illustrates the various stages of shock refraction under convergent geometry, resulting in shock focusing at the downstream pole of the bubble. The convergence of the diffracted shock waves, accompanied by the convergence of the transmitted shock wave, generates a sharp increase in pressure and temperature, which can potentially initiate ignition in the case of RSBI.

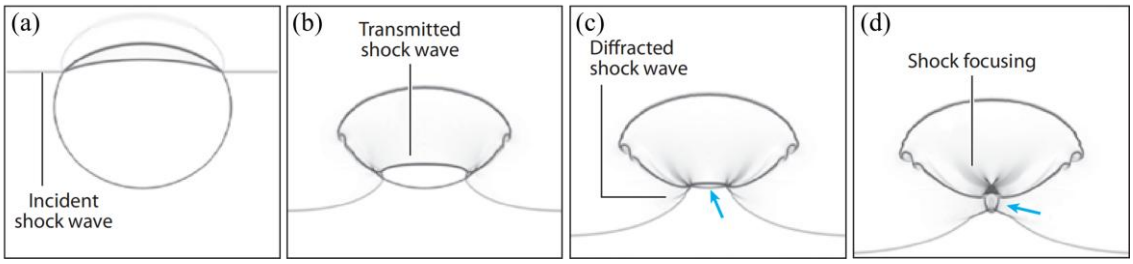

Figure 1-3. Schematic view of shock focusing in the case of convergent geometry ($A > 0$). The arrow in the diagram indicates the location of the shock focusing [11].

1.3. Literature review

1.3.1. Study of ISBI

The concept of the interaction between shock waves and curved surfaces was initially introduced by Markstein [12]. In earlier studies, Haas et al. [13] created gas cylinders filled with light gas (He) or heavy gas (R22) by using the nitrocellulose film technique. The resulting wave patterns within and outside of the interface were observed, with the shape of the shock waves predicted using geometric acoustics. The evolution of the interface was also quantitatively analyzed. Building upon this experiment, Winkler et al. [14] conducted

numerical simulations of a shock wave impacting an R22 bubble at a Mach number of 2.0. They observed the formation of a continuously growing supersonic vortex ring after the shock wave had passed through the bubble. Picone et al. [15] furthered this work with numerical simulations demonstrating the dominance of vorticity in the later stages of interface evolution. They proposed the PB model for predicting the circulation deposited on the interface:

$$\Gamma_{\mathrm{PB}} = 2RV'\left(1-\frac{V'}{2W_{\mathrm{i}}}\right)\ln\left(\frac{\rho_a}{\rho_b}\right) \tag{1-5}$$

Subsequently, Yang et al. [16] conducted a combined numerical and theoretical investigation of the interaction between shock waves and gas cylinders. They presented simulation results for shock waves impacting a He cylinder with incident Mach number ranging from 1.05 to 2.0. Based on the analysis of circulation deposited at the interface, they proposed YKZ model for predicting circulation:

$$\Gamma_{\mathrm{YKZ}} = \frac{4R}{W_{\mathrm{i}}}\frac{p_0'-p_0}{\rho_a'}\frac{\rho_b-\rho_a}{\rho_b+\rho_a} \tag{1-6}$$

PB and YKZ model neglected the variations in shock strength, interfacial geometry, pressure and density of the gas. To address these limitations, Samtaney and Zabusky [17] derived an analytical expression for the circulation deposited per unit length of the interface:

$$\frac{\mathrm{d}\Gamma_{\mathrm{SZ}}}{\mathrm{d}s} = \frac{2c_0}{\gamma+1}\left(1-\sqrt{\frac{\rho_a}{\rho_b}}\right)(1+M^{-1}+2M^{-2})(M-1)\sin\alpha \tag{1-7}$$

where $\gamma = (\gamma_0+\gamma_1)/2$. It is noted that this model was originally developed for light/heavy interfaces but can be extended to accommodate various interface geometries by integrating along different paths. When integrated along the interface of a gas cylinder, the SZ model for predicting the circulation deposited on the interface was given by:

$$\Gamma_{\mathrm{SZ}} = \begin{cases} \dfrac{4}{1+\gamma}\Gamma^*, 0 < A < 0.2 \\ \dfrac{\pi+2}{1+\gamma}\Gamma^*, A \geqslant 0.2 \end{cases} \tag{1-8}$$

$$\Gamma^* = \left(1-\sqrt{\frac{\rho_a}{\rho_b}}\right)(1+M^{-1}+2M^{-2})(M-1)Rc_0$$

Subsequently, Niederhaus et al. [18] conducted numerical simulations of the interaction between shock waves ($1.1 < M \leq 2.0$) and gas bubbles ($-0.8 < A < 0.7$) by solving the three-dimensional multi-component Euler equations. Based on 1-D gas dynamics theory, they proposed a new circulation model:

$$\Gamma_{1\mathrm{D}} = u_1' y_1 + \frac{R}{3}(u_2' - u_1')\left(\frac{y_1}{R}\right)^3 + \frac{2R}{\widetilde{W}}(W_\mathrm{t} - u_2')u_2' - \frac{2R}{\widetilde{W}}\left(W_\mathrm{i} + \frac{W_\mathrm{r}}{\sqrt{M_\mathrm{r}}}\right)u_1'$$

$$y_1 = \frac{2R}{\widetilde{W}}\frac{u_2' + W_\mathrm{r}}{\sqrt{M_\mathrm{r}}}, \widetilde{W} = \begin{cases} W_\mathrm{t}, A < 0 \\ W_\mathrm{i}, 0 \leqslant A \leqslant 0.2 \\ 2W_\mathrm{i}/(1+\pi/2), A > 0.2 \end{cases} \quad \textbf{(1-9)}$$

To mitigate the impact of the struts and membrane, Jacobs [19], [20]employed jet technology to create light and heavy gas cylinders and observed the ensuing flow field using PLIF. Tomkins et al. [21] investigated the interaction between shock waves and gas columns using a method similar to that of Jacobs [19], [20]. They conducted quantitative measurements of the mixing between air and SF_6 in the post-shock flow field and provided a detailed analysis of the underlying mixing mechanisms. The results revealed the presence of three distinct mixing regions: the bridge structure connecting the two primary vortices, the vortex cores, and the region dominated by KH instabilities. Bagabir et al. [22] investigated the effects of the Mach numbers on the interaction of the shock wave with a cylindrical bubble numerically, which suggested that the displacements of the upstream, downstream and jet interfaces were not significantly affected below the Mach number of 2.5. However, larger deformations of the bubble occurred, and a secondary-reflected shock wave formed upstream of the bubble at higher Mach numbers. Zhai et al. [23] investigated the evolution of the shock-heavy gas bubble, emphasizing the formation of the jet. Zhu et al. [24] studied the influence of the various Mach numbers on the shock-SF_6 bubble interaction, focusing on the issues of shock focusing. Besides, the bubble volume and effective bubble volume decrease, but the compression ratio, the mixedness between two different fluids and the vorticity are all raised with increasing Mach number. Ou et al. [25] obtained gas cylinders of different Atwood numbers by mixing SF_6 and air, studying the effects on shock focusing position as well as the type of jet produced. Guan et al. [26] explored the characteristics of shock-accelerated heavy gas bubbles and emphasized the categories of the forming mechanisms on the bubble jets, which can be divided into two types: regular and irregular jets. Moreover, Fan et al. [27] and Deng et al. [28] investigated the interaction between shock wave and polygonal gas cylinders, proposed a modified theoretical model to predict the circulation based on the SZ model.

While previous studies have primarily focused on the evolution of a single-layer interface following a shock impact, practical applications often involve multi-layer interfaces. For a finite-layer fluid layer, Taylor [29] theoretically put forth a theoretical framework for the RTI in a finite-thickness liquid layer, obtaining a linear solution for the amplitude growth

of the two interfaces. The RMI can be considered as the impulsive-acceleration limit of the RT instability. When the thickness of the fluid layer is sufficiently small, particularly less than one-third of the interface wavelength, the interface coupling effect becomes significant. Subsequently, Ott [30] proposed a nonlinear solution for the RT instability growth of a thin massless fluid layer, explaining the formation of spike and bubble structures. Mikaelian [31] obtained a linear solution for the RMI growth of a stratified fluid, assuming an incompressible flow and discussing the interface coupling as well as the necessary conditions for the freeze-out of the first interface growth. The results were compared to Ott's solution. De Frahan et al. [32] employed the discontinuous Galerkin method to investigate the effects of the amplitude and phase difference on the perturbation growth for successive layers of fluids. developed a weakly nonlinear third-order analysis to explore the dependence of perturbation growth on arbitrary Atwood numbers in two superimposed fluid layers within the context of RM instability.

In experiments, Jacobs et al. [33] employed a jet technique to generate an SF_6 curtain interface with symmetric perturbations. They developed a linear model to predict the amplitudes of the two interfaces, which considered interface coupling and a nonlinear model based on vortex dynamics to describe the evolution of the mixing width. The corresponding expressions are given as:

$$\begin{aligned} a_1 &= \frac{k\Delta u_1\left[A_t\left(a_{1,0}-a_{2,0}\right)+A_c\left(a_{1,0}+a_{2,0}\right)\right]}{2} \\ a_2 &= \frac{k\Delta u_2\left[A_t\left(a_{1,0}-a_{2,0}\right)-A_c\left(a_{1,0}+a_{2,0}\right)\right]}{2} \end{aligned} \tag{1-10}$$

$$w = \frac{2}{k}\sin L_0{}^{-1}\left[\frac{2}{\pi}\left(1+\tan L_0\left(\frac{1}{2}kw_0\right)\right)k^2 A_{\mathrm{t}}\Delta V a_0 t + \sin L_0\left(\frac{1}{2}kw_0\right)\right] \tag{1-11}$$

with two modified Atwood numbers,

$$\begin{aligned} A_t &= \frac{\rho_2-\rho_1}{\rho_2\tanh\left(kL_0/2\right)+\rho_1} \\ A_c &= \frac{\rho_2-\rho_1}{\rho_2\coth(kL_0/2)+\rho_1} \end{aligned} \tag{1-12}$$

To predict the linear growth of interface perturbations in a heavy fluid layer, while accounting for additional instabilities at the interfaces and their coupling, Liang et al. [34], [35] modified the Jacobs model. Specifically, the first interface was corrected by considering IS compression, and the second by considering TS_1 compression, which can be expressed:

$$a_1 = \frac{k\Delta u_1 \left\{ A_t \left[Z_1 a_{1,0} - \frac{(Z_2+1)a_{2,0}}{2} \right] + A_c \left[Z_1 a_{1,0} + \frac{(Z_2+1)a_{2,0}}{2} \right] \right\}}{2}$$
$$a_2 = \frac{k\Delta u_2 \left\{ A_t \left[Z_1 a_{1,0} - \frac{(Z_2+1)a_{2,0}}{2} \right] - A_c \left[Z_1 a_{1,0} + \frac{(Z_2+1)a_{2,0}}{2} \right] \right\}}{2} \quad \textbf{(1-13)}$$

with two modified Atwood numbers,

$$A_t = \frac{\rho_2 - \rho_1}{\rho_2 \tanh(Z_L k L_0/2) + \rho_1}$$
$$A_c = \frac{\rho_2 - \rho_1}{\rho_2 \coth(Z_L k L_0/2) + \rho_1} \quad \textbf{(1-14)}$$

For a light fluid layer, Liang et al. [36] investigated the effects of layer thickness and initial amplitude of the perturbation on RM instability. They accurately predicted the interface perturbations using both linear and nonlinear models. It emphasized the significance of wave reverberation within the fluid layers in shaping their evolution.

Furthermore, Liang et al. [37], [38] quantified RM instability at two interfaces with arbitrary fluid combinations to evaluate amplitude growth, which is given by:

$$a_1 = -\frac{k\Delta u_1 Z_1 a_{1,0} \left[(R_1 - 1)(2R_3\xi + \xi^2 + 1) + \frac{(1-R_3)(1-\xi^2)}{Z_1 a_{1,0}/Z_2 a_{2,0}} \right]}{2\xi(R_1 R_3 + 1) + (R_1 + R_3)(\xi^2 + 1)}$$
$$a_2 = \frac{k\Delta u_2 Z_2 a_{2,0} [\epsilon(R_1 - 1)(\xi^2 - 1) - (1 - R_3)(2R_1\xi + \xi^2 + 1)]}{2\xi(R_1 R_3 + 1) + (R_1 + R_3)(\xi^2 + 1)} \quad \textbf{(1-15)}$$

This model was further extended by combining with potential flow theory to quantify the long-term amplitude growth in the nonlinear regime. In addition, Liang et al. [39] derived a linear solution for RM instability involving three interfaces and quantified the coupling effects between the two fluid layers.

For a multi-layer gas bubble, Xiang et al. [40] conducted numerical investigations on the interaction between a shock wave and a water column embedded with an air cavity, examining the effects of shock intensity and gas cavity size on interface evolution. The study focused particularly on gas cavity deformation, the breakup mechanism of the water column, and the formation of transverse jets. Wu et al. [41] simulated the collision of a cylindrical column embedded with an air or vapour cavity on a rigid wall, with a focus on the interaction between the water-hammer shock reflected from the rigid wall and the gas cavity. The study also considered the phase transition process and demonstrated the differences between the collapses of air and vapour cavities. Wang et al. [42] presented the configurations of gas rings and introduced a method for predicting circulation based on the linear superposition of existing circulation models. Through the soap film technique, Feng et al. [43], [44] focused

on the evolution process of the double-layer gas cylinder by changing the radius ratio and eccentricity between the inner and outer cylinders experimentally and numerically, accessing a quantitative analysis by measuring the width and height of the cylinders, in addition to the displacement of the upstream poles. Studies on the interface area and average volume fraction evaluated the impact of radius ratio and eccentricity on the mixing of gases.

1.3.2. Study of RSBI

Distinguished from inert scenarios, a shock-induced change in thermodynamic properties can trigger ignition, leading to a reaction wave classified into two types: deflagration and detonation. Deflagration is a subsonic reaction wave driven by energy transfer from the burning to the unburned gas through diffusion [45]. In contrast, detonation is sustained by a rapid chemical reaction with significant heat release, preceded by a shock wave that compresses and preheats the gas mixture [45]. Under certain conditions, a deflagration wave can transition into a detonation wave, a phenomenon known as DDT. A deflagration wave is typically unstable and prone to acceleration. Under certain conditions, the continuous acceleration can abruptly lead to a transition into a detonation wave [46]. Relevant research on shock-induced chemistry can be traced back to Markstein's study [47] on shock-flame interactions, which were found to effectively increase flame area, promote energy release, and improve combustion efficiency. Thomas et al. [48] experimentally and numerically investigated the behaviour of a light spherical flame accelerated by a strong shock wave in gas mixture, demonstrating flame instabilities and highlighting the occurrence of detonation near the reaction zone. Batley et al. [49] conducted numerical simulations to study the interaction between shock waves and two-dimensional flame balls, describing flame distortion and vorticity generation. Ju et al. [50] numerically explored the mechanisms of vorticity generation and the impacts of shock intensity on two-dimensional shock-flame interactions. Oran et al. [51] conducted high-resolution simulation with adaptive mesh refinement to study hot-spot ignition and DDT in shock-flame interactions. Gui et al. [52] carried out extensive research to reveal the complex combustion phenomena in confined spaces during shock-flame interactions. Bakalis et al. [53] performed a numerical investigation on DDT through the interaction of a weak shock with a series of separate laminar flame cylinders. Their study validated the occurrence of DDT triggered by multiple shock-flame interactions.

RSBI was first experimentally studied by Haehn et al. [54], who identified two distinct ignition mechanisms depending on the strength of the incident shock wave. Diegelmann et al. [55], [56], [57]conducted a series of 2-D RSBI numerical simulations, revealing that changes

in the incident shock strength and pressure behind the shock front significantly affect the behaviour of the reaction wave. They found that deflagration initiated at Mach numbers between 2.0 and 2.3, with DDT occurring at Mach 2.19, characterized by an increase of the pressure peak, a decrease of hydrogen in the reaction zone and steepening of the temperature profile. Detonation is observed at Mach numbers above 2.3. In their 3-D RSBI simulation, the evolution process at Mach 2.83 was described, including the development of vortices and interface instabilities. Li et al. [58] focused on the effect of bubble geometry on ignition and bubble evolution at high Mach numbers, showing that the geometric effects on RSBI are more significant than on ISBI. Fan et al. [59] described flow characteristics in RSBI and analyzed the impact of deflagration on bubble morphologies and gas mixing at low Mach numbers.

1.4. Motivations and Objectives

1.4.1. Motivations

ICF is a type of fusion approach that relies on the inertia of the fuel mass to provide confinement [60], [61]. The ICF target capsule is a spherical shell consisting of an outer ablator and an inner region containing deuterium-tritium (DT) as the primary fuel. The minimum energy required for ignition of the fusion fuel in the capsule is determined by the peak implosion velocity [62]. The success of ICF hinges on the formation of a hot spot with sufficient temperature and density at the center [63]. Due to processing constraints, the interfaces between the layers of the ICF target capsule exhibit some roughness, and small perturbations are inevitably present. When the shock wave accelerates these interfaces, RM instability occurs, and the small perturbations on the interface continue to grow, possibly causing mixing between the outer ablator material and the inner fuel. This leads to a significant increase in hot spot radiation, a reduction in energy gain of the inner fuel, and ultimately ignition failure [64], [65]. Therefore, it is important to suppress RM instability in ICF. However, an ICF target capsule consists of multiple material layers, including an outer ablator and an inner fuel layer. During the practical ignition process, shock waves interact with the multi-layer interface rather than single-layer interface. Moreover, there is a CH form shell (35 mg ml^{-1}) existing between the outer shell (2.7 g ml^{-1}) and the inner shell (200 mg ml^{-1}) in a double-shell ICF capsule [66], [67] for instance, suggesting that the materials of different shells are completely dissimilar.

The scramjet is a type of airbreathing ramjet engine [68]. Unlike traditional jet engines, supersonic combustion engines, which can draw in the ambient air to enter the combustion

chamber and provide the oxidizer needed for fuel combustion, without carrying additional oxidizers distinguished from traditional jet engines. Due to the extremely short residence time of airflow in the combustion chamber, the fuel must mix rapidly with the air to obtain sufficient oxidizer. During the process of fuel-air mixing, the RM instability occurs, and the turbulence caused by RM instability can promote the contact between fuel and oxidizer, thereby improving combustion efficiency. In practical applications, fuel-atomized droplets often contain air cavities, leading to shock interactions with multi-layer interfaces within the droplets.

In traditional supernova models, there are typically two explosion mechanisms: thermonuclear explosion supernovae (Type I) and core-collapse supernovae (Type II) [62]. In Type II supernova explosion, the core of the star is enveloped by helium and hydrogen elements, surrounded by outer layers of elements such as iron, silicon, carbon, and oxygen [69]. During the explosion, the stellar core undergoes fusion from lighter to heavier elements and eventually collapses to an extremely high, incompressible density [70]. Meanwhile, the outer material rapidly falls inward, generating a shock wave. When this shock wave collides with the incompressible core, it reflects and interacts with the multiple-layered structure, triggering RM instability [71]. Understanding RM instability is crucial for predicting the structural evolution of supernova remnants. In actual explosions, the shock wave also impacts multilayer interstellar clouds of varying densities.

In summary, RM instability involving multi-layer interfaces is more representative of practical scenarios than its single-layer counterpart. However, prior studies on the evolution of inert double-layer gas cylinders have primarily focused on geometric parameters such as radius ratio and eccentricity, while the influence of other fundamental factors, such as the incident shock Mach number and the Atwood number, remains unexplored. Given the relevance of combustion in many applications, the study of shock interactions with reactive gas cylinders is also of vital importance. Previous studies about RSBI have only specialized in single-layer configurations, neglecting the complex interactions that arise in multi-layer systems. Therefore, understanding the behaviour of RM instability with multi-layer of both inert and reactive gas bubbles is critical for practical applications. To fill these gaps, this work aims to address this gap by numerically investigating the interaction between the shock wave and the inert and reactive double-layer gas cylinder under initial conditions.

1.4.2. Objectives

The objective of this research is to numerically investigate the interaction between shock waves and both inert and reactive double-layer gas cylinders under various initial conditions.

Many efforts have been put into the RM instability involving single-layer interfaces, both inert and reactive double-layer gas cylinders are still unclear. The main objectives in this study are divided into two main parts, which are listed as below:

A. The shock-induced evolution of inert double-layer gas cylinders at different Mach numbers and Atwood numbers.
    i. To qualitatively and quantitatively characterize the effects of varying Mach number and Atwood number on the evolution of the double-layer gas cylinder.
    ii. To explore the underlying mechanism of vorticity evolution under different Mach and Atwood numbers based on the vorticity transport equation.
    iii. To predict the net circulation by linearly summing existing circulation models.
    iv. To investigate the influence of Mach number and Atwood number on gas mixing based on the analysis of mean mass fraction evolution.
B. The shock-induced evolution of reactive double-layer gas cylinders at different Mach numbers and radius ratios.
    i. To qualitatively and quantitatively characterize the effects of varying Mach number and radius ratio on the evolution of the double-layer gas cylinder.
    ii. To investigate the process of hot spot generation and identify the type of reaction wave under various Mach numbers and radius ratios.
    iii. To analyze influences of reaction waves on hydrodynamical properties involving vorticity and mixing fraction.

1.5. Outline

In Chapter 1, the background of this research is introduced. First, a literature survey of RM instability is provided. Then, based on the canonical configuration of gas bubble or cylinder, the literature review and engineering applications of RM instability associated with ISBI and RSBI are presented. In addition, the existing gaps in the studies of ISBI and RSBI are stated.

In Chapter 2, the details of the numerical simulations are presented. The CFD code is developed in a multi-block parallel finite-volume CFD solver PHAROS. The detailed governing equations, flux schemes, time marching methods and chemical reaction mechanisms are introduced. Moreover, the numerical results of ISBI and RSBI are validated with experimental data.

In Chapter 3, the impacts of different Mach number and Atwood number on the evolution of an inert double-layer gas cylinder are analyzed qualitatively and quantitatively.

Then, the underlying mechanism of vorticity deposition is explored using the vorticity transport equation. Net circulation can be predicted by linearly summing existing circulation models. In addition, gas mixing is also examined through the analysis of mean mass fraction evolution.

In Chapter 4, the evolution of a reactive double-layer gas cylinder under different Mach numbers and radius ratios is qualitatively and quantitatively characterized. The process of hot spot formation is investigated, and the types of resulting reaction waves are identified. Furthermore, the influences of these reaction waves on hydrodynamic properties, including vorticity and mixing fractions, are discussed in detail.

In Chapter 5, the content of this study is concluded. Numerical limitations and future work are noted.

CHAPTER 2 Numerical method

Numerical simulations are conducted to provide detailed insights into the flowfields under ISBI and RSBI scenarios. In this work, a compressible multi-component model is established in an in-house multi-block parallel finite-volume CFD solver. In this chapter, the details of the compressible multi-component model, including the governing equations, thermodynamic and transport properties, and chemical reaction models, are presented first. The numerical method applied to the ISBI and RSBI cases is then validated with experimental results.

2.1. Numerical models

2.1.1. Governing equations

In this study, the reactive compressible flow is simulated using the compressible multi-component Navier-Stokes equations. In a 2-D Cartesian coordinate system, the governing equations for the reactive flow with n_s species can be expressed as follows [72], [73], [74]:

$$\frac{\partial \boldsymbol{U}}{\partial t}+\frac{\partial \boldsymbol{F}}{\partial x}+\frac{\partial \boldsymbol{G}}{\partial y}=\frac{\partial \boldsymbol{F}_v}{\partial x}+\frac{\partial \boldsymbol{G}_v}{\partial y}+\boldsymbol{S}_c \tag{2-1}$$

The conservative variable $\boldsymbol{U}$ and inviscid fluxes $\boldsymbol{F}$、$\boldsymbol{G}$ are given by:

$$\boldsymbol{U}=\begin{bmatrix}\rho_1\\ :\\ \rho_{n_s}\\ \rho u\\ \rho v\\ E\end{bmatrix},\boldsymbol{F}=\begin{bmatrix}\rho_1 u\\ :\\ \rho_{n_s} u\\ \rho u^2+p\\ \rho uv\\ (E+p)u\end{bmatrix},\boldsymbol{G}=\begin{bmatrix}\rho_1 v\\ :\\ \rho_{n_s} v\\ \rho uv\\ \rho v^2+p\\ (E+p)v\end{bmatrix} \tag{2-2}$$

where ρ_i $(i=1-n_s)$ denotes the density of each species.

The definitions of the viscous fluxes $\boldsymbol{F}_v$, $\boldsymbol{G}_v$ and the chemical source term $\boldsymbol{S}_c$ are as follows:

$$\boldsymbol{F}_v=\begin{bmatrix}-J_{1,x}\\ :\\ -J_{n_s,x}\\ \tau_{xx}\\ \tau_{xy}\\ u\tau_{xx}+v\tau_{xy}-q_x-\sum_{i=1}^{n_s}J_{i,x}h_i\end{bmatrix},\boldsymbol{G}_v\begin{bmatrix}-J_{1,y}\\ :\\ -J_{n_s,y}\\ \tau_{xy}\\ \tau_{yy}\\ u\tau_{xy}+v\tau_{yy}-q_y-\sum_{i=1}^{n_s}J_{i,y}h_i\end{bmatrix} \tag{2-3}$$

$$\boldsymbol{S}_c = \begin{bmatrix} \dot{\omega}_1 \\ \vdots \\ \dot{\omega}_{n_s} \\ 0 \\ 0 \\ 0 \end{bmatrix}$$

2.1.2. Equation of state

The equation of state for a thermally perfect gas is defined as follows:

$$p = \sum_{i=1}^{n_s} \rho_i \frac{R_u}{MW_i} T \tag{2-4}$$

The total energy per unit volume of the mixture is given by:

$$E = \sum_{i=1}^{n_s} \rho_i \left(h_i - \frac{R_u}{MW_i} T \right) + \frac{1}{2} \rho (u^2 + v^2) \tag{2-5}$$

with h_i as the species enthalpy, calculated using curve fits of the form:

$$\begin{aligned} \frac{h_i(T)}{R_i T} = & -a_{i,1} T^{-2} + a_{i,2} \frac{\ln T}{T} + a_{i,3} + a_{i,4} \frac{T}{2} \\ & + a_{i,5} \frac{T^2}{3} + a_{i,6} \frac{T^3}{4} + a_{i,7} \frac{T^4}{5} + \frac{b_{i,1}}{T} \end{aligned} \tag{2-4}$$

The coefficients $a_{i,k}$ and $b_{i,1}$ are obtained from the NASA thermochemical polynomial data [74]. The species specific heat at constant pressure $C_{p,i}$ and entropy S_i are evaluated using similar curve fits.

2.1.3. Transport properties

When neglecting the bulk viscosity effect, the viscous stresses are expressed as follows:

$$\begin{aligned} \tau_{xx} &= \frac{2}{3} \mu \left(2 \frac{\partial u}{\partial x} - \frac{\partial v}{\partial y} \right) \\ \tau_{yy} &= \frac{2}{3} \mu \left(2 \frac{\partial v}{\partial y} - \frac{\partial u}{\partial x} \right) \\ \tau_{xy} &= \tau_{yx} = \mu \left(\frac{\partial u}{\partial y} + \frac{\partial v}{\partial x} \right) \end{aligned} \tag{2-5}$$

with μ represents the mixture viscosity, which is computed using Wilke's mixing rule [75]:

$$\mu = \sum_{i=1}^{n_s} \frac{X_i}{\phi_i} \mu_i \tag{2-6}$$

The term ϕ_i is given by:

$$\phi_i = \sum_{m=1}^{n_s} \frac{X_m \left\{1 + \sqrt{\frac{\mu_i}{\mu_m}} \left(\frac{MW_m}{MW_i}\right)^{1/4}\right\}^2}{\sqrt{8\left(1 + \frac{MW_i}{MW_m}\right)}} \tag{2-9}$$

The viscous coefficient of each species μ_i is calculated based on the Chapman-Enskog viscosity model [76]:

$$\mu_i = 2.6693 \cdot 10^{-6} \frac{\sqrt{MW_i T}}{\Omega_{\mu,i} {\sigma_i}^2} \tag{2-10}$$

The collision integral $\Omega_{\mu,i}$ [77] is given by:

$$\Omega_{\mu,i} = A(T_i^*)^B + C\exp\left(DT_i^*\right) + \mathrm{E}\exp(FT_i^*) \tag{2-11}$$

with A = 1.16145, B = −0.14874, C = 0.52487, D = −0.7732, E = 2.16178, F = −2.43787, and $T_i^* = T/(\varepsilon/k)_i$.

The thermal conduction is modeled based on the Fourier law:

$$\begin{aligned} q_x &= -\kappa \frac{\partial T}{\partial x} \\ q_y &= -\kappa \frac{\partial T}{\partial y} \end{aligned} \tag{2-12}$$

where κ is the thermal conductivity of the mixture, also calculated with Wilke's mixing rule [75]:

$$\kappa = \sum_{i=1}^{n_s} \frac{X_i}{\phi_i} \kappa_i \tag{2-13}$$

The thermal conductivity of each species κ_i is derived using Eucken's relation [78]:

$$\kappa_i = \left(C_{p,i} + \frac{5}{4}\frac{R_u}{MW_i}\right)\mu_i \tag{2-14}$$

The diffusion terms of species i are expressed as follows:

$$\begin{aligned} J_{i,x} &= -\rho\left(D_i \frac{\partial Y_s}{\partial x} - Y_i \sum_{m=1}^{n_s} D_m \frac{\partial Y_m}{\partial x}\right) \\ J_{i,y} &= -\rho\left(D_i \frac{\partial Y_s}{\partial y} - Y_i \sum_{m=1}^{n_s} D_m \frac{\partial Y_m}{\partial y}\right) \end{aligned} \tag{2-15}$$

where Y_i is the species mass fraction, and D_i represents the species diffusion coefficient, modelled as:

$$D_i = (1 - X_i)\left(\sum_{j \neq i}^{n_s} \frac{X_j}{D_{ij}}\right)^{-1} \quad \textbf{(2-16)}$$

The constitutive empirical law is used to compute the binary diffusion coefficient D_{ij} [79], which is given by:

$$D_{ij} = \frac{0.0266}{\Omega_{D,ij}} \frac{T^{3/2}}{p\sqrt{M_{ij}}\sigma_{ij}^2} \quad \textbf{(2-17)}$$

where $M_{ij} = \frac{2}{\frac{1}{M_i}+\frac{1}{M_j}}$, and $\sigma_{ij} = \frac{\sigma_i+\sigma_j}{2}$. The collision integral for binary diffusion is expressed as:

$$\Omega_{D,ij} = A^*\left(T_{ij}^*\right)^{B^*} + C^* \exp\left(D^* T_{ij}^*\right) + E^* \exp\left(F^* T_{ij}^*\right) + G^* \exp\left(H^* T_{ij}^*\right) \quad \textbf{(2-18)}$$

where $A^* = 1.06036$, $B^* = -0.1561$, $C^* = 0.19300$, $D^* = -0.47635$, $E^* = 1.03587$, $F^* = -1.52996$, $G^* = 1.76474$, $H^* = -3.89411$, and $T_{ij} = T/T_{\varepsilon_{ij}}$, with $T_{\varepsilon_{ij}}$ obtained from the Lennard-Jones potential parameter [11]:

$$T_{\varepsilon_{ij}} = \sqrt{\left(\frac{\varepsilon}{k}\right)_i \left(\frac{\varepsilon}{k}\right)_j} \quad \textbf{(2-19)}$$

2.1.4. Chemical reaction model

The general representation of a chemical reaction mechanism with n_r elementary reactions can be written as:

$$\sum_{i=1}^{n_s} v_{m,i}^f X_i \leftrightarrow \sum_{i=1}^{n_s} v_{m,i}^b X_i, m = 1, \ldots, n_r \quad \textbf{(2-20)}$$

The mass production rate of each species, ω_i, is calculated as a summation of all elementary reactions:

$$\omega_i = W_i \sum_{i=1}^{n_r} \Gamma_r\left(v_{m,i}^b - v_{m,i}^f\right)\left[k_{f,m}\prod_{j=1}^{n_s}\left(C_j\right)^{v_{m,j}^f} - k_{b,m}\prod_{j=1}^{n_s}\left(C_j\right)^{v_{m,j}^b}\right] \quad \textbf{(2-21)}$$

Here, $k_{f,m}$ and $k_{b,m}$ are forward and backward rate coefficients, defined as:

$$k_{f,m} = A_{f,m} T^{B_{f,m}} \exp\left(-\frac{E_{f,m}}{R_u T}\right) \quad \textbf{(2-22)}$$

$$k_{b,m} = \frac{k_{f,m}}{K_{c,m}} \quad \textbf{(2-23)}$$

The equilibrium constant $K_{c,m}$ is evaluated by:

$$K_{c,m} = \exp\left(-\frac{\Delta G_m^0}{R_u T}\right)\left(\frac{R_u T}{p_{\text{atm}}}\right)^{\Sigma_i\left(v_{r,i}^f - v_{r,i}^b\right)} \quad \textbf{(2-24)}$$

where p_{atm} = 1 atm.

The hydrogen-air reaction mechanism in this study is based on Jachimowski's model [80], composed of 9 species and 19 elementary reactions, as outlined in Table 2-1. For the third-body efficiencies, the following values are specified: In Reaction 6 and Reaction 7, the third-body efficiency of H_2O is 6.0 and the coefficients of other species are 1.0. In Reaction 8, the third-body efficiency of H_2O is 5.0 and the coefficients of other species are 1.0. In Reaction 9, the third-body efficiencies are 16.0 for H_2O and 2.0 for H_2 and the coefficients of other species are 1.0. In Reaction 19, the third-body efficiency of H_2O is 15.0 and the coefficients of other species are 1.0. For all remaining species not listed above, the third-body efficiency is assumed to be 0.0.

Table 2-1. Hydrogen-air reaction mechanism.

Reaction		$A_{f,m}$ ($\mathrm{m^3/(mol \cdot s)}$)	$B_{f,m}$	$\frac{E_{f,m}}{R_u}$
1	$H_2 + O_2 = HO_2 + H$	1.0×10^{14}	0.0	28197.38
2	$H + O_2 = OH + O$	2.6×10^{14}	0.0	8459.21
3	$H_2 + O = OH + H$	1.8×10^{10}	1.0	4481.37
4	$H_2 + OH = H + H_2O$	2.2×10^{13}	0.0	2593.15
5	$OH + OH = O + H_2O$	6.3×10^{12}	0.0	548.84
6	$H + OH + M = H_2O + M$	2.2×10^{22}	−2.0	0.0
7	$H + H + M = H_2 + M$	6.4×10^{17}	−1.0	0.0
8	$H + O + M = OH + M$	6.0×10^{16}	−0.6	0.0
9	$H + O_2 + M = HO_2 + M$	2.1×10^{15}	0.0	−503.52
10	$O + O + M = O_2 + M$	6.0×10^{13}	0.0	906.34
11	$HO_2 + H = OH + OH$	1.4×10^{14}	0.0	543.81
12	$HO_2 + H = H_2O + O$	1.0×10^{13}	0.0	543.81
13	$HO_2 + O = O_2 + OH$	1.5×10^{13}	0.0	478.35
14	$HO_2 + OH = H_2O + O_2$	8.0×10^{12}	0.0	0.0
15	$HO_2 + HO_2 = H_2O_2 + O_2$	2.0×10^{12}	0.0	0.0
16	$H + H_2O_2 = H_2 + HO_2$	1.4×10^{12}	0.0	1812.69
17	$O + H_2O_2 = H_2 + HO_2$	1.4×10^{13}	0.0	3222.56
18	$OH + H_2O_2 = H_2O + HO_2$	6.1×10^{12}	0.0	720.04
19	$H_2O_2 + M_2 = OH + OH + M$	1.2×10^{17}	0.0	22910.37

To simulate the evolution of inert and reactive shock-bubble interaction, we employ an in-house multi-block parallel finite-volume CFD code named PHAROS [81], [82], [83], which has been successfully applied to supersonic/hypersonic over capsule, double-cone, hollow-cylinder/flare, and double-wedge configurations. The detailed computational process of the solver is illustrated in Figure 2-1. When solving the Riemann problems, the Godunov-type methods have been applied to estimate the inviscid fluxes due to their robustness and usefulness in computing flows with complex shock structures. The original Harten-Lax-van Leer (HLL) solver simplifies the Riemann problem to two waves, with a single average state in between. Despite its simplicity, this approach is notably dissipative. The Harten-Lax-van Leer Contact (HLLC) solver [84] is an extension of the HLL scheme, which reduces the dissipation by restoring a contact discontinuity to the theoretical wave structure. The Godunov-type method is inherently free of spurious oscillations around shock waves but is restricted to first-order accuracy. To address this limitation, the monotone upstream-centered scheme for conservation law (MUSCL) reconstruction and the Weighted Essential Non-Oscillation reconstruction (WENO) are applied, achieving second-order and fifth-order accuracy in smooth parts of the flow while not interfering with the region of any discontinuity. The Van Leer limiter, which provides the best accuracy and reliability, is used in the MUSCL [85]. Viscous fluxes are calculated using a second-order central scheme. Temporal integration is conducted by using a three-step third-order Runge-Kutta method [86].

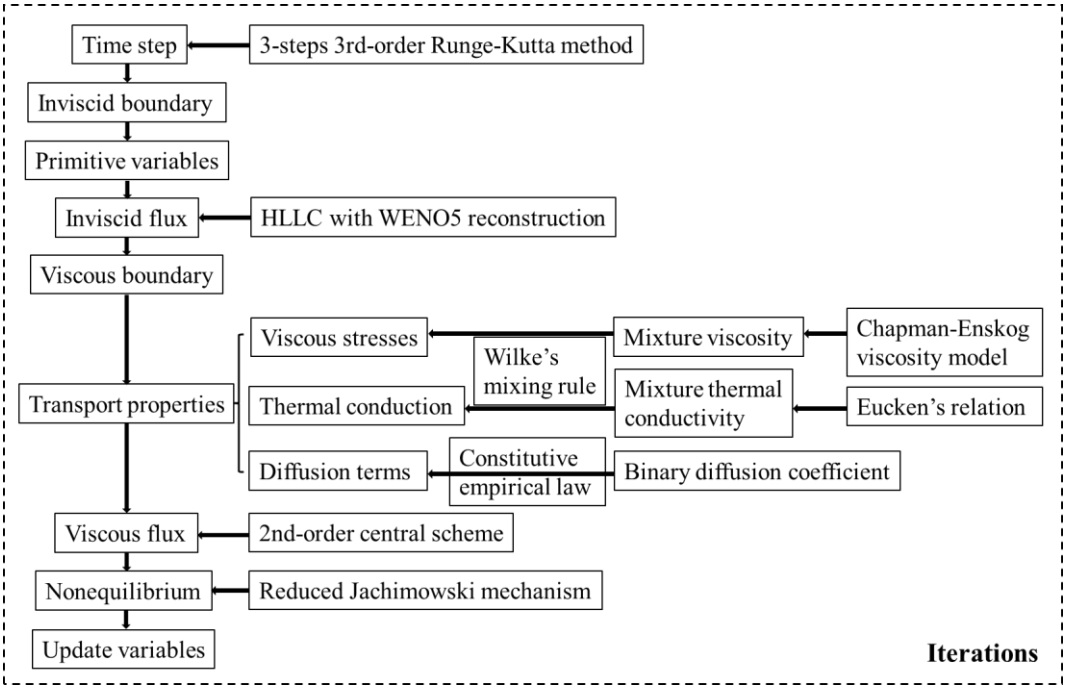

Figure 2-1. The detailed computational process of PHAROS.

2.2. Numerical method validation

2.2.1. Applications for inert shock-bubble interaction

As shown in Figure 2-2, the computational domain of inert shock-bubble interaction is a two-dimensional rectangle with a length of 275 mm and a width of 68 mm. The boundary conditions on the left and right boundaries are specified as inlet and outlet, while the lower and upper boundaries are set as symmetry and slip wall conditions. The center of the bubble is defined as the coordinate origin (0, 0). The radii of the outer and inner cylinders are 28 mm and 14 mm, respectively. The poles are defined as the intersection points of the symmetry axis with the interfaces of the double-layer gas cylinder. The incident shock (IS) propagates downstream from the left boundary. The moment when it reaches the upstream pole of the outer cylinder is denoted as t = 0, where t represents the physical time. A nondimensional time τ can be scaled by tW_i/D. The initial conditions are consistent with the experimental settings outlined in Table 3-1, which encompass an initial IS Mach number of 1.27, initial temperature T = 293 K, and initial pressure p = 101,325 Pa. The surrounding medium is set to ambient air. The outer gas ring comprises 50% SF_6 and 50% ambient air in volume fraction, while the inner gas cylinder comprises 5% SF_6 and 95% ambient air.

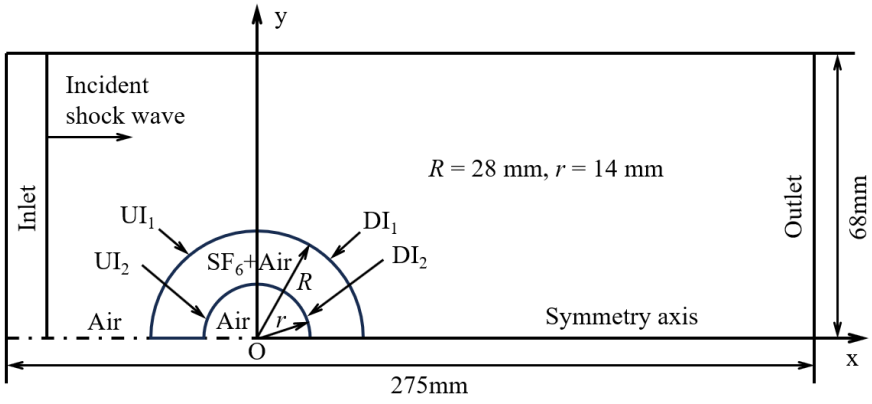

Figure 2-2. Schematic of the computational domain for inert double-layer gas cylinder.

Figure 2-3 provides a comparison between the numerical schlieren images and experimental results [43]. The results reveal that the morphologies of the gas cylinder and the position of shock waves agree with the experimental data. In addition, Figure 2-4 and Figure 2-5 illustrate the comparison of the calculated widths and heights for both the outer and inner cylinders, marking the error bars between the numerical and experimental results. It can be observed that the calculated widths and heights are in good alignment with the experimental

results. Through qualitative and quantitative comparisons, this numerical method is suitable for simulating the interaction between the IS and the double-layer gas cylinder.

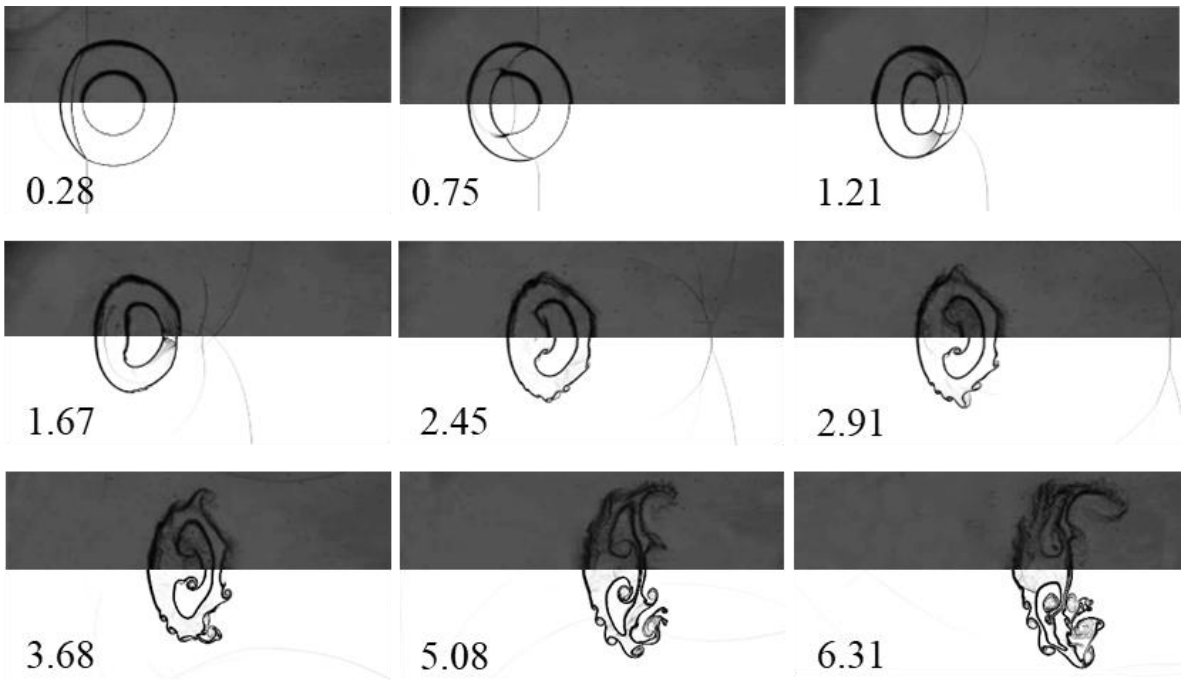

Figure 2-3. Comparison of numerical schlieren images at different time sequences with the experimental results from Ref. [43]**. The upper regions depict the experimental results, and the lower regions depict the numerical results.**

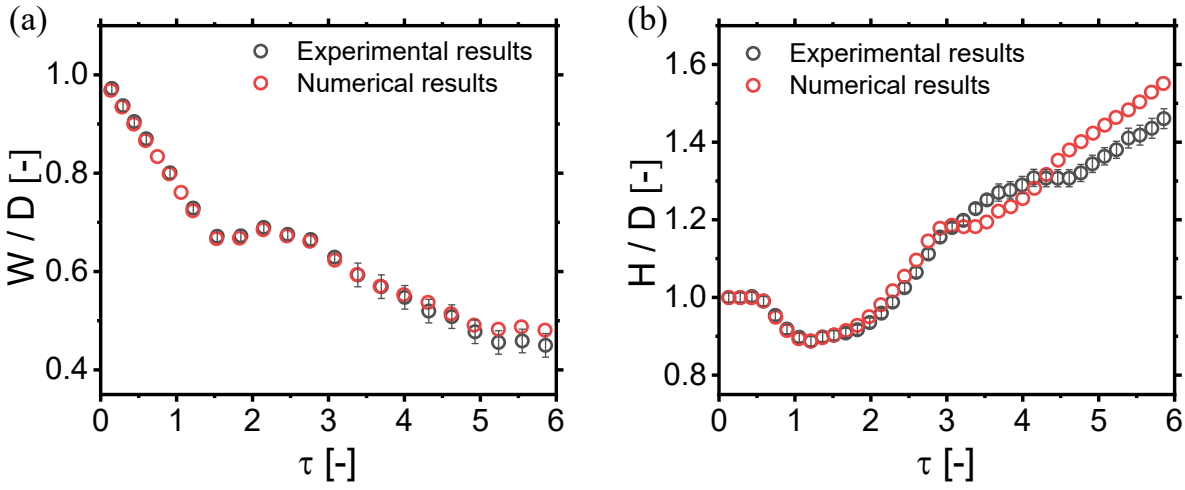

Figure 2-4. Comparison of the calculated (a) widths and (b) heights for outer cylinders with the experimental results [43]**.**

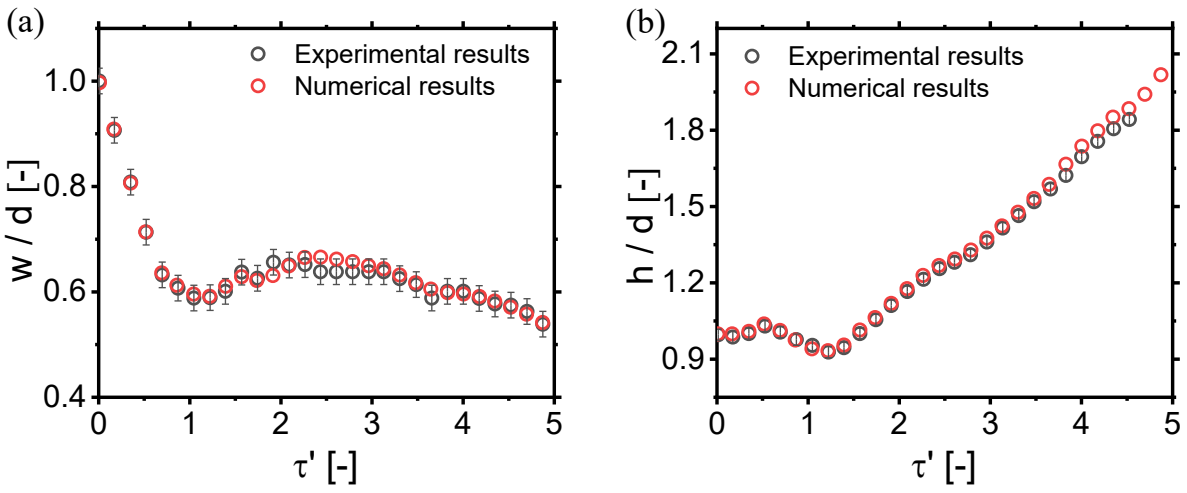

Figure 2-5. Comparison of the calculated (a) widths and (b) heights for inner cylinders with the experimental results [43].

2.2.2. Applications for reactive shock-bubble interaction

Figure 2-6 shows the 2-D computational domain for the reactive shock-double layer cylinder interactions. The left, right, upper, and lower boundaries are set as inlet, outlet, slip wall boundary and symmetry conditions, respectively. The physical time t = 0 μs is defined as the moment when the IS reaches the upstream interface (UI_1) of the double-layer gas cylinder. The center of the gas cylinder is located at the coordinate origin (0,0). The radius of the bubble is 0.02 m. The ambient gas is pure N_2, while the gas in the gas bubble is a mixture of H_2, O_2, and Xe in a ratio of 2:1:3.67 molar fractions.

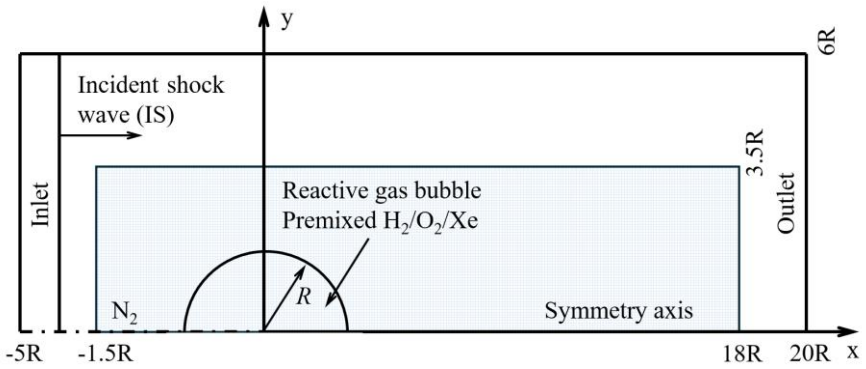

Figure 2-6. Schematic of the computational domain for a reactive single-layer spherical gas bubble.

To validate the accuracy of the numerical simulations, the results for a reactive single-layer gas cylinder and a reactive single-layer spherical gas bubble are compared with the numerical results from Diegelmann et al. [56] and the experimental data from Haehn et al. [54]. For the reactive single-layer gas cylinder, the Mach number of the IS is 2.3, with the

initial pressure and temperature given as 0.5atm and 350K. Figure 2-7 compares the calculated temperature contours with those from Diegelmann's study. In Diegelmann's work, the physical time at which the IS begins to propagate is defined as t = 0. As the IS reaches UI1, the physical time is 26 μs, which is 26 μs ahead of the physical time in our simulations. The ignition time obtained in this work is 58 μs, differing from the reference by only 2 μs. The ignition locations can be observed near the downstream interface in both cases. At 94 μs and 480 μs, heat release, temperature distribution and the morphologies of gas cylinders are in good agreement with the reference results. Figure 2-8 compares the numerical normalized transverse bubble diameters with the reference results [56], demonstrating good agreement.

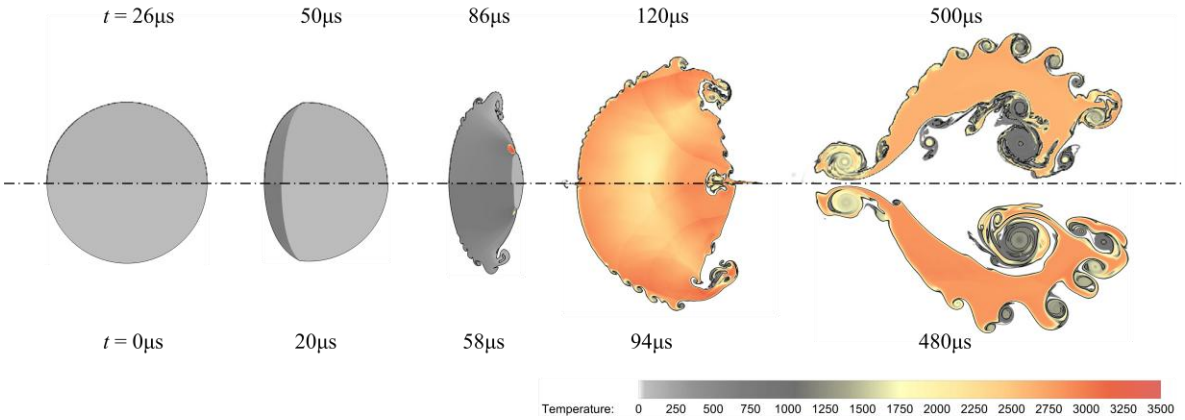

Figure 2-7. Temperature contours of RSBI cases. The upper region depicts the results from [56]**, while the lower region depicts the results of this study.**

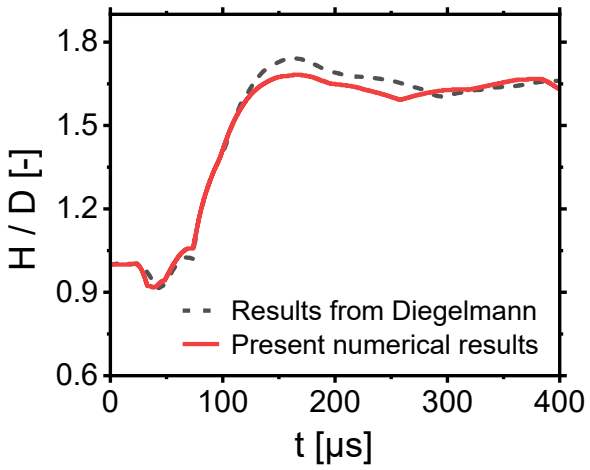

Figure 2-8. Comparison of the numerical normalized transverse bubble diameters with the reference [56]**.**

For the reactive single-layer spherical gas bubble, we compare the numerical method with the experimental results from Haehn [54] to validate its accuracy. The initial conditions

are consistent with those employed in the experiments, which are conducted under STP. Incident shock Mach numbers are set to 2.07 and 2.83, leading to the formation of deflagration and detonation waves, respectively. Figure 2-9 presents the comparison between the normalized transverse bubble diameter and the experimental data. In the case of M = 2.07, the numerical results exhibit a smaller transverse bubble diameter during the early-stage evolution, but the overall trend of the curve agrees well with the experimental observations. In the case of M = 2.83, since the pre-shock transverse bubble diameter deviates from the experimental values by approximately 4%, the simulated initial bubble diameter is adjusted to the average of the experimental measurements from Haehn [54]. The numerical results show good agreement with the experimental data during the early stages of evolution. In the later stages, the trend of the curves also aligns with the experimental observations, further confirming the accuracy of this numerical method.

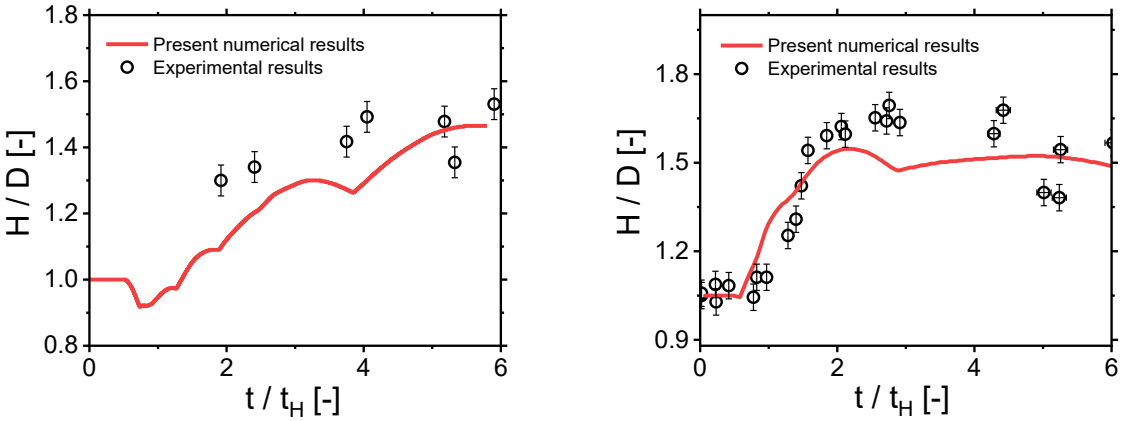

Figure 2-9. Comparison of the numerical normalized transverse bubble diameters with the experimental results from [38]. (a) Deflagration: M = 2.07, (b) Detonation: M = 2.83.

CHAPTER 3 Evolution of an inert double-layer gas cylinder

In this chapter, the computational setups for different Mach numbers and Atwood numbers are introduced first. The grid independence study is verified using the GCI method and density distribution along the symmetry axis. Subsequently, the impacts of varying Mach numbers and Atwood numbers on the evolution of a double-layer gas cylinder are analyzed qualitatively. The compressibility effects are quantified by the widths and heights of the gas cylinders. The mechanism behind vorticity evolution is investigated using the vorticity transport equation. Net circulation is compared with existing circulation models. Gas mixing is also examined through the analysis of mean mass fraction evolution.

3.1. Computational setups

The computational domain is a two-dimensional rectangle with a length of 275 mm and a width of 68 mm, as illustrated in Figure 3-1. To improve computational efficiency, the domain is set to half of the test section. The initial conditions are consistent with the experimental settings outlined in Table 3-1, which encompass an initial IS Mach number of 1.27, initial temperature T = 293 K, and initial pressure p = 101,325 Pa. The surrounding medium is set to ambient air, and the gas ring contains a mixture composed of the selected gas and air. To independently track the evolution of the outer and inner cylinders, the selected gas in the inner cylinder is replaced by a hypothetical gas, which retains identical physical properties. By monitoring the mass fractions of the selected gas in the gas ring and the corresponding hypothetical gas in the inner cylinder, the distinct physical characteristics and behaviours of the outer and inner cylinders can be effectively identified. The outer and inner interfaces can be defined in terms of the molar fraction of the ambient gas and the mixture in the inner cylinder:

$$X_{\mathrm{Air}} = \frac{1 + \tanh\left(\left(\sqrt{x^2 + y^2} - R\right) \cdot \sigma\right)}{2}$$
$$X_{inner} = \frac{1 - \tanh\left(\left(\sqrt{x^2 + y^2} - r\right) \cdot \sigma\right)}{2} \quad \textbf{(3-1)}$$

where the parameter σ, which controls the steepness, is set to 2×10^4 [55]. The molar fraction of the mixture within the gas ring is then given by $X_{\mathrm{outer}} = 1 - X_{\mathrm{Air}} - X_{\mathrm{inner}}$.

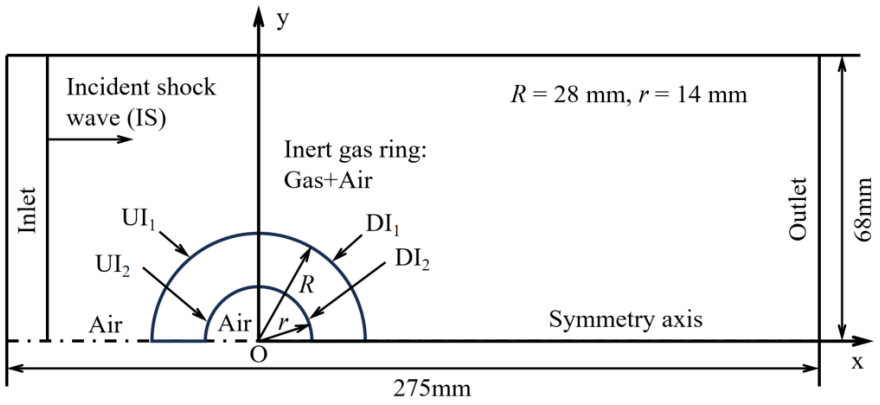

Figure 3-1. Schematic of the computational domain for inert double-layer gas cylinder.

Table 3-1. Physical settings in the numerical simulation.

M	R (mm)	r (mm)	T (K)	p (Pa)
1.27	28	14	293	101,325

For the scenarios of varying Mach numbers, different intensities of the IS (M = 1.27, 1.5, 1.7, and 2.1) are considered in this study. The outer gas ring comprises 50% SF_6 and 50% ambient air in volume fraction, while the inner gas cylinder comprises 5% SF_6 and 95% ambient air, which are consistent with the experimental conditions [43]. Further details regarding the physical properties of various gases are cataloged in Table 3-2.

Table 3-2. Physical properties of different gases at the initial condition.

Gas	Density ($kg \cdot m^{-3}$)	Specific heat ratio	Sound speed ($m \cdot s^{-1}$)	Acoustic impedance ($kg \cdot m^{-2} \cdot s^{-1}$)	Molecular weight ($g \cdot mol^{-1}$)
Air	1.20	1.4	343	412	28.965
SF_6	6.14	1.1	136	835	146.055

In terms of Atwood number effects, two types of gas layer configurations are considered: an A/B/A-type gas layer (where the densities in the surroundings, gas ring, and inner cylinder are denoted as A, B, and A) and an A/B/C-type gas layer (where the densities in the surroundings, gas ring, and inner cylinder are denoted as A, B, and C). For the scenarios of an A/B/A−type gas cylinder, different gases (SF_6, Kr, CO_2, and He) in the gas ring are conducted in this study. The gas ring contains a mixture composed of the selected gas and air. The volume fraction of this gas within the gas ring and inner cylinder are 0.5 and 0.05, respectively. Physical properties regarding air and different gases are presented in Table 3-3. The Atwood numbers for different layers can be calculated according to Equation (1-4),

where ρ_1 *and* ρ_2 pertain to the densities of the ambient gas and the inside the gas ring for the first layer gas cylinder (A_1), while ρ_1 and ρ_2 denote the densities of the gas inside the gas ring and inner cylinder for the second layer gas cylinder (A_2), as listed in Table 3-4.

Table 3-3. Physical properties of different gases at the initial condition.

Gas	Density ($kg \cdot m^{-3}$)	Specific heat ratio	Sound speed ($m \cdot s^{-1}$)	Acoustic impedance ($kg \cdot m^{-2} \cdot s^{-1}$)	Molecular weight ($g \cdot mol^{-1}$)
Kr	3.49	1.67	220	768	83.800
CO_2	1.83	1.3	259	474	44.010
He	0.17	1.67	972	165	4.003

Table 3-4. The corresponding Atwood numbers and flow patterns for four configurations combined by air and various gases.

Configuration	The first layer		The second layer	
	A_1	Flow pattern	A_2	Flow pattern
Air-SF_6-Air	0.50	Convergent	−0.50	Divergent
Air-Kr-Air	0.39	Convergent	−0.39	Divergent
Air-CO_2-Air	0.19	Convergent	−0.19	Divergent
Air-He-Air	−0.20	Divergent	0.20	Convergent

For the scenarios of an A/B/C−type gas cylinder, the gas in the gas ring is a mixture comprising 50% air and 50% SF_6 in volume fraction, and the concentrations of SF_6 (ranging from 5% to 80% in volume fraction) are adjusted in the inner cylinder in this study. Table 3-5 lists the physical properties of the mixture at various layers, along with their corresponding Atwood numbers. With an increase in the concentrations of SF_6 in the inner cylinder, both the densities of the mixed gases and their Atwood numbers rise, while the specific heat ratios decrease. When VF_2 approaches VF_1, the absolute value of the Atwood numbers gets smaller.

Table 3-5. Physical properties of different gases at different layers.

Case		I	II	III	IV	V
Ambient gas (Air)	Density ($kg \cdot m^{-3}$)	1.20				
	Specific heat ratio	1.4				

Outer cylinder (0.5 Air+0.5 SF_6)	Density ($kg \cdot m^{-3}$)	3.65				
	Specific heat ratio	1.16				
	Atwood number for the first layer (A_1)	0.50				
Inner cylinder (VF_1 Air+VF_2 SF_6)	VF_2	0.05	0.2	0.4	0.6	0.8
	Density ($kg \cdot m^{-3}$)	1.45	2.19	3.17	4.14	5.11
	Specific heat ratio	1.35	1.25	1.18	1.14	1.12
	Atwood number for the second layer (A_2)	−0.43	−0.25	−0.07	0.06	0.17

3.2. Grid independence study

Grid independence is verified using uniform meshes with various sizes of 0.1 mm, 0.2 mm, and 0.4 mm, which are labelled Meshes I–III. By comparing the density distribution along the symmetry axis at t = 120 μs, it can be observed that there is a convergence in the curve of density distribution as the mesh resolution increases in Figure 3-2. The Richardson extrapolation is introduced to quantitatively analyze the grid convergence. Starting with the series solution of the discretization error,

$$f = f_{\text{exact}} + g_1 h + g_2 h^2 + O(h^3) \quad \textbf{(3-2)}$$

Equation (3-2) can be generalized for a p-th order method and r-value of mesh ratio as:

$$f_{\text{exact}} \cong f_1 + \frac{f_1 - f_2}{z^p - 1} \quad \textbf{(3-3)}$$

where p can be obtained from three solutions using the grid refinement ratio z,

$$p = \ln\left(\frac{f_3 - f_2}{f_2 - f_1}\right) / \ln(z) \quad \textbf{(3-4)}$$

The Grid Convergence Index (GCI) measures the percentage difference between the computed value and the asymptotic numerical value. The GCI on the fine mesh is written as:

$$GCI = \frac{F_s|\varepsilon|}{(rz^p - 1)} \quad \textbf{(3-5)}$$

where F_s is a factor of safety and set to 1.25. It is crucial that the solutions at each grid level must be in the asymptotic range of convergence, which can be checked by:

$$GCI_{2,3} = z^p GCI_{1,2} \quad \textbf{(3-6)}$$

Table 3-6 shows the grid spacing and the density at the intersection point of the symmetry axis and the UI_1 at 120 μs. The value of p is 5.16. The GCI for Meshes I and II and Meshes II and III are 0.016% and 0.588%, respectively. And the calculated ratio of $GCI_{2,3}$

and $z^p GCI_{1,2}$ is 1.00, which is well within the asymptotic range of convergence. Based on the above results, mesh I can be adopted to adequately resolve the flow.

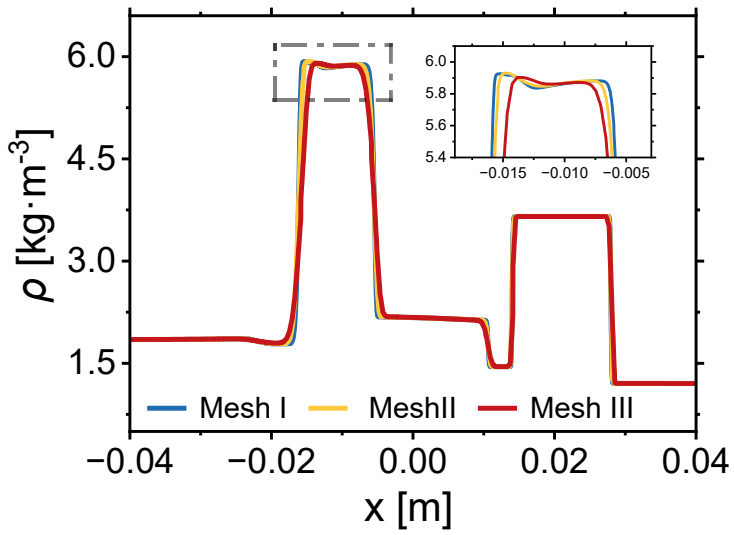

Figure 3-2. Density distributions along the symmetry axis of the double-layer gas cylinder with different mesh sizes.

Table 3-6. Mesh spacing and the density at the intersection point of the symmetry axis and the UI_1 at 120 μs among different meshes. The calculated values of GCI between two meshes.

	Mesh spacing (mm)	Density (kg·m^{-3})	GCI (%)
Mesh I	1	3.74	0.02
Mesh II	2	3.73	0.59
Mesh III	4	3.12	–

3.3. Effects of Mach number on ISBI scenarios

3.3.1. Evolution of the double-layer gas cylinder

Figure 3-3 illustrates the numerical schlieren images at different Mach numbers. With an increase in Mach numbers, there is a noticeable compression effect on UI_1 under the interaction of intense shock waves, mainly acting on the interface's central region (τ = 0.75−1.21). It can be observed that an upstream jet emerges from the upstream pole of the outer cylinder and extends into the ambient air in the following evolution (τ = 2.45−5.08).

Although the jet forms earliest in the case of M = 2.1, its length is shorter compared to cases where M = 1.5 and M = 1.7 in the later phase of the evolution, which requires a detailed investigation in the following section. A similar upstream jet occurs in a double-layer gas cylinder when the radius ratio of the inner cylinder to the outer one is large, and the inner cylinder is positioned upstream [43], [44]. In the scenario of a single-layer gas cylinder, there is only a downstream jet emerging from the downstream pole of the gas interface, which results from the generation of a higher-pressure zone due to the shock focusing inside the gas interface [26]. However, the wave structure is complex within the gas ring due to the presence of the inner cylinder, which contributes to the formation of the secondary vortex pair rather than the downstream jet. Furthermore, the interaction with intense shock waves leads to a substantial quantity of baroclinic vorticity deposited on the interface, accelerating the generation and further development of the primary and secondary vortex pair of the outer cylinder. A similar vortex pair can also be observed in the inner cylinder due to the intense shock wave, shortening the distance between the interfaces connecting the vortex pair and speeding up the coupling with the primary vortex pair of the outer cylinder as the Mach number rises. The numerical schlieren images of the double-layer gas cylinder at varying Mach numbers qualitatively illustrate a significant impact of shock wave intensity on the evolution of the double-layer gas cylinder.

3.3.2. Widths and heights

The extent of compression on the interfaces strongly correlates with the intensity of the IS, as evident in the numerical schlieren images at varying Mach numbers. To quantitatively evaluate the compression at the early stage of evolution, we emphasize the analysis of the normalized widths and heights of the outer and inner gas cylinders (τ = 0−5) in this section.

During the initial phase of evolution (τ = 0−1.22) in Figure 3-4(a), the outer gas cylinder is rapidly compressed due to the interaction with the IS, causing a pronounced reduction in its width as the intensity of the IS rises. As the evolution proceeds, the earlier formation and faster development of the primary vortex pair lead to a notable increase in width. Additionally, the interaction of the intense IS generates an upstream-directed jet structure, as evident in cases of Mach 1.5−2.1, which also contributes to the growth of width.

As illustrated in Figure 3-4(b), the height of the outer cylinder remains relatively unchanged in the initial phase of the interaction between the IS and the double-layer gas cylinder. After passing through the diametral plane of the outer interface, the IS undergoes a transformation into a diffracted shock, leading to the compression of the outer cylinder in the spanwise direction and a consequent reduction in its height. With an increase in the intensity of the IS,

the height of the outer cylinder is compressed more significantly. As the primary vortex pair evolves, the heights of the outer cylinder at higher Mach numbers notably increase, surpassing those observed in the scenario of M = 1.27 after τ = 1.50. Simultaneously, the development of the inner cylinder also promotes the expansion of the outer cylinder outward in the spanwise direction. In the initial phase of evolution, the noticeable reduction in the outer cylinder's width and height highlights the dominant role of the compressibility effect of the intense shock wave during this phase.

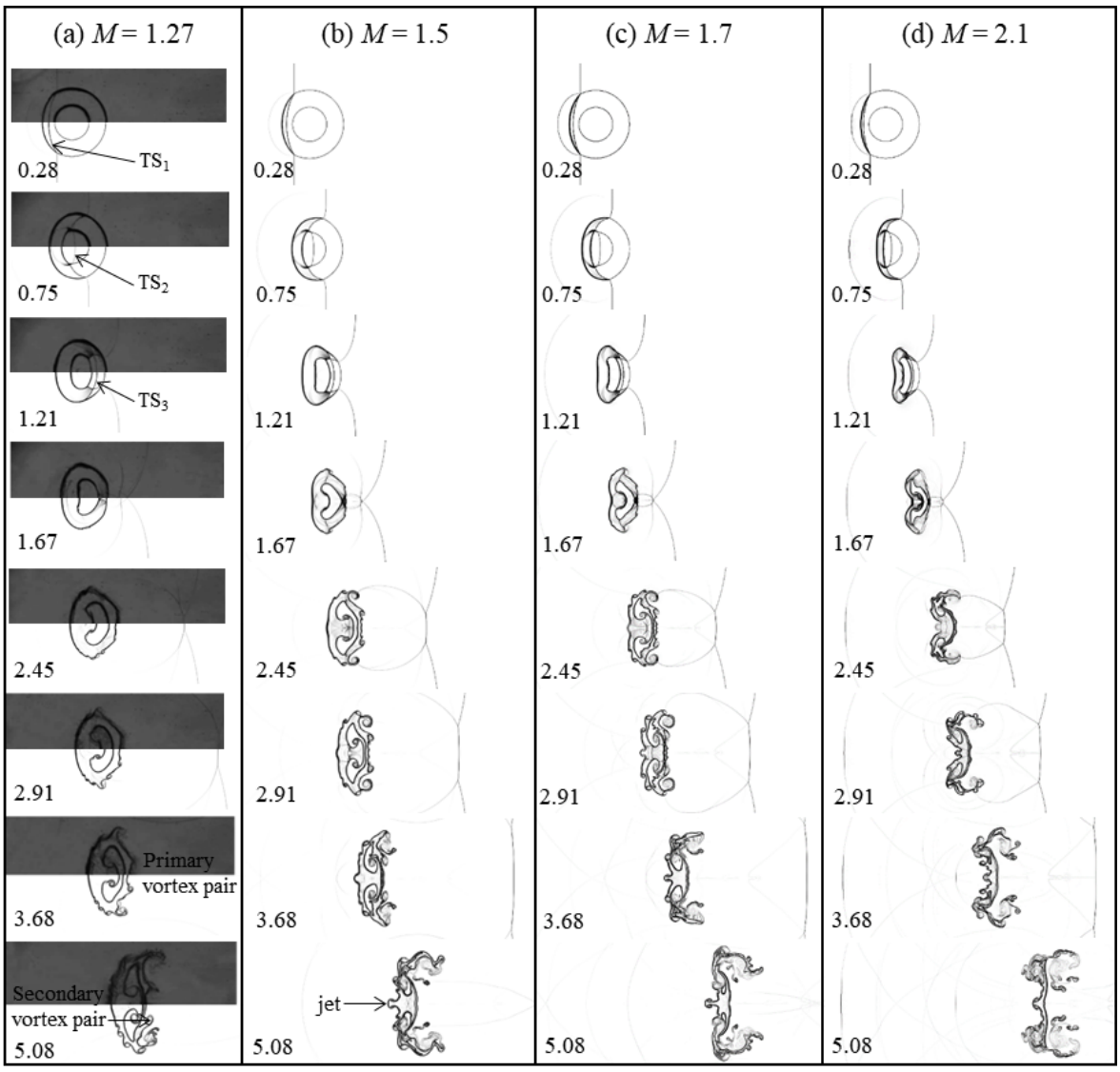

Figure 3-3. Numerical schlieren images of the double-layer gas cylinders for different Mach numbers.

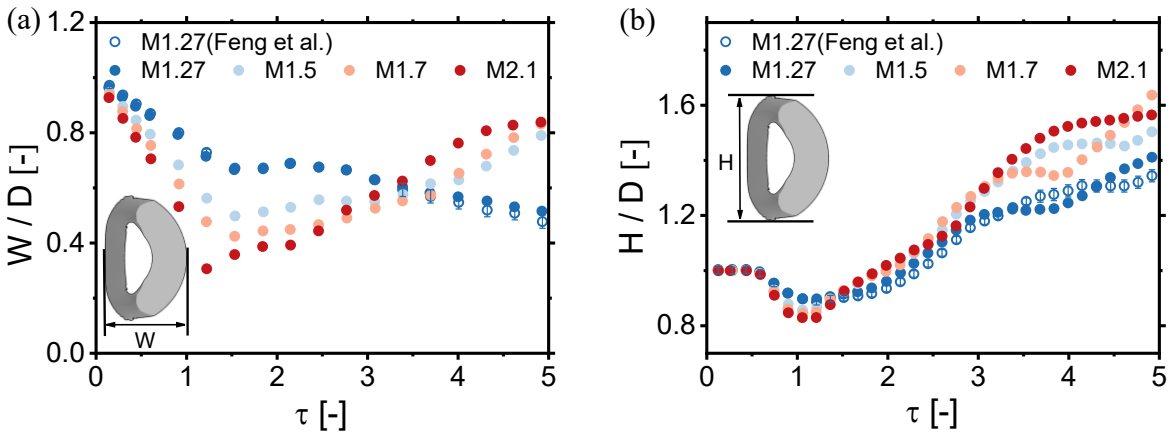

Figure 3-4. Variation of (a) widths and (b) heights of the outer cylinder.

The development of the inner cylinder is impacted by the TS_1 and the evolution of the outer cylinder. The physical time (t) can be normalized by $\tau' = tW_i'/d$. During the initial phase ($\tau' = 0-0.87$), the widths of the inner cylinder undergo compression accompanied by a rapid decline due to the influence of the TS_1 with the IS intensity increasing, as depicted in Figure 3-5(a). This phenomenon occurs as the increased intensity of the TS_1 caused by the intense IS leads to compression on the UI_2. Simultaneously, the intense IS compresses the outer interface, prompting an accelerated downstream displacement and subsequently causing compression on UI_2, which results in a reduction in width. Following this compression phase, the development of the DI_2 and the growth of the vortex pair contribute to an increase in the width of the inner cylinder until it ultimately couples with the outer interface.

The compression of the inner cylinder in the flow direction by the shock wave promotes its spanwise development, contributing to a slight increase in heights at the early stage of the evolution ($\tau' = 0.40-0.75$). The heights are compressed due to the TS_1 passing over the diametral plane of the inner cylinder ($\tau' = 0.75-1.30$). As the intensity of IS increases, the development of the vortex pair in the spanwise direction is further enhanced, resulting in the growth of the heights, as illustrated in Figure 3-5(b). However, at the later stage of evolution, an increase in the intensity of the IS accelerates the coupling between the vortex pair of the inner cylinder and the primary vortex pair of the outer.

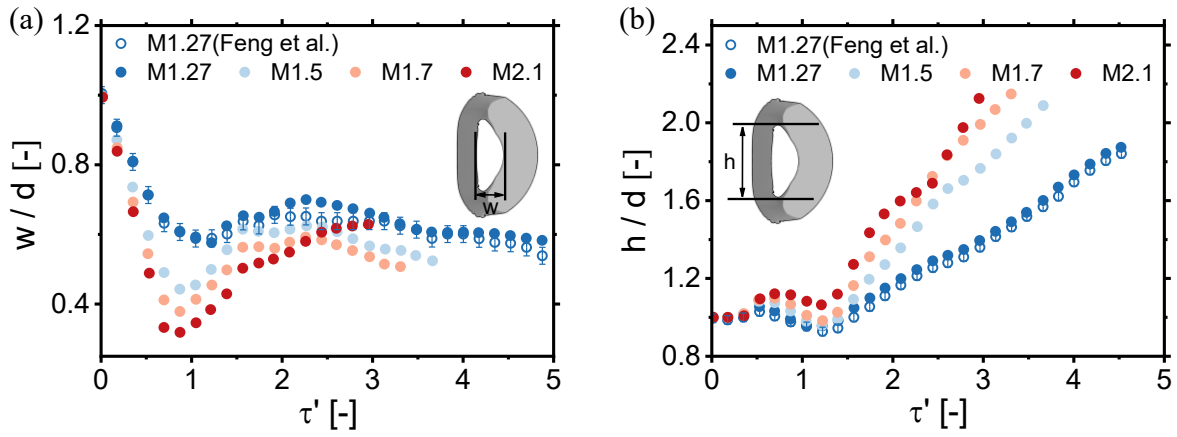

Figure 3-5. Variation of (a) widths and (b) heights of the inner cylinder.

3.3.3. Jet formation

Jet formation is closely connected with the flow morphologies and the mechanisms of shock waves. Many studies on the regular and irregular jet formation of the single-layer gas cylinder have been carried out [23], [24], [26]. However, the mechanism of the upstream jet formation concerning the double-layer gas cylinder remains limited. Analysis of numerical schlieren images indicates that the length of the upstream jet generated at the outer interface of the gas cylinder is highly sensitive to incident shock Mach numbers. To investigate the phenomenon concerning a shorter length of the upstream jet during the later stages under the higher Mach number, the mechanism behind the formation of the upstream jet is discussed in this section. Figure 3-6, Figure 3-7, and Figure 3-8 illustrate the numerical schlieren images and pressure contours for different time sequences at various Mach numbers.

In the case of M = 1.5, it becomes evident that the TS_2 emerges after the TS_1 passes through UI_2. A REW is generated upon the TS_2 colliding with DI_2. Subsequently, an RS inside the inner cylinder moves upstream as the DI_2 is a fast/slow interface relative to the motion of the TS_2 [87], and another shock K forms at this moment. With time progressing, shock K and its symmetric counterpart intersect at point Q and gradually converge into a small region along with RS. The pressure downstream of RS significantly increases following the convergence, as observed in the pressure contours. After the collision of the shock K with each other, RS_1 forms and moves upstream along with RS. Once the reflected shock waves reach UI_2, RS nearly dissipates, and RS_1 transmits into the T_1RS_1, where a downstream high-pressure region is still present. Upon the impingement of T_1RS_1 onto UI_1, a T_2RS_1 emerges, which leads to the generation of the bulge at the center of the UI_1, which develops into the upstream jet afterwards.

Through the quantitative analysis of the compressibility, it can be inferred that as the intensity of IS increases, the width of the inner cylinder is compressed during the initial evolution stages, which results in a region with further convergence of two shock waves Ks and RS moving closer to UI_2. In the case of M = 2.1, the convergence area emerges closely near UI_2, at which point RS has already collided with UI_2 and subsequently transmitted into $T1RS_1$. As T_1RS and T_1RS_1, which have both undergone transmission through UI_2, sweep past UI_1 together, a bulge emerges and eventually evolves into the upstream jet. With increasing Mach number, the pressure in the downstream high-pressure region of the reflected waves continues to rise, leading to the evolution and development of the jet.

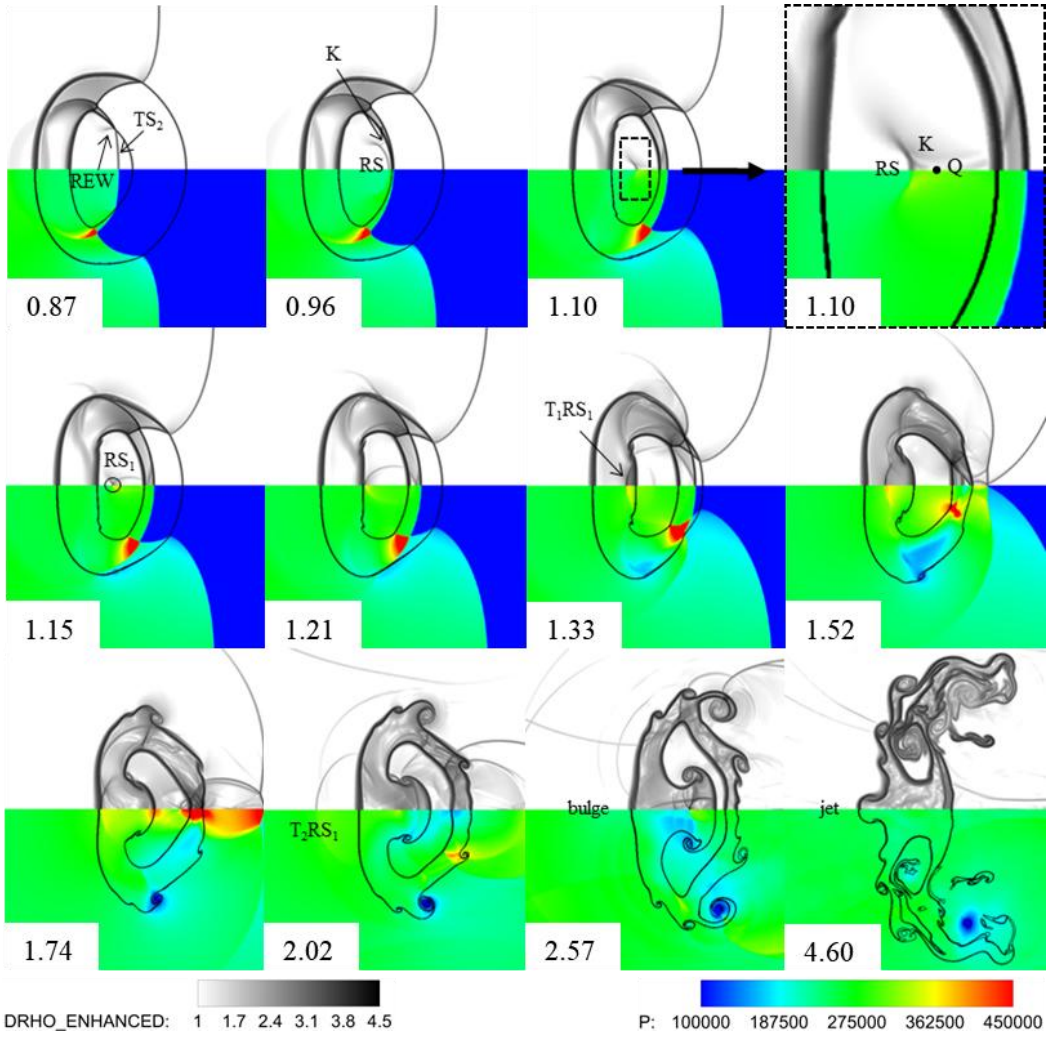

Figure 3-6. Time sequences of numerical schlieren images and pressure contours at Mach 1.5. REW, reflected expansion wave; TS_2, the second transmitted shock wave; RS, reflected shock wave; RS_1, another reflected shock wave; K, a shock wave; T_1RS_1, another first transmitted reflected shock wave; T_2RS_1, another second transmitted reflected shock wave.

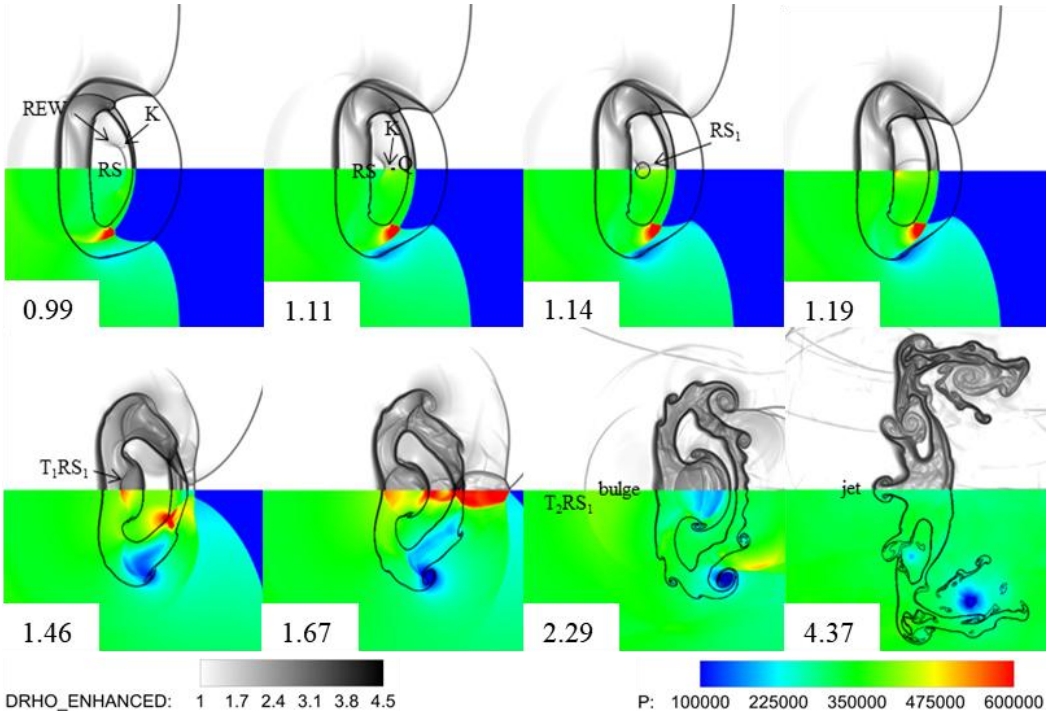

Figure 3-7. Time sequences of numerical schlieren images and pressure contours at Mach 1.7.

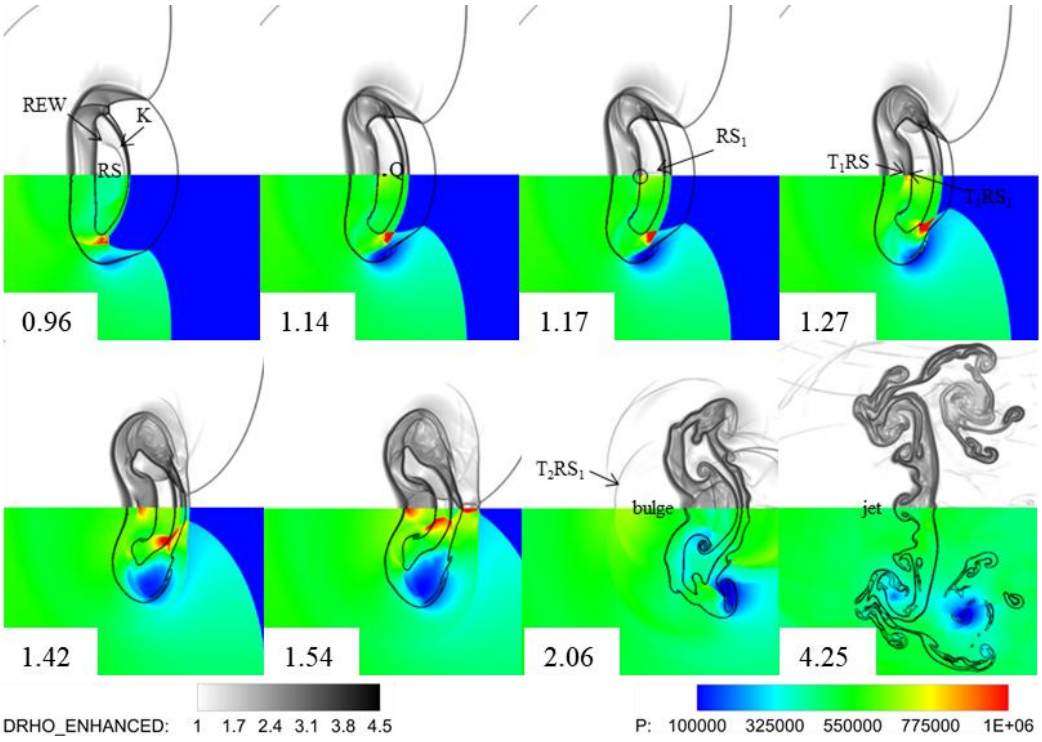

Figure 3-8. Time sequences of numerical schlieren images and pressure contours at Mach 2.1. T_1RS, the first transmitted reflected shock wave.

3.3.4. Vorticity generation

3.3.4.1. Dynamics of vorticity production

During the interaction between the shock waves and the gas cylinder, a large amount of vorticity is deposited at the interfaces, resulting in mixing. Figure 3-9 illustrates the impacts of the Mach number on the vorticity distribution at various time sequences. Initially, the vorticity is uniformly 0. As IS traverses UI_1, baroclinic vorticity is locally deposited on the interface due to the misalignment of the density gradient ($\nabla\rho$) and the pressure gradient (∇p). Owing to the nearly orthogonal orientation of the pressure and density gradients at the diametral plane of both the outer and inner cylinders, a significant amount of vorticity is deposited in these regions, which induces the formation of a large-scale primary vortex pair. The development of RM instability leads to velocity shear and small perturbations at the interfaces, which are necessary preconditions for KH instability [88]. These perturbations are amplified, eventually generating vortices at the interface and promoting the emergence of smaller-scale structures [3].

The initial densities of Air and SF_6 are 1.20 kg/m^3 and 6.14 kg/m^3, respectively. UI_1 corresponds to a light/heavy interface where $\nabla\rho$ directs inwards radially, while UI_2 corresponds to a heavy/light interface where $\nabla\rho$ directs outwards radially. Since ∇p opposes the shock propagation direction, negative vorticity is deposited at the outer interface, while positive vorticity is deposited at the inner interface. With the growth of the Mach number, more vorticity is deposited at both the outer and inner interfaces. At a later stage of evolution, a small amount of vorticity forms around the bubble interface at Mach 1.27, with the rolled-up vortices becoming more distinct at higher Mach numbers. These observations align with the findings in the reference [89].

To have a further understanding of the effects of the Atwood number on the vorticity production, the spatially integrated dilatation, baroclinic, and viscous terms are investigated in detail, which are given by:

$$P_{\omega,\mathrm{dil}} = -\frac{\int_D |\omega(\nabla\cdot u)|dxdy}{\int_D dxdy} = -\frac{\int_D \left|\omega\left(\frac{\partial u}{\partial x}+\frac{\partial v}{\partial y}\right)\right| dxdy}{\int_D dxdy} \tag{3-7}$$

$$P_{\omega,\mathrm{bar}} = \frac{\int_D \left|\frac{1}{\rho^2}(\nabla\rho\times\nabla p)\right| dxdy}{\int_D dxdy} = \frac{\int_D \left|\frac{1}{\rho^2}(\frac{\partial\rho}{\partial x}\frac{\partial p}{\partial y}-\frac{\partial\rho}{\partial y}\frac{\partial p}{\partial x})\right| dxdy}{\int_D dxdy} \tag{3-8}$$

$$P_{\omega,\mathrm{vis}} = \frac{\int_D \left|\frac{\mu}{\rho}\nabla^2\omega\right| dxdy}{\int_D dxdy} = \frac{\int_D \left|\frac{\mu}{\rho}\left(\frac{\partial^2\omega}{\partial x^2}+\frac{\partial^2\omega}{\partial y^2}\right)\right| dxdy}{\int_D dxdy} \tag{3-9}$$

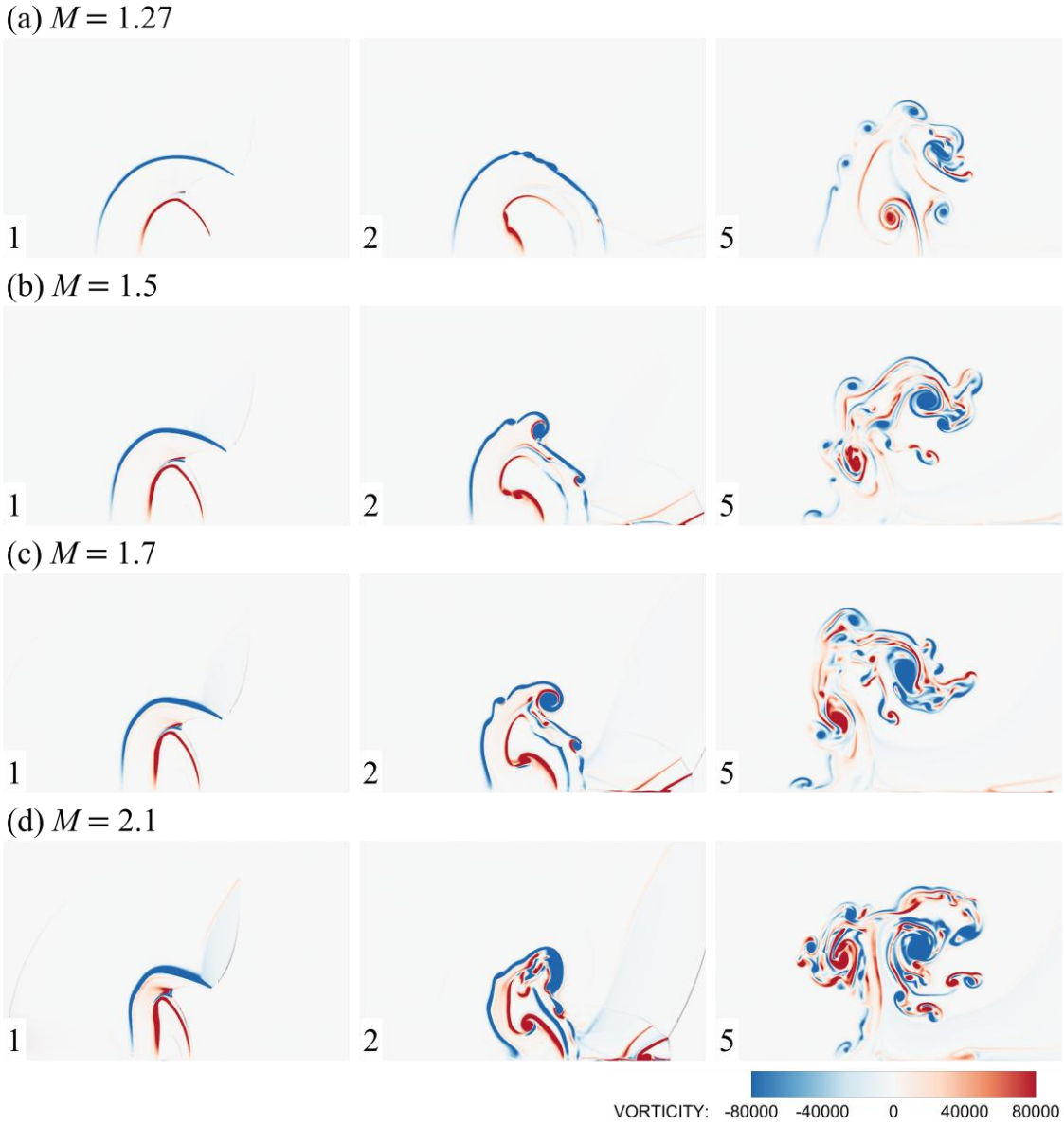

Figure 3-9. Time sequences of vorticity distribution for different Mach numbers.

As illustrated in Figure 3-10, the absolute values of the dilatational and baroclinic terms surpass that of the viscous term, indicating their dominance in vorticity production during the evolution. With the growth of Mach number, the value of the dilatation term increases, implying that the higher Mach numbers result in stronger compression effects. The first peak values of the dilatation term occur after the TP impinges on the DI_1 due to the generation of the secondary vortex pairs and the presence of the stretched structures around the vortex core. The increase in Mach number contributes to the growth of the pressure gradient, leading to a rise in the baroclinic term due to the misalignment of the density and pressure gradients.

Moreover, the rise in Mach number also enhances the rate at which vorticity changes due to molecular diffusion.

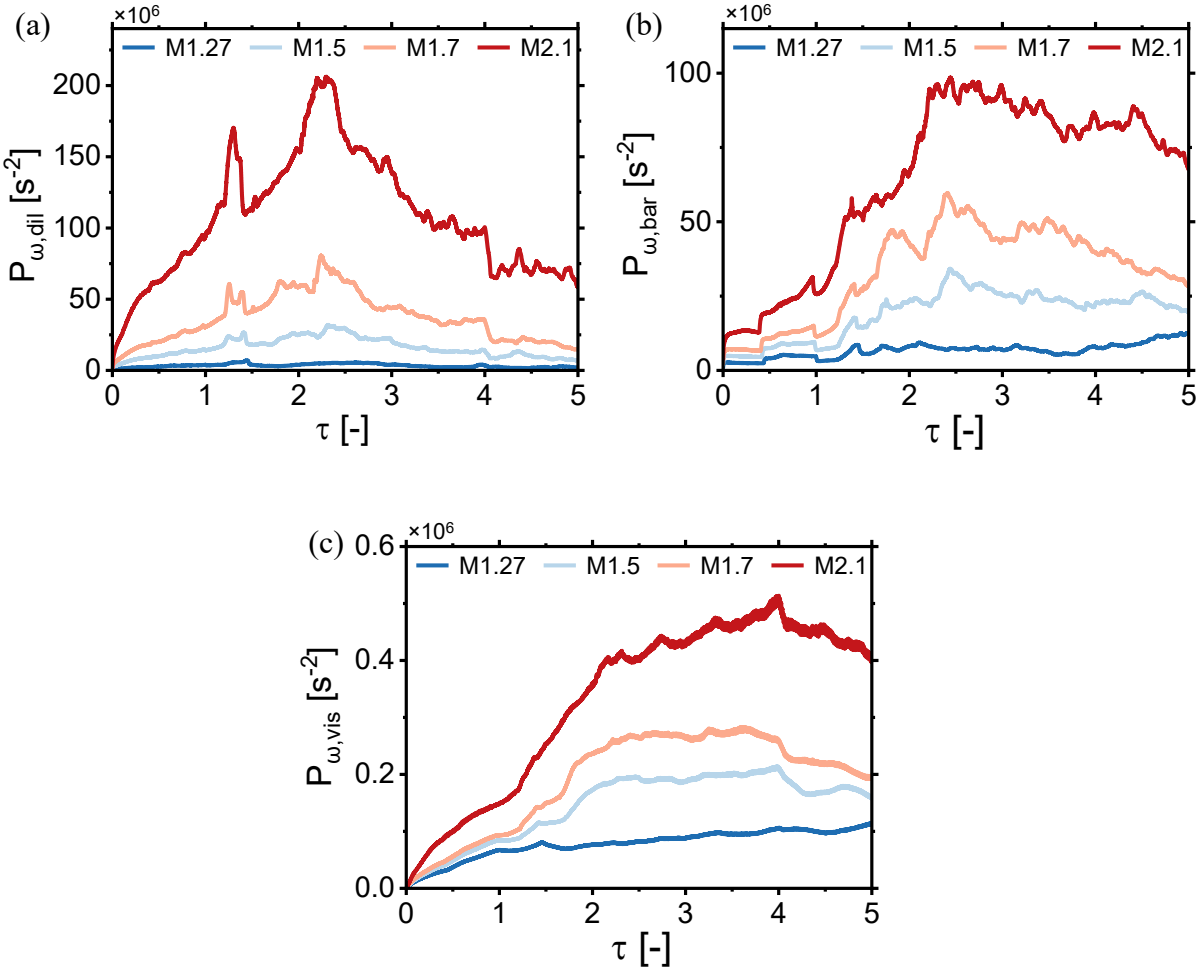

Figure 3-10. Spatially integrated fields of (a) dilatation term, (b) baroclinic term, and (c) viscosity term.

3.3.4.2. Circulation

The mixing of SF_6 and air caused by interface distortion is induced by deposited vorticity. Hence, it becomes essential to examine the vorticity deposited at the interface. In this section, we integrate the vorticity across the upper half of the double-layer gas cylinder to derive the temporal evolution of the circulation. The formula for the circulation (Γ) is given as follows:

$$\Gamma = \iint_A \omega(x,y)dxdy \qquad \textbf{(3-10)}$$

where A represents the area of the computational region in the upper half-plane, and ω signifies the vorticity at each grid point of the whole computational domain.

Figure 3-11 illustrates the positive, negative, and net components of the circulation histories in comparison with the numerical results from Feng et al. [43]. There is a notable increase in the magnitudes of both positive and negative circulation with the growth of the IS intensity. An increase in the Mach numbers intensifies the deposition of vorticity on both interfaces, which leads to the rapid evolution of vortex pairs. Notably, the magnitude of the positive circulation remains smaller than that of the negative circulation, and there is a peak of the net circulation around $\tau = 1.50$.

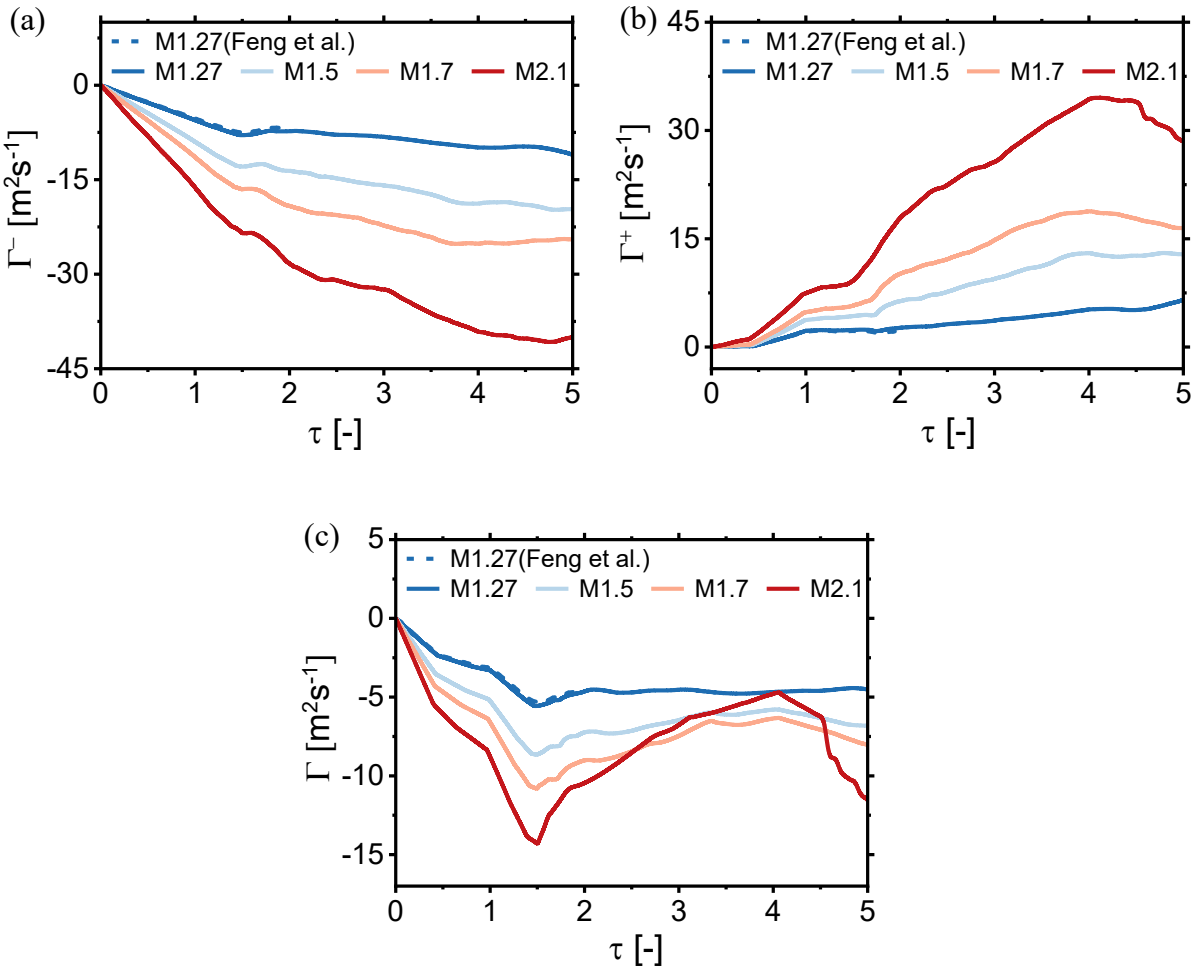

Figure 3-11. The (a) negative, (b) positive, and (c) net component of the circulation.

It is evident that both positive and negative components of the circulation exhibit a linear increase before $\tau = 1.50$. The negative circulation is mainly deposited at the outer cylinder, while the positive circulation is mainly deposited at the inner cylinder. The net circulation can be predicted by the linear summation of the positive circulation and negative circulation [42], [43]. The scenario of the IS passing over the outer cylinder can be regarded as a shock-heavy

bubble interaction. Hence, the negative circulation can be computed by the PB model [15] or the SZ model [43].

Another scenario of the TS_1 passing over the inner cylinder can be represented as the shock-light bubble interaction. Hence, the positive circulation can be calculated using the PB model or the YKZ model [16].

After linear summation of the PB model or SZ model for the outer cylinder and PB model or YKZ model for the inner cylinder, the comparison of net circulation between the numerical results and theoretical results is listed below in Table 3-7. The results indicate that the absolute value of the relative error obtained from the summation of the SZ model and PB model is under 2%, providing an accurate prediction of the net circulation. Moreover, it is observed that the summation of the PB model and PB model has a better prediction under the scenarios of higher Mach numbers.

Table 3-7. Comparison of circulation from the numerical simulation results (Γ_{sim}) and theoretical predictions by the summation of different models at τ = 1.32 (the unit of circulation is m^2/s).

Cases	Γ_{sim}	$\Gamma_{PB}+\Gamma_{PB}$	|error|	$\Gamma_{PB}+\Gamma_{YKZ}$	|error|	$\Gamma_{SZ}+\Gamma_{PB}$	|error|	$\Gamma_{SZ}+\Gamma_{YKZ}$	|error|
M=1.27	−5.03	−4.63	7.95%	−5.52	9.74%	−4.96	1.39%	−5.85	16.30%
M=1.5	−7.84	−7.40	5.61%	−9.33	19.01%	−7.81	0.38%	−9.74	24.23%
M=1.7	−9.80	−9.42	3.88%	−12.23	24.80%	−9.77	0.31%	−12.58	28.37%
M=2.1	−12.99	−12.88	0.85%	−17.37	33.72%	−12.90	0.69%	−17.40	33.95%

3.3.5. Mixing

To explore the impacts of the Mach number on the mixing of different gases, the mean mass fraction histories of SF_6 in the gas ring and its hypothetical gas SF_{6V} that retains identical physical properties in the inner cylinder are analyzed. The equation of the mean mass fraction is given below:

$$\bar{C} = \frac{\iint C\, dxdy}{\iint_B dxdy} \tag{3-11}$$

Figure 3-12 illustrates the mean mass fractions of both the outer and inner cylinders. Following the interaction with the incident shock wave, the mean mass fraction of SF_6 within the gas ring and SF_{6V} within the inner cylinder gradually decreases. This decline becomes more pronounced with increasing Mach number, indicating that stronger shocks enhance

mixing between the ambient air and SF_6. Therefore, higher Mach numbers promote material mixing in the double-layer gas cylinder.

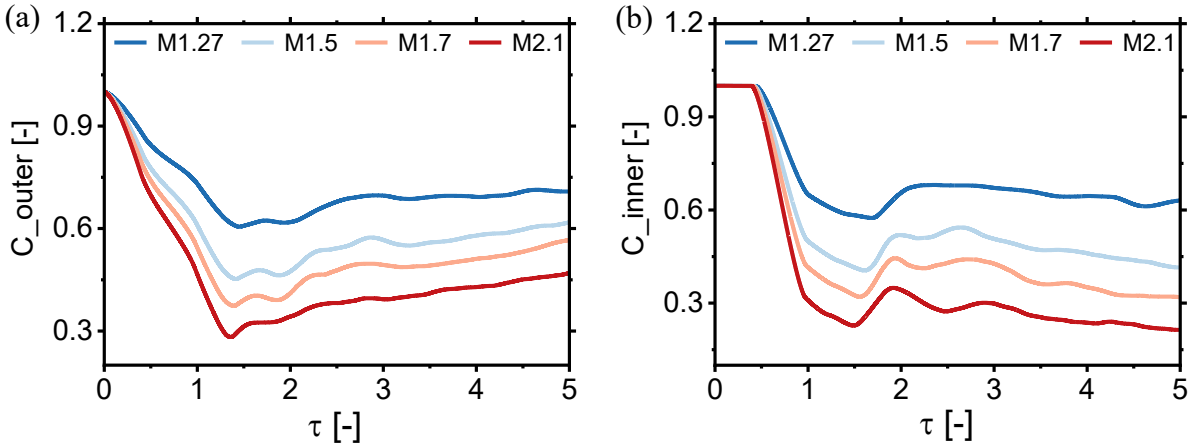

Figure 3-12. Mean mass fraction histories of the (a) outer cylinder and (b) inner cylinder.

3.4. Effects of Atwood number on ISBI scenarios

3.4.1. A-B-A type gas cylinder

3.4.1.1. Evolution of the double-layer gas cylinder

The numerical schlieren images of the double-layer gas cylinders accelerated by a planar shock for different Atwood numbers are given in Figure 3-13. We first examine the cases with $A_1 > 0$. The detailed morphologies of the double-layer gas cylinder in the scenario of $A_1 = 0.50$ have already been provided before. The TS_1 propagates in the gas ring at a slower pace than the IS outside the gas ring due to the mismatch in acoustic impedances across the interface, resulting in a convergent shape for the outer cylinder. With a decrease in the Atwood numbers, the acoustic impedance of the gases within the gas ring also decreases, resulting in a faster velocity of TS_1 in comparison to the case of $A_1 = 0.50$, enabling the TS_1 to reach the upstream pole of the inner cylinder more quickly. Moreover, the reduction in the velocity difference between TS_1 and TS_2 is particularly apparent for $A_1 = 0.39$, where the velocity of TS_1 and TS_2 exhibits only a slight difference, as illustrated in Figure 3-13. In addition, the amount of baroclinic vorticity deposited on the outer and inner interfaces diminishes with a decrease in the Atwood number, thereby suppressing RM instability and KH instability. This leads to a slower formation of primary and secondary vortex pairs and a reduced velocity of coupling with the primary vortex pair of the outer cylinder.

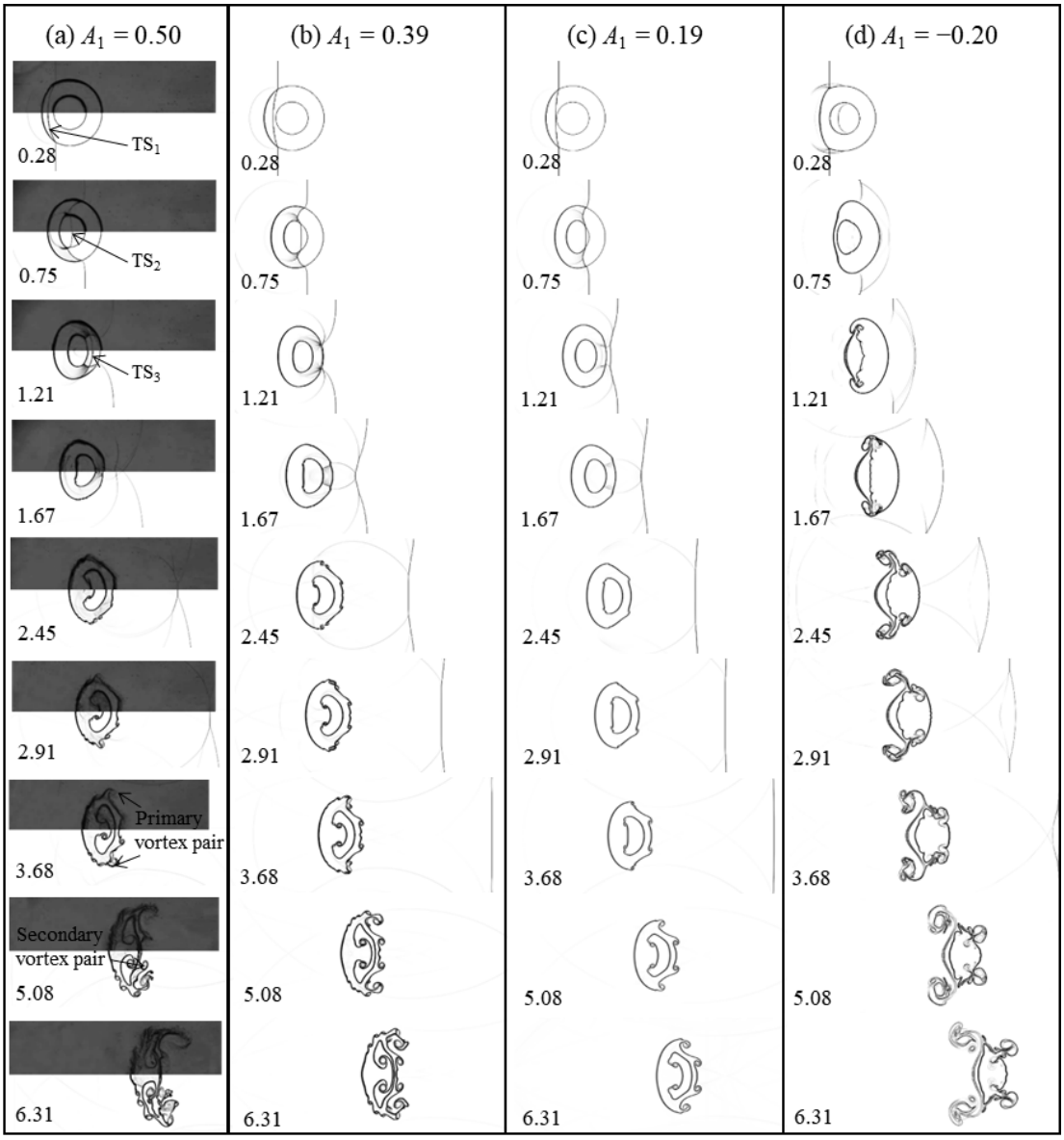

Figure 3-13. Numerical schlieren images of the double-layer gas cylinders for different Atwood numbers in A-B-A type gas cylinder.

In the scenario of $A_1 < 0$ depicted in Figure 3-14, an RRW emerges upon the collision of IS with UI_1. Within the gas ring, the TS_1 propagates faster than the IS due to the lower acoustic impedance of the gas compared to the surrounding air, which results in TS_1 taking on a divergent shape (τ = 0.04). Upon reaching UI_2, TS_1 transitions into TS_2, taking on a convergent form. At this moment, an RS generates and moves upstream. As the RS touches the UI_1, it transmits into the TRS (τ = 0.27). The convergence of the TS_2, the DTS_2, and its symmetric counterpart causes the formation of two high-pressure zones (hpz) whose trajectories are marked by the slip lines (sl) (τ = 0.51). As TS_2 passes the intersection point of DTS_2 and its counterpart, a significantly higher-pressure zone forms upstream of TS_2 (τ = 0.58). Subsequently, as TS_2 traverses the DI_2, a bulge emerges downstream. Throughout this

evolution, the distance between UI_1 and UI_2 diminishes while the distance between DI_1 and DI_2 widens. In the upstream interface, it becomes apparent that ambient air converges with air from the upper and lower poles of the inner cylinder, entering the He ring and generating two jets in a spanwise direction (τ = 1.05). These jets collide with the upper and lower interfaces of the inner cylinder, resulting in the generation of a vortex pair moving upstream. In addition, protrusions of the ambient air into the He ring promote the development of a vortex pair moving downstream from the DI_1 (τ = 4.94).

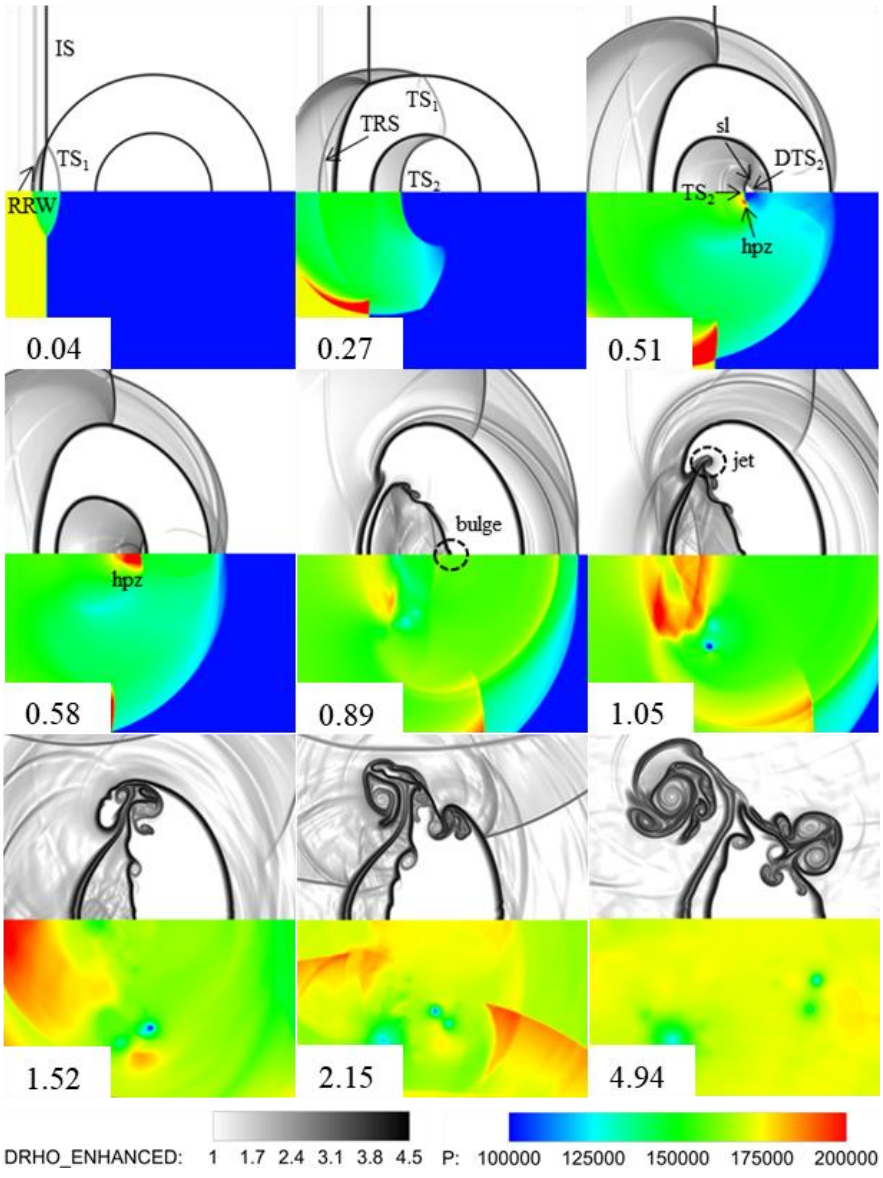

Figure 3-14. Time sequences of numerical schlieren images and pressure contours for A_1 = −0.20. RRW, reflected rarefaction wave; TRS, transmitted reflected shock wave; DTS_2, the second diffracted transmitted shock wave; sl, slip line; hpz, high-pressure zone.

3.4.1.2. Widths and heights

To quantify this process of evolution at various Atwood numbers, the normalized widths and heights of the outer and inner gas cylinders are analyzed, as shown in Figure 3-15. At the early stage (τ = 0−1.22), the widths of the outer gas cylinder decrease rapidly after being compressed by the IS. As the Atwood number increases, the compression of the UI_1 by the IS becomes less pronounced. For cases with $A_1 > 0$, the rise in acoustic impedance of the gas mixture within the ring reduces the propagation velocity of the transmitted shock across the DI_1, thereby exerting a smaller downstream acceleration on DI_1 and resulting in a narrower width for higher Atwood number cases. Moreover, a higher Atwood number enhances the density gradient, leading to increased deposition of baroclinic vorticity on DI_1. This promotes the faster formation and evolution of vortex pairs, which slows down the reduction in width. In contrast, for cases with small absolute values of the Atwood number, the RM instability is effectively suppressed, and the width remains nearly constant after $\tau > 2.76$.

Initially, the height of the outer gas cylinder remains almost unchanged during the interaction of the IS with the double-layer gas cylinder. However, after the shock wave passes through the diametral plane of the interface, it transforms into a diffracted shock wave, which compresses the gas cylinder in the spanwise direction, reducing its height. With the increasing Atwood number, the compression of the gas cylinder on height becomes more significant. As the primary vortex pairs develop, the height of the outer cylinder increases significantly, with the height of $A_1 = 0.50$ exceeding that of $A_1 = 0.39$ and $A_1 = 0.19$ after $\tau = 2.6$. In the case of $A_1 < 0$, the change in widths of $A_1 = -0.20$ is similar to that of the other cases, while its heights increase after the IS passes through the diametral plane of the interface. As the primary vortex pair develops, the height of the gas cylinder continues to increase, keeping larger than the other cases. In summary, when $A_1 > 0$, the reduction in the Atwood number effectively suppresses the evolution of the outer cylinder in width at the early stage. However, the width and height remain relatively steady as evolution progresses.

The widths and heights of the inner cylinder influenced by Atwood numbers in the scenario of $A_1 > 0$ are shown in Figure 3-16. The sign of Atwood numbers for the second layer is opposite to that of A_1. In the initial phase, the widths of the inner cylinder rapidly decrease due to the compression of the TS_1. The rate of reduction slows down as the Atwood number decreases. Following the phase of compression, the development of the DI_2 and the evolution of vortex pairs cause an increase in the width of the gas cylinder.

The compression of the inner cylinder in the flow direction by the shock wave promotes its spanwise development at the early stage of evolution. Moreover, the height of the inner

cylinder grows more rapidly with an increase in the Atwood number (τ' = 0−0.51). Consequently, the height of the inner cylinder decreases due to the TS_1 passing through its diametral plane. At the later stage of evolution, the increase in the Atwood number enhances the coupling speed of the vortex pair of the inner cylinder and the primary vortex pair of the outer cylinder, promoting the gradual merging of its upstream interface and downstream interface of the outer cylinder. In the scenario of $A_1 < 0$, the inner gas cylinder merges with the outer cylinder at the early stage of evolution, making it challenging to distinguish its height. Therefore, the discussion in this section does not concern the height and width of A_1 = −0.20.

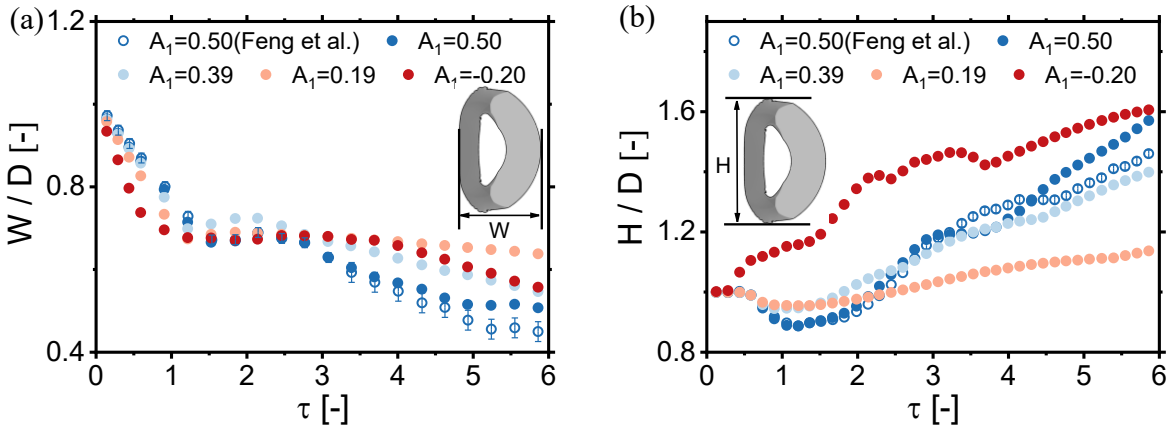

Figure 3-15. Variation of (a) widths and (b) heights of the outer cylinder.

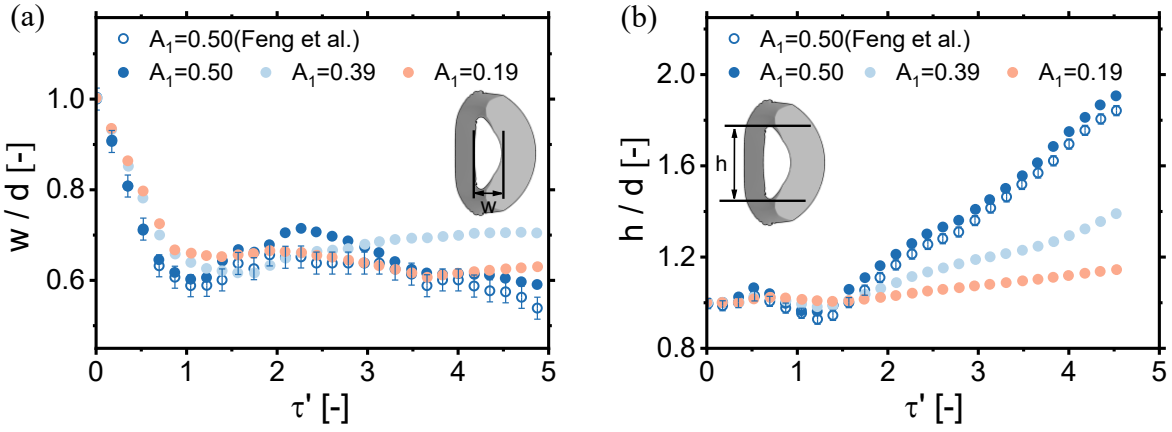

Figure 3-16. Variation of (a) widths and (b) heights of the inner cylinder.

3.4.1.3. Vorticity generation

3.4.1.3.1. Dynamics of vorticity production

Figure 3-17 illustrates the impact of the Atwood number on the vorticity distribution at various time sequences. For the scenarios where the initial densities of SF_6, Kr and CO_2 are 6.14 kg/m^3, 3.49 kg/m^3 and 1.83 kg/m^3, respectively. UI_1 corresponds to a light/heavy interface where $\nabla\rho$ directs inwards radially, while UI_2 corresponds to a heavy/light interface where $\nabla\rho$ directs outwards radially. Since ∇p opposes the shock propagation direction, negative vorticity is deposited at the outer interface, while positive vorticity is deposited at the inner interface. In contrast, for the scenarios where the initial density of He is 0.17 kg/m^3, UI_1 corresponds to a heavy/light interface, while UI_2 corresponds to a light/heavy interface. In this case, positive vorticity is deposited at the outer interface, while negative vorticity is deposited at the inner interface. As the magnitude of the Atwood number increases, more vorticity is deposited at both outer and inner interfaces, causing the rolled-up vortices to become more pronounced.

As illustrated in Figure 3-18, the absolute values of the dilatational and baroclinic terms surpass that of the viscous term, indicating their dominance in vorticity production during the evolution. For the scenarios of $A_1 > 0$, the increase in the Atwood number contributes to the growth of the dilatation term, indicating that higher Atwood numbers result in stronger compression effects. The first peak values appear due to the generation of vortex pairs and stretched structures around the vortex core. During the stage when IS passes through the gas ring, higher acoustic numbers enhance the density gradient, which in turn amplifies the baroclinic term due to the larger misalignment between the density and pressure gradients. As time progresses, the values in baroclinic terms remain elevated due to the sustained influence of the reflected shock waves. In addition, the higher Atwood numbers also intensify the viscosity term.

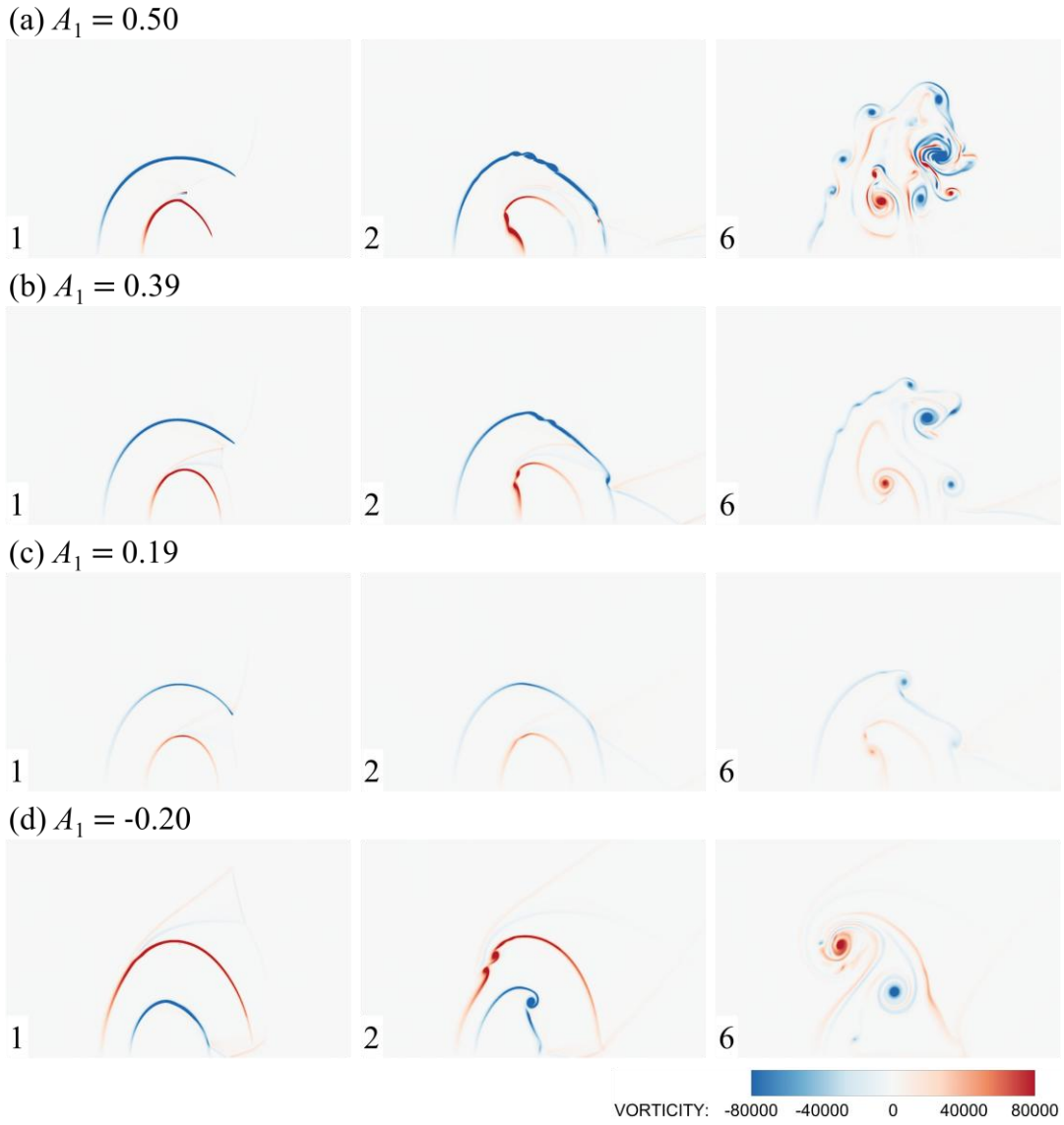

Figure 3-17. Time sequences of vorticity distribution for different Atwood numbers in A-B-A type gas cylinder.

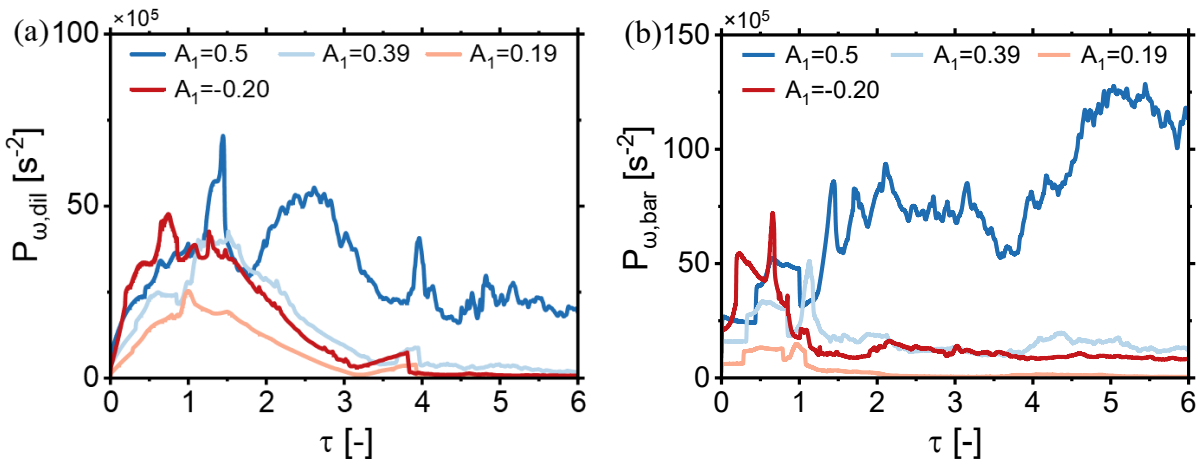

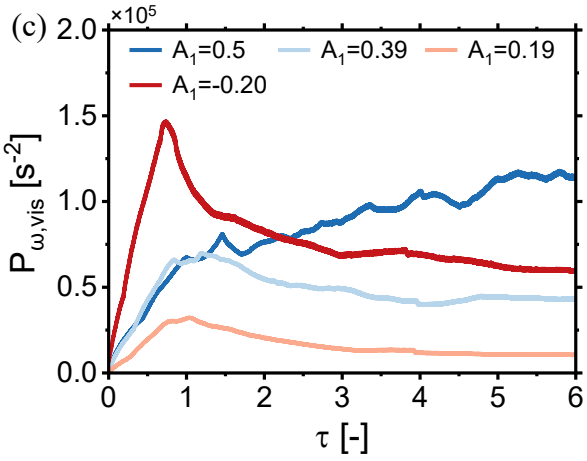

Figure 3-18. Spatially integrated fields of (a) dilatation term, (b) baroclinic term, and (c) viscosity term.

3.4.1.3.2. Circulation

In the context of the mixing of SF_6 and air, interface distortion induced by deposited vorticity plays a crucial role, making it necessary to analyze the circulation on the interface. Figure 3-19 compares the positive, negative, and net components of circulation with the numerical findings from Feng et al. [43]. In the case of $A_1 > 0$, the decrease in the Atwood number leads to a substantial reduction in the magnitudes of both positive and negative circulation. As positive vorticity is primarily observed at the inner interface and negative vorticity is concentrated at the outer interface, the decrease in the Atwood number reduces the deposition of vorticity on both interfaces, suppresses the development of vortex pairs and decelerates the mixing of different gases. Notably, the magnitudes of positive circulation consistently remain smaller than those of negative circulation, resulting in a peak of net circulation around τ = 1.50. Conversely, when $A_1 < 0$, the magnitudes of both positive and negative circulation increase significantly, accelerating the mixing rate.

The net circulation at positive Atwood number conditions is predicted by the linear summation of the PB model or SZ model for the outer cylinder and the PB model or YKZ model for the inner cylinder. Upon comparing numerical results with theoretical predictions outlined in Table 3-8. Comparison of circulation from the numerical simulation results (Γ_{sim}) and theoretical predictions by the summation of different models at τ = 1.32 (the unit of circulation is m^2/s)., it is evident that the absolute value of the relative error obtained from the summation of SZ model and PB model remains under 3%, having a better prediction of net circulation.

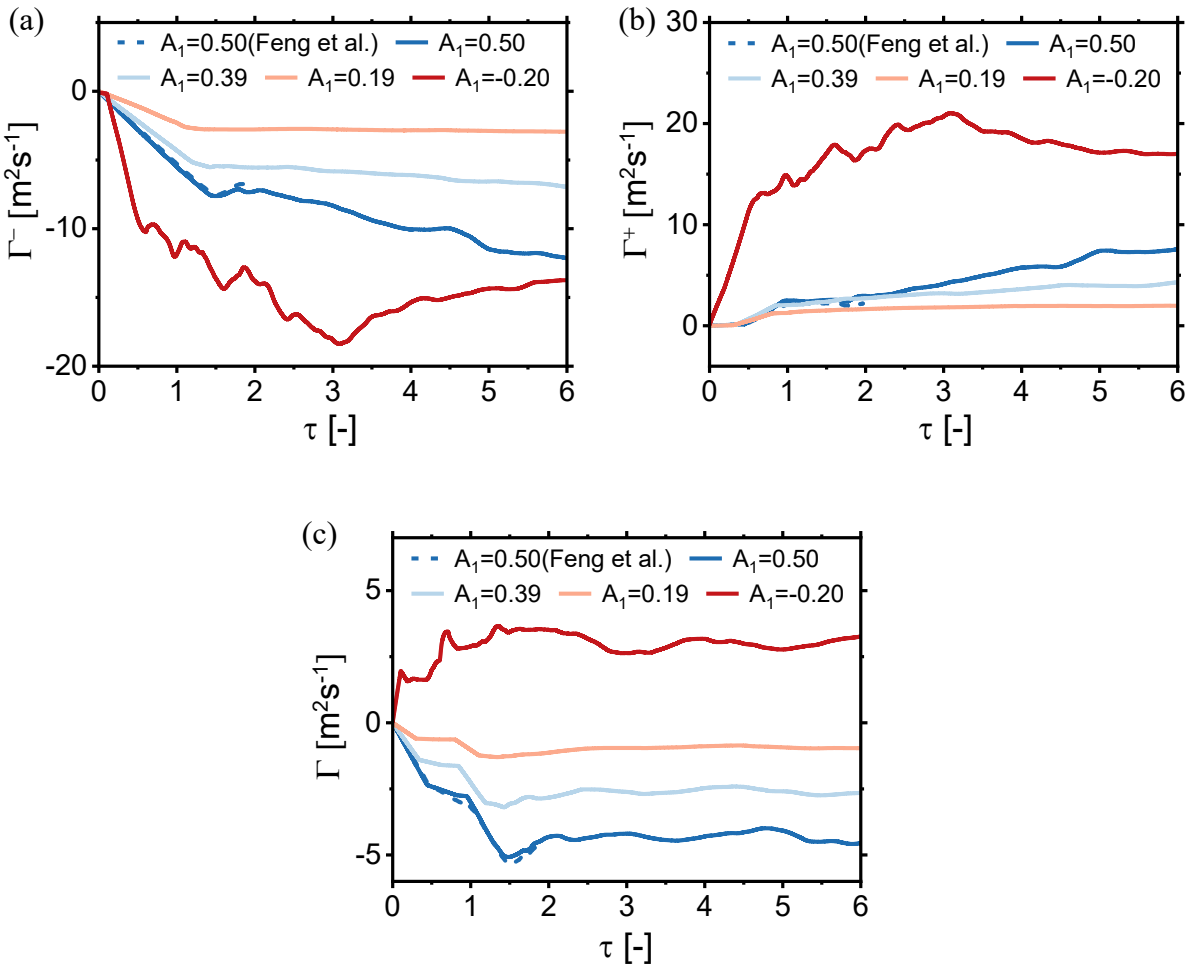

Figure 3-19. The (a) negative, (b) positive, and (c) net component of the circulation.

Table 3-8. Comparison of circulation from the numerical simulation results (Γ_{sim}) and theoretical predictions by the summation of different models at τ = 1.32 (the unit of circulation is m²/s).

Cases	Γ_{sim}	$\Gamma_{PB}+\Gamma_{PB}$	|error|	$\Gamma_{PB}+\Gamma_{YKZ}$	|error|	$\Gamma_{SZ}+\Gamma_{PB}$	|error|	$\Gamma_{SZ}+\Gamma_{YKZ}$	|error|
A_1=0.50	−5.03	−4.63	7.95%	−5.52	9.74%	−4.96	1.39%	−5.85	16.30%
A_1=0.39	−2.94	−2.63	10.5%	−2.85	3.06%	−2.92	0.68%	−3.15	7.14%
A_1=0.19	−1.17	−0.83	29.06%	−0.92	21.37%	−1.20	2.56%	−1.28	9.40%

3.4.1.4. Mixing

To explore the impacts of the Atwood number on the mixing of different gases, the mean mass fraction histories of both outer gas ring and inner cylinder are analyzed.

Figure 3-20 illustrates the mean mass fraction of SF_6 in the gas ring and SF_{6V} in the inner cylinder. During the passage of the incident shock over the outer interface, the mean mass fraction of SF_6 within the gas ring exhibits a decline, accompanied by a slight increase at the later stage of evolution. As the Atwood number increases, the mean mass fraction of SF_{6V} in the inner gas cylinder significantly decreases, which promotes the mixing within the inner interface.

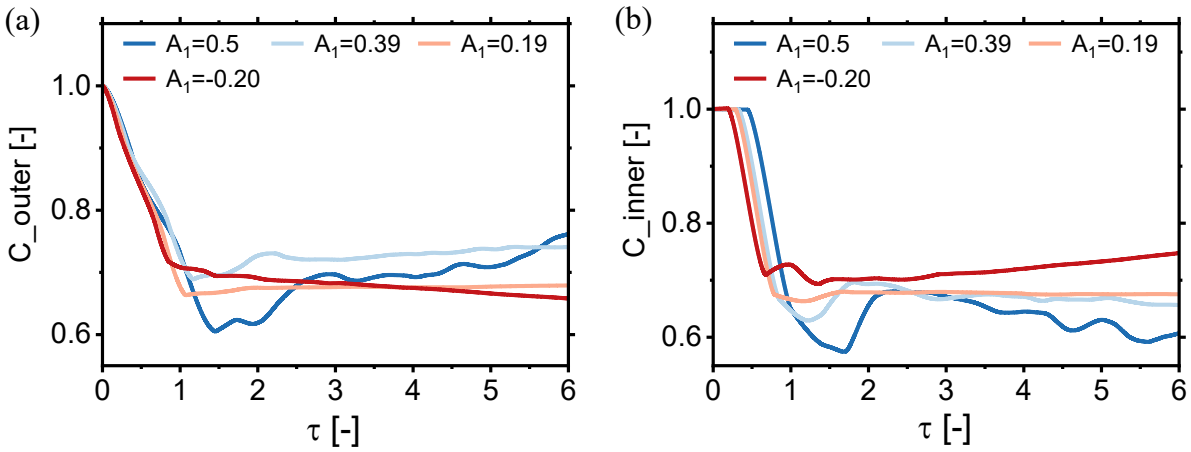

Figure 3-20. Mean mass fraction histories of the (a) outer cylinder and (b) inner cylinder.

3.4.2. A-B-C type gas cylinder

3.4.2.1. Evolution of the double-layer gas cylinder

Figure 3-21 displays numerical schlieren images at various Atwood numbers. Upon the impact of the IS on the UI_1, it transforms into the TS_1. The gas composition within the gas ring is consistent in various scenarios, resulting in a constant velocity for TS_1 (τ = 0.28), which suggests that the moment when TS_1 impinges on the UI_2 keeps the same at different scenarios. Following the passage of TS_1 over UI_2, it turns to the TS_2. As the concentrations of SF_6 in the inner cylinder increase, the acoustic impedance rises, thereby suppressing the propagation velocity of TS_2 in the inner cylinder (τ = 0.75). The transition in the morphology of TS_2 from divergence to convergence can also be observed, which induces diverse interface morphologies downstream of DI_1. The secondary vortex pair emerges at the DI_1 for $A_2 < 0$. The distance between the second vortex pairs decreases with increasing Atwood number. Due to the small distance between the vortex pair, they rapidly merge and form a jet at the later stage of evolution. When $A_2 > 0$, a jet is formed at the DI_1 ($\tau > 2.45$). In the scenario of a single-layer gas cylinder, a downstream jet propagates from the downstream interface due to shock focusing [25]. However, the wave patterns are complex due to the existence of an inner

cylinder compared to the single-layer gas cylinder, further investigation is needed to understand the mechanisms behind the generation of secondary vortex pairs and downstream jets of the double-layer gas cylinder.

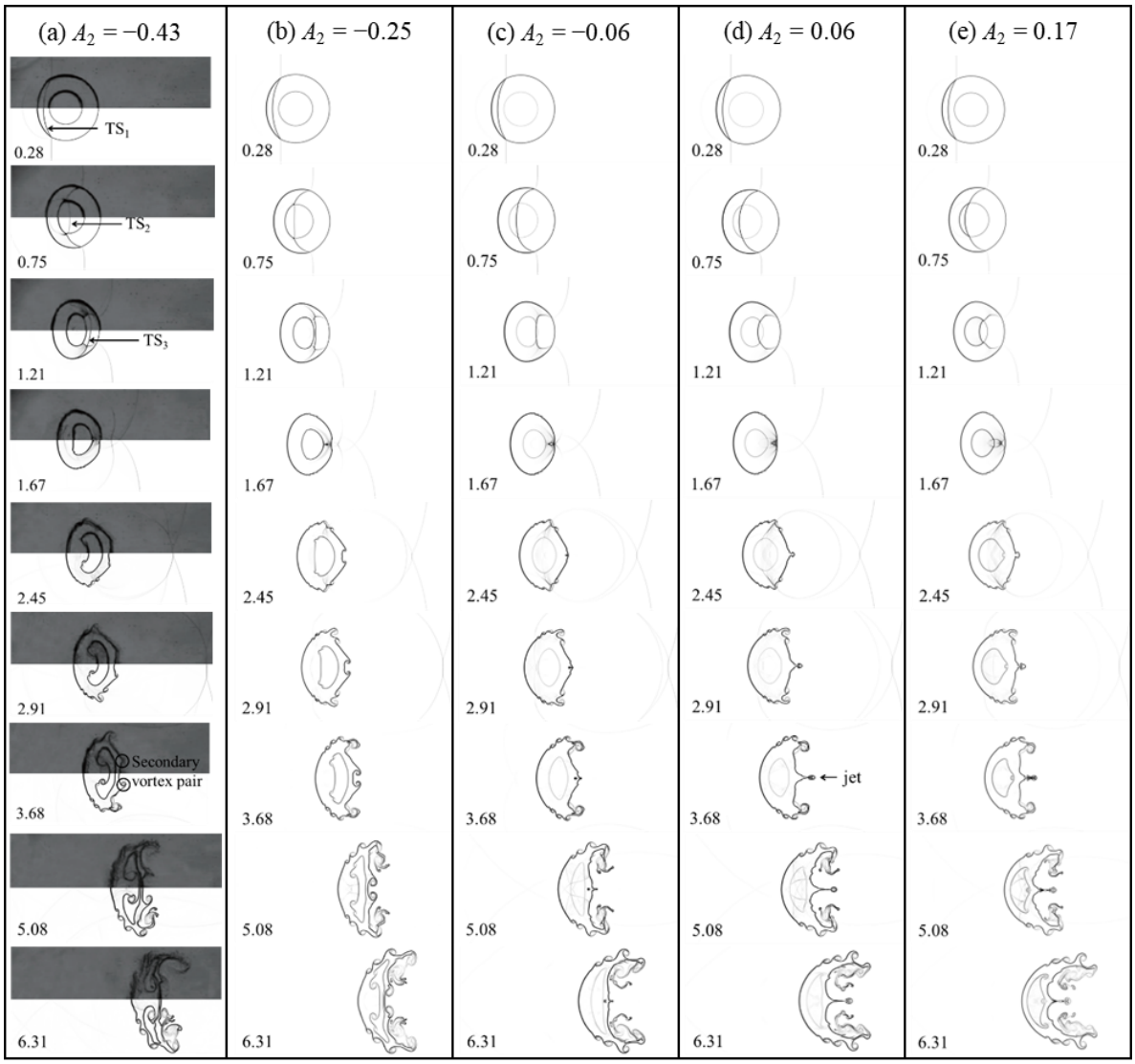

Figure 3-21. Numerical schlieren images of the double-layer gas cylinders for different Atwood numbers in A-B-C type gas cylinder.

3.4.2.2. Formation of the secondary vortex pair and jet

Due to the sign of the Atwood number for the inner layer having an impact on the morphologies of the DI_1, the mechanisms behind the formation of secondary vortex pairs and jets at DI_1 are discussed in this section to investigate the dependence of the flow morphologies on Atwood numbers.

For the scenarios of $A_2 < 0$ (see Figure 3-22, Figure 3-23, and Figure 3-24), the sweeping of a diffracted shock contributes to the formation of an internal DTS inside the bubble. Upon

TS_2 passing over the DI_2, it turns into the TS_3. The shock k, the TS_3, the DTS, and the RS are connected by a Mach stem. As time progresses, these four shock waves intersect at one point. Subsequently, TS_3 separates from the other three shock waves, generating a new TP. It is noteworthy that the position at which the triple points collide with the downstream interface coincides with the position of the vortex pair formation. Due to the interaction of shock waves, a high-pressure zone is formed downstream of the TP. As the triple points pass through DI_1, the increase in pressure gradient and the change in density gradient lead to the generation of baroclinic vorticity, thereby inducing the formation of secondary vortex pairs.

As depicted in Figure 3-22, Figure 3-23, and Figure 3-24, the morphological transition of TS_2 shifts from divergence to convergence with increasing concentrations of SF_6 in the inner cylinder. The morphology of TS_2 is divergent for $A_2 = -0.43$, while the TS_2 tends to converge for $A_2 = -0.06$. Therefore, when TS_2 passes through DI_2, the distance between the Mach stem and the symmetry axis decreases, and the length of the Mach stem increases. With an increase in the Atwood number, the intersection point of the shock k, TS_3, DTS, and RS moves closer to the symmetry axis. Following the separation of TS_3 from this point, the distance between the resulting triple points decreases. As the interaction between the triple points and DI_1 induces the formation of secondary vortex pairs, an increase in the Atwood number leads to a reduction in the distance between secondary vortex pairs.

Figure 3-25 and Figure 3-26 reveal the scenarios of $A_2 > 0$, where TS_2 exhibits a convergent morphology. The TS_3, DTS, and RS meet at one point after TS_2 impinges on the DI_2, and TS_3 does not separate from this point. The convergence of TS_3, DTS, and its symmetric counterpart results in the formation of two high-pressure zones. After TS_3 passes through the intersection point of DTS and its symmetric counterpart, a significantly higher-pressure zone is generated downstream of TS_3. As TS_3 continues to move and impinge on the downstream interface, it gives rise to the formation of a bulge, followed by the generation of a jet.

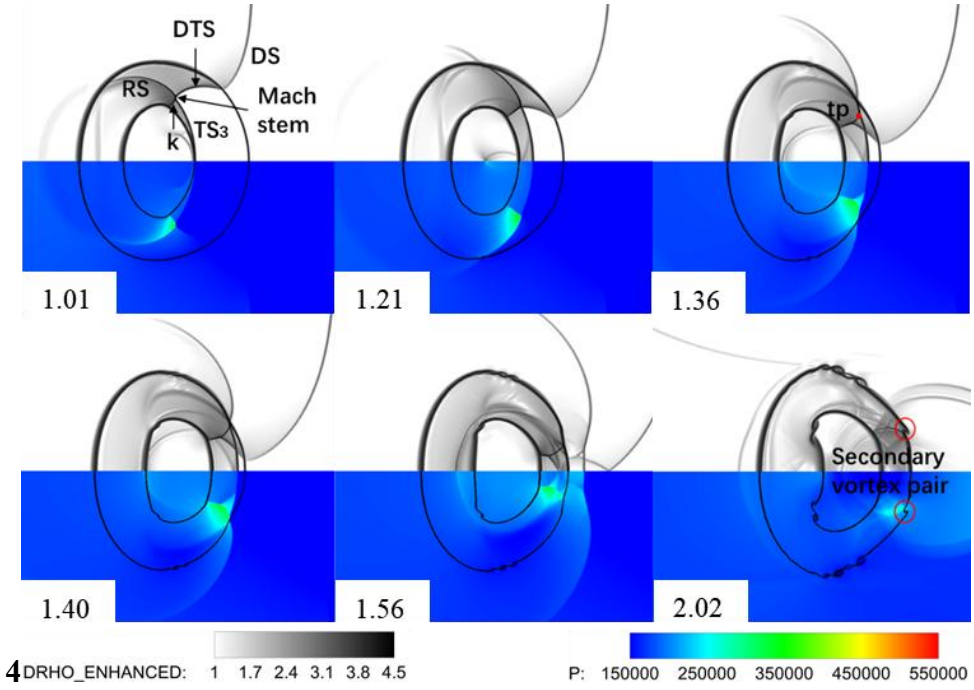

Figure 3-22. Time sequences of numerical schlieren images and pressure contours for A_2 = –0.43. DS, diffracted shock wave; DTS, diffracted transmitted shock wave; RS, reflected shock wave; TS_3, the third transmitted shock wave; K, a shock wave; TP, triple point.

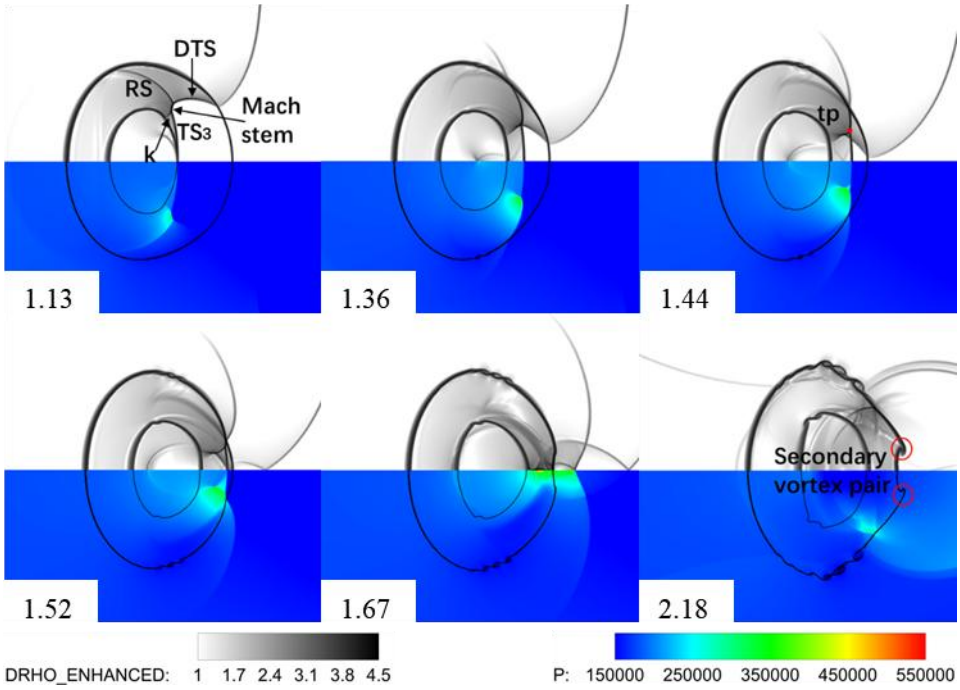

Figure 3-23. Time sequences of numerical schlieren images and pressure contours for A_2 = –0.25.

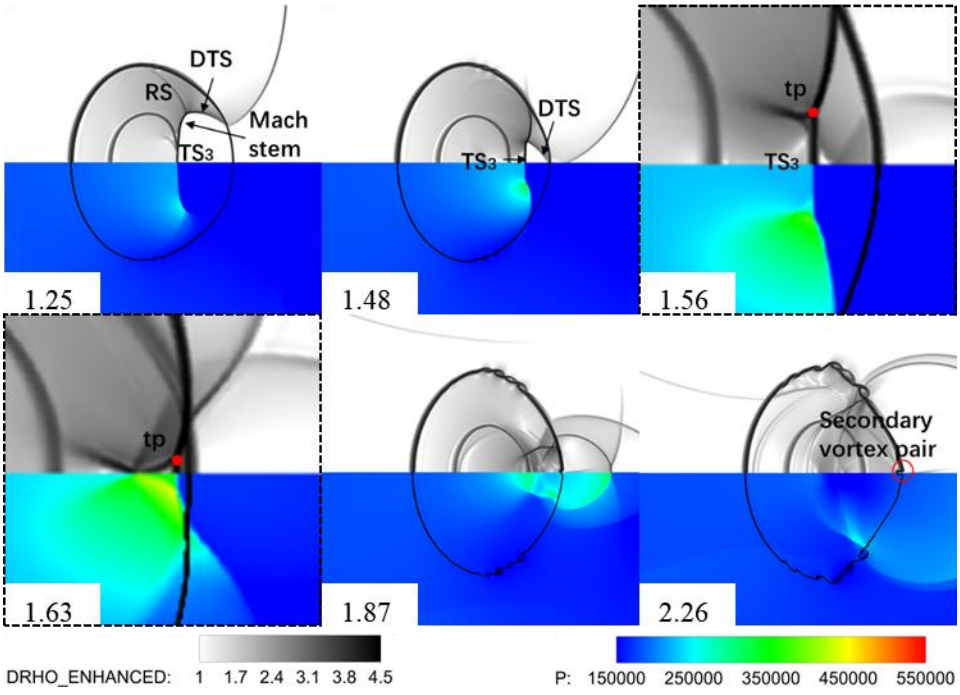

Figure 3-24. Time sequences of numerical schlieren images and pressure contours for $A_2 = -0.06$.

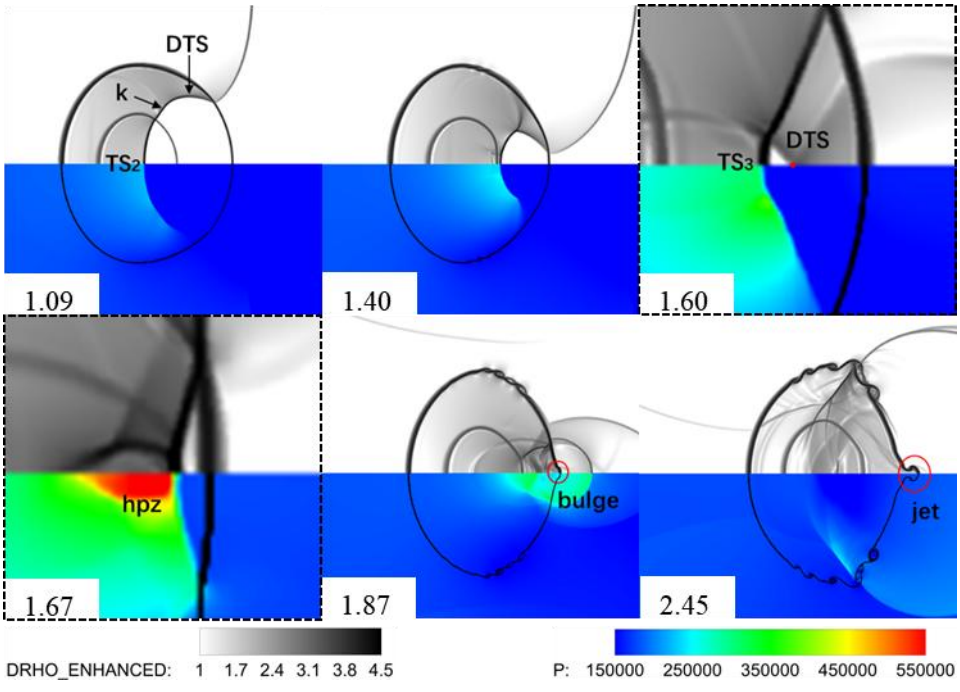

Figure 3-25. Time sequences of numerical schlieren images and pressure contours for $A_2 = 0.06$.

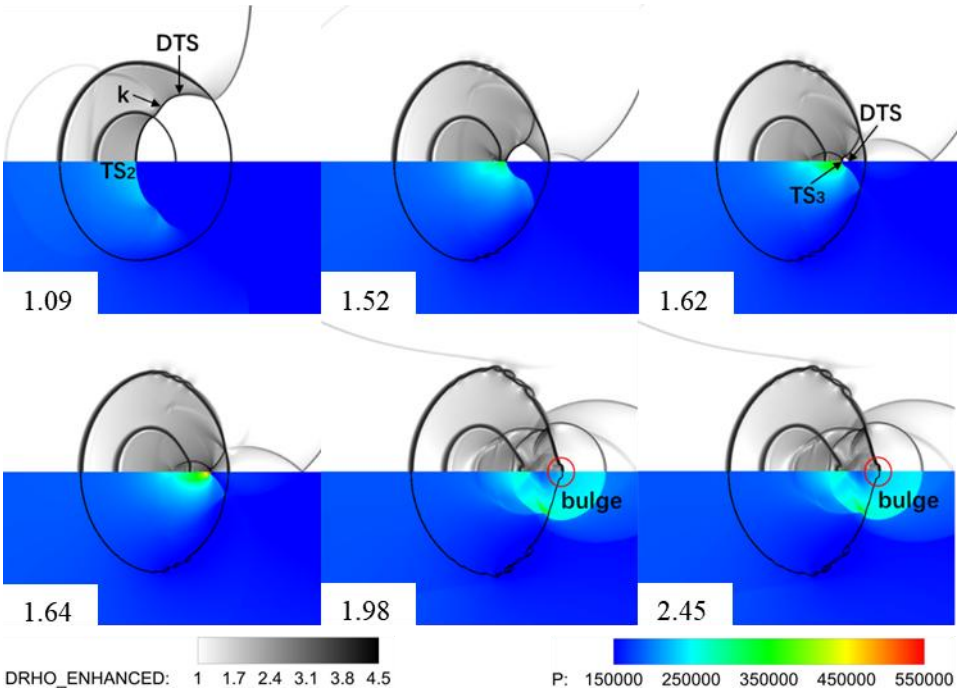

Figure 3-26. Time sequences of numerical schlieren images and pressure contours for $A_2 = 0.17$.

3.4.2.3. Widths and heights

The normalized widths and heights of both outer and inner cylinders are investigated to quantitatively analyze the evolution process. For the outer cylinder, the compression effect of the IS on the UI_1 leads to a reduction in widths at the early stage of evolution, as shown in Figure 3-27(a). Since gas composition within the gas ring remains constant and the change in the gas composition of the inner cylinder has minimal impact on the morphologies of the outer interface before the passage of the IS, the widths and heights of various cases remain essentially unchanged (τ = 0–1.22). As the Atwood number increases, the morphologies of the UI_2 transition from secondary vortex pairs to jets, leading to an increase in widths. As the concentration of SF_6 in the inner cylinder increases, the acoustic impedance increases, which slows down the propagation speed of the transmitted shock wave within the inner cylinder for the scenarios of $A_2 > 0$. Consequently, the high-pressure zone associated with the TS_3 for A_2 = 0.17 reaches the DI_1 later than that for A_2 = 0.06, the formation of the bulge and the jet is delayed (see Figure 3-25 and Figure 3-26), leading to a smaller width for A_2 = 0.17 compared to that for A_2 = 0.06. As depicted in Figure 3-27(b), the heights of the outer cylinder remain unchanged during the early phase of the evolution (τ = 0–0.7). After the IS passes through the diametral plane of the outer cylinder, a DS is generated, resulting in compression of the heights (τ = 0–1.22). A large amount of baroclinic vorticity is deposited near the diametral

plane of the outer interface, generating the primary vortex pair, which promotes the increase in heights. As the Atwood number increases, the morphologies of the inner cylinder noticeably transition from divergence to convergence, leading to a reduction in the growth rate of heights.

Figure 3-28 reveals the variation of the widths and heights of the inner cylinder. During the initial phase (τ' = 0–1.05), the widths of the inner cylinder undergo a rapid decline due to the impact of the TS_1 with the Atwood number decreasing. Following the phase of compression, the development of vortex pairs and movement downstream of the DI_2 amplify the width. Under the compression of UI_1, the width subsequently decreases. Due to the suppression of RM instability at lower magnitudes of the Atwood number, the width remains smaller compared to other scenarios.

After the compression of the inner cylinder in the flow direction by the shock wave promotes its spanwise development at the early stage of evolution, the height of the inner cylinder subsequently decreases due to the TS_1 passing through its diametral plane. With increasing Atwood number, the morphology of the inner cylinder shifts from divergent to convergent, leading to a more significant reduction in height.

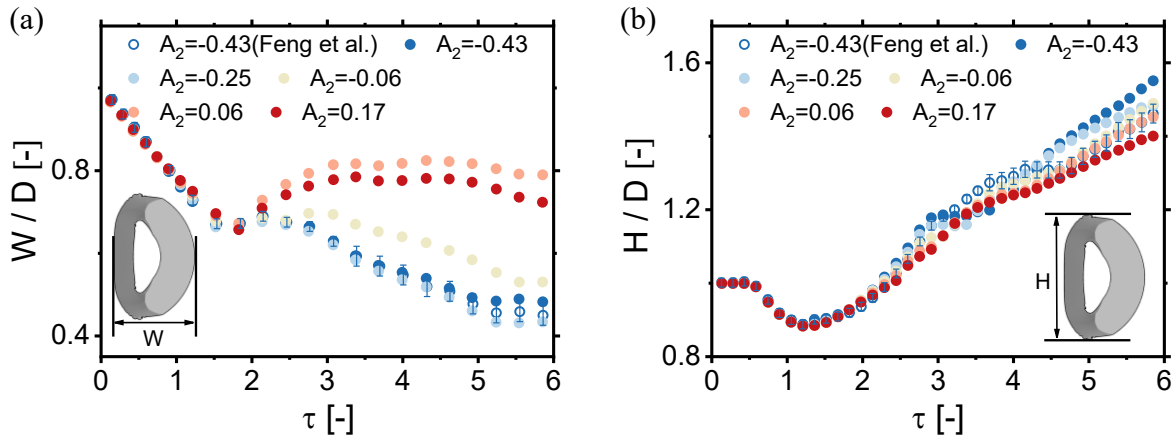

Figure 3-27. Variation of (a) widths and (b) heights of the outer cylinder.

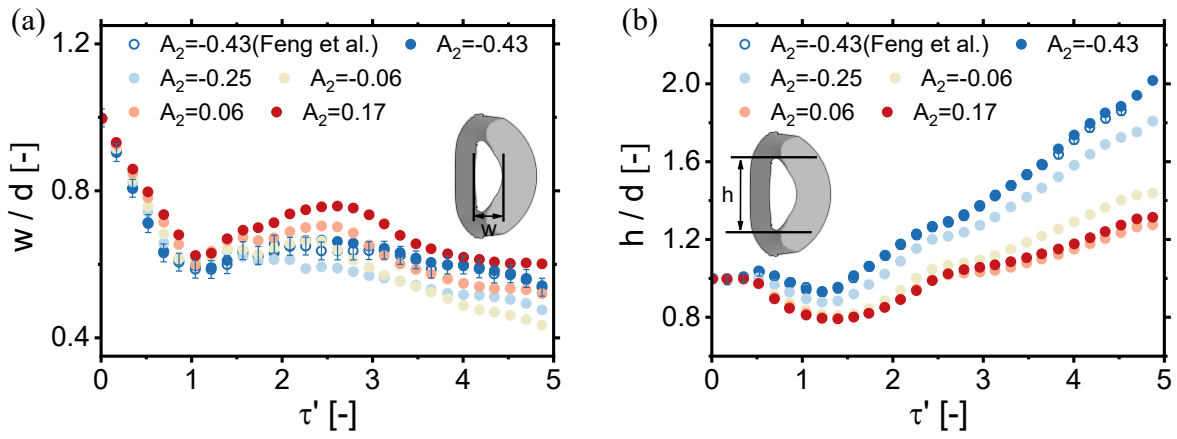

Figure 3-28. Variation of (a) widths and (b) heights of the inner cylinder.

3.4.2.4. Vorticity generation

3.4.2.4.1. Dynamics of vorticity production

Figure 3-29 illustrates the impact of the Atwood number on the vorticity distribution at various time sequences. For the first layer with positive Atwood numbers, UI_1 corresponds to a light/heavy interface where negative vorticity is deposited at the outer interface. In contrast, for the second layer with negative Atwood numbers, UI_2 corresponds to a heavy/light interface where positive vorticity is deposited at the inner interface. For the second layer with positive Atwood numbers, UI_2 corresponds to a light/heavy interface where negative vorticity is deposited at the inner interface. As the magnitude of the Atwood number increases for the second layer, more vorticity is deposited at the inner interface, causing the rolled-up vortices to become more pronounced. With the growth of the Atwood number, the morphologies of the DI_1 transition from the secondary vortex pair to the downstream jet with positive vorticity.

As illustrated in Figure 3-30, the absolute values of the dilatational and baroclinic terms surpass that of the viscous term, indicating their dominance in vorticity production during the evolution. Following the passage of the IS over the UI_2 ($0.43 < \tau < 1.10$), the value of $A_2 > 0$ in the dilatation term is greater than other cases, implying that the large absolute values of the Atwood numbers result in stronger compression effects, especially for the compression stage of the IS acting on the UI_1. Moreover, the absolute values of the Atwood numbers increase contributes to the growth of the density gradient, which leads to an increase in the baroclinic term due to the misalignment of the density and pressure gradients. For the scenarios of negative Atwood numbers, the first peak values occur after the TP impinges on the DI_1. The generation of the secondary vortex pairs and the presence of the stretched structures around the vortex core result in relatively large peak values of $A_2 = -0.43$ and $A_2 = -0.25$ in the

dilatation term. For the scenarios of $A_2 > 0$, the first peak values occur after the TS_3 with a much higher-pressure zone passing over the DI_1. As time progresses, the values in the baroclinic term remain elevated under the impact of the reflected shock structures.

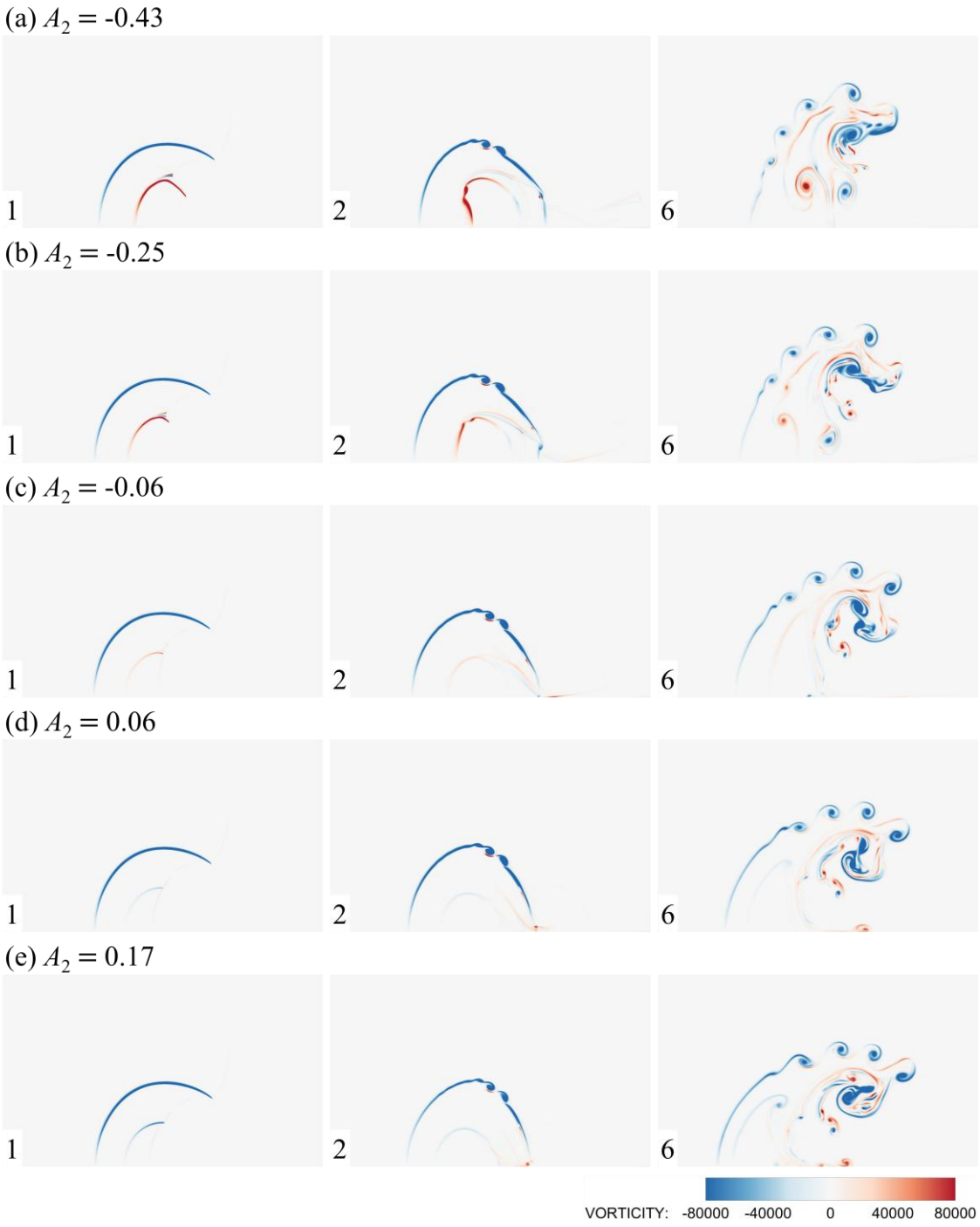

Figure 3-29. Time sequences of vorticity distribution for different Atwood numbers in A-B-C type gas cylinder.

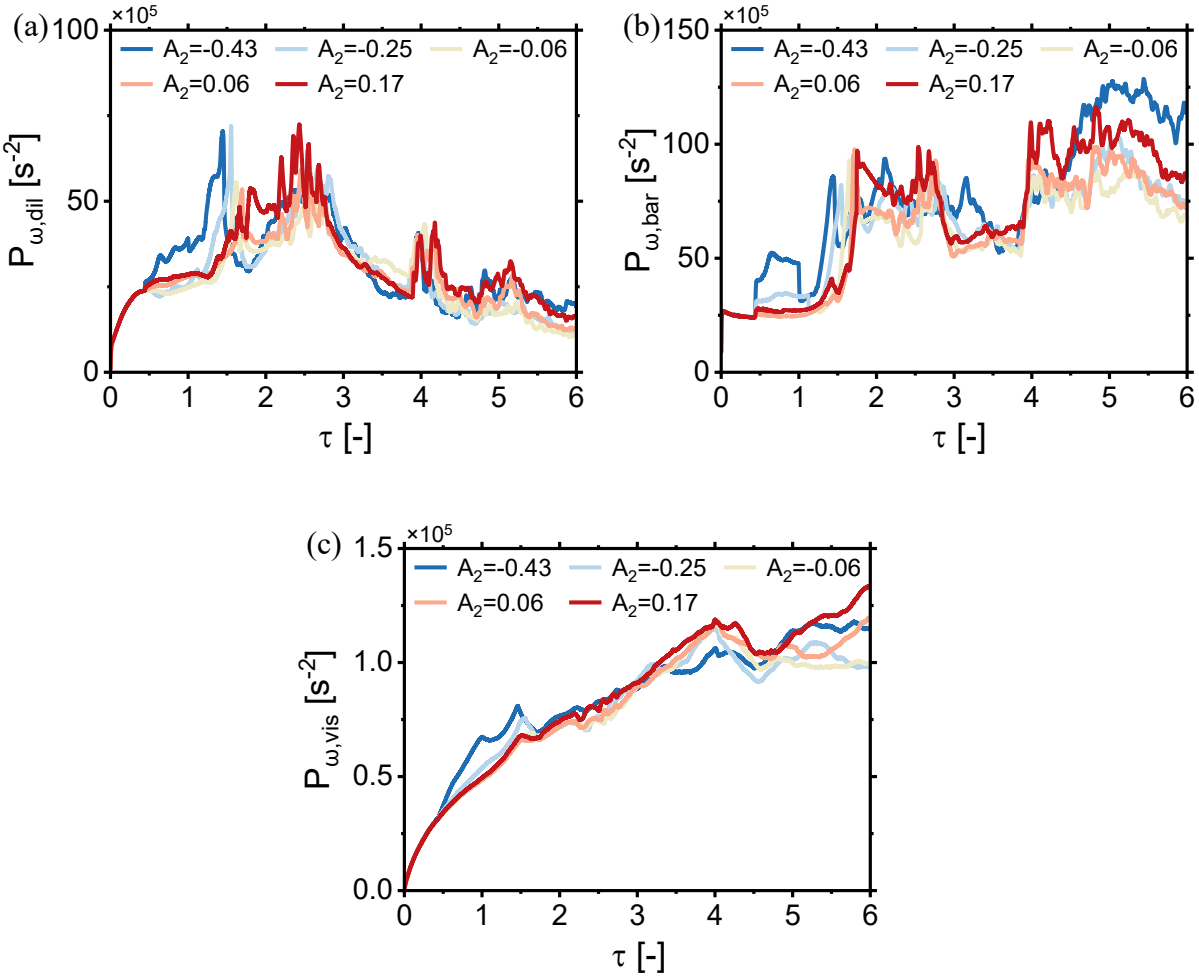

Figure 3-30. Spatially integrated fields of (a) dilatation term, (b) baroclinic term, and (c) viscosity term.

3.4.2.4.2. Circulation

Figure 3-31 illustrates the positive, negative, and net components of the circulation, respectively. It can be observed that the magnitude of the positive circulation is consistently smaller than that of the negative circulation, resulting in a net circulation magnitude that remains below 0. The magnitude of the net circulation increases with the Atwood number rising. The net circulation can be predicted by the linear summation of the positive circulation and the negative circulation. Since the Atwood numbers for the outer cylinders are greater than 0, the process of IS passing through the outer cylinder can be viewed as the shock-heavy gas cylinder interaction, for which circulation can be predicted using either the PB model or the SZ model. For the scenarios where $A_2 < 0$, the passage of TS_1 over the inner cylinder can be regarded as the shock-light gas cylinder interaction, for which circulation can be predicted by the PB model or YKZ model. After linearly summing the PB model or SZ model for the

outer cylinder and the PB model or YKZ model for the inner cylinder, the comparison of net circulation between numerical and theoretical results is presented in Table 3-9. The findings reveal that the absolute value of the relative error obtained from the summation of the SZ model and PB model is under 5%, indicating an accurate prediction of net circulation.

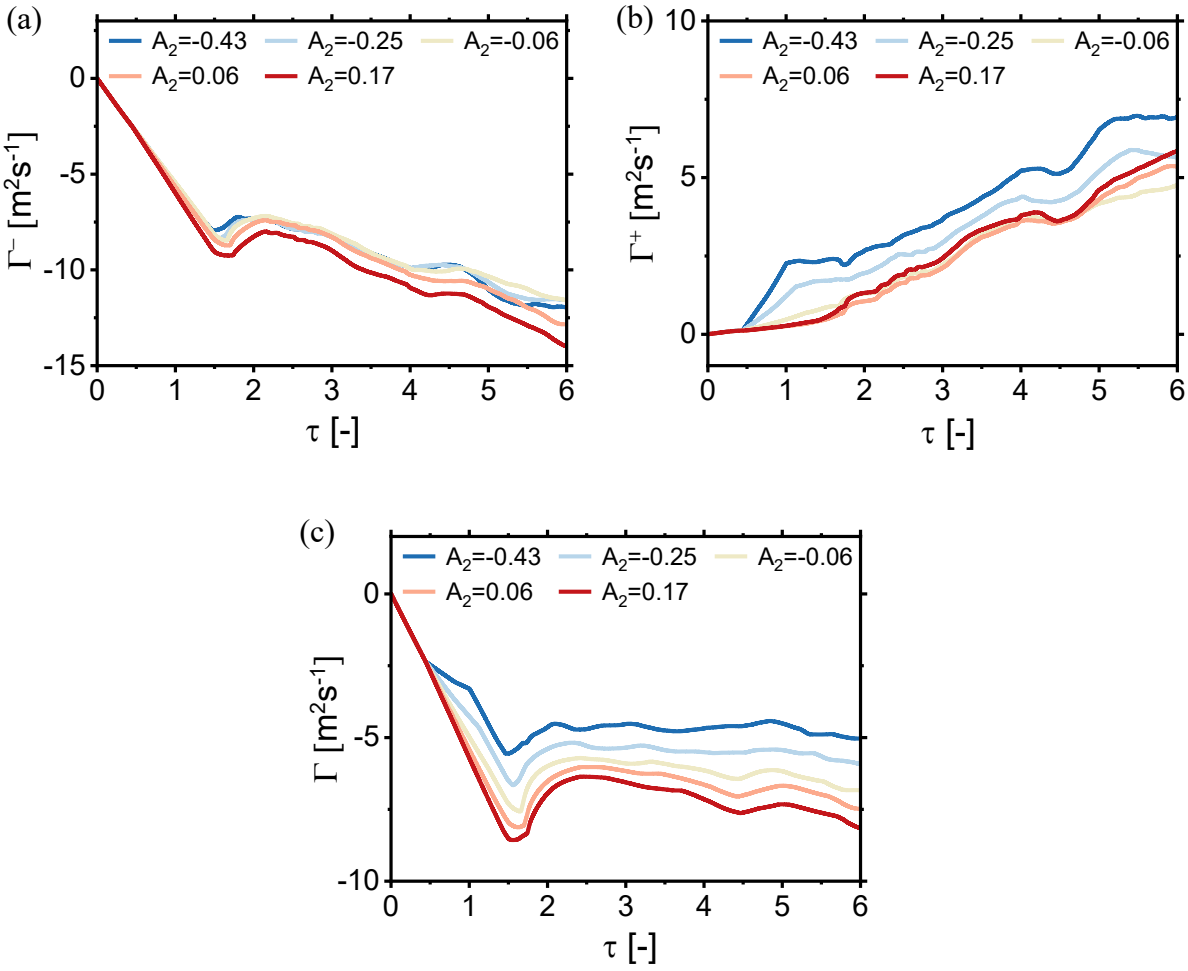

Figure 3-31. The (a) negative, (b) positive, and (c) net component of the circulation.

Table 3-9. Comparison of circulation from the numerical simulation results (Γ_{sim}) and theoretical predictions by the summation of different models at τ = 1.32 (the unit of circulation is m²/s).

Cases	Γ_{sim}	Γ_{PB+PB}	|error|	Γ_{PB+YKZ}	|error|	Γ_{SZ+PB}	|error|	Γ_{SZ+YKZ}	|error|
A_2=–0.43	−5.56	−5.07	8.81%	−5.76	3.60%	−5.39	3.06%	−6.09	9.53%
A_2=–0.25	−6.65	−6.02	9.47%	−6.37	4.21%	−6.35	4.51%	−6.70	0.75%
A_2=–0.06	−7.51	−6.88	8.39%	−6.98	7.06%	−7.21	3.99%	−7.30	2.80%

For scenarios where A_2 >0, the passage of TS_1 over the inner cylinder can be considered as a shock-heavy gas cylinder interaction. Similarly, the circulation in these cases can be predicted using either the PB or SZ model. After linear summation of the PB model or SZ model for the outer cylinder and the PB model or SZ model for the inner cylinder, the comparison of net circulation between numerical and theoretical results is listed in Table 3-10. The results indicate that the summing SZ and PB model or SZ and SZ model accurately predict the net circulation, with the absolute value of the relative error being under 5%.

Table 3-10. Comparison of circulation from the numerical simulation results (Γ_{sim}) and theoretical predictions by the summation of different models (the unit of circulation is m^2/s).

Cases	Γ_{sim}	Γ_{PB+PB}	|error|	Γ_{PB+SZ}	|error|	Γ_{SZ+PB}	|error|	Γ_{SZ+SZ}	|error|
A_2=0.06	−8.02	−7.51	6.36%	−7.57	5.61%	−7.83	2.37%	−7.89	1.62%
A_2=0.17	−8.31	−8.00	3.73%	−8.12	2.29%	−8.32	0.12%	−8.44	1.54%

3.4.2.5. Mixing

Figure 3-32 illustrates the mean mass fraction of both outer and inner cylinders. The mean mass fractions of SF_6 within the gas ring remain nearly identical due to constant Atwood number across the outer interface. As the magnitude of the Atwood number increases, a reduction of mean mass fraction of SF_{6V} in the inner cylinder is observed after the IS passes over the outer interface. This behaviour primarily results from enhanced dilution of the ambient air from the gas ring, thereby promoting mixing between the different gases.

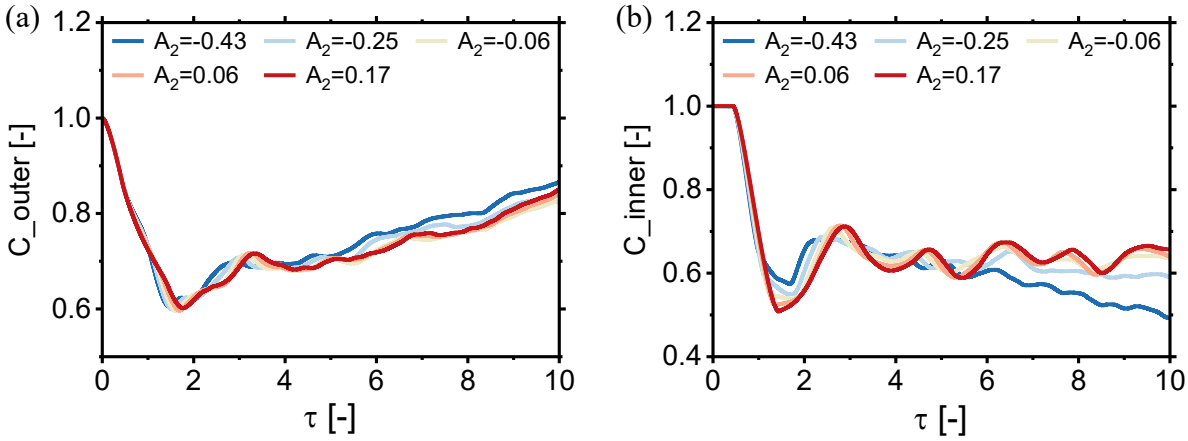

Figure 3-32. Mean mass fraction histories of the (a) outer cylinder and (b) inner cylinder.

3.5. Remark

The influences of initial conditions including shock Mach numbers and Atwood numbers on the evolution of the inert double-layer cylinder are investigated qualitatively and quantitatively.

For the scenarios of varying Mach numbers, different intensities of the IS (M = 1.27, 1.5, 1.7, and 2.1) are considered. As the Mach number increases, the UI_1 undergoes more pronounced compression due to the higher shock intensity, accompanied by enhanced baroclinic vorticity deposition. This accelerates the formation and growth of vortex pairs. Notably, the jet formation occurs earlier at a Mach number of 2.1, yet its length is shorter than other scenarios due to an elevated pressure difference upstream of the jet head following the interaction of the reflected shock with downstream high-pressure regions. A higher Mach number promotes the development of the primary vortex pair, thereby enhancing the acceleration of heights. Negative vorticity is deposited at the outer interface, while positive vorticity is deposited at the inner interface. Higher Mach numbers amplify vorticity deposition, leading to more pronounced rolled-up vortical structures over time. The dilatation and baroclinic terms dominate vorticity production, with their magnitudes increasing as the Mach number rises. The summation of the SZ model and PB model accurately predicts net circulation. Moreover, the summation of the PB model and PB model has a better prediction under the scenarios of higher Mach numbers. For the analysis of mean mass fraction histories, an intense shock wave can promote the mixing of SF_6 and air.

In terms of Atwood number effects, two types of gas layer configurations are considered in this study: an A/B/A-type gas layer (A_1 = 0.50, 0.39, 0.19, and −0.20) and an A/B/C-type gas layer (A_2 = −0.50, −0.25, −0.06, 0.06 and 0.17). For the scenarios of A/B/A-type gas cylinder, reduced baroclinic vorticity deposition slows the development of primary and secondary vortex pairs as the Atwood number decreases for $A_1 > 0$, accompanied by the widths and heights of outer and inner cylinders stabilizing in later evolution phases. The dilatation, baroclinic, and viscous terms diminish with decreasing A_1. The first peak values of dilatation terms appear due to the generation of vortex pairs and stretched structures around the vortex core. In addition, the summation of the SZ model and PB model provides reliable circulation predictions. When $A_1 < 0$, distinct flow patterns emerge. A vortex pair emerges and propagates in the upstream direction at the upper and lower poles of the outer interface, while another vortex pair moving downstream is generated originating from the DI_2.

For the scenarios of the A/B/C-type gas cylinder, secondary vortex pairs form at the outer cylinder's downstream interface, with their separation distance decreasing as the Atwood number rises for $A_2 < 0$. Pressure contour analysis reveals that this behaviour arises from substantial baroclinic vorticity deposition, triggered by the interaction of a high-pressure triple point with the downstream interface. Instead of secondary vortex pairs, a jet develops at the downstream interface for positive Atwood numbers. This transition occurs due to shock wave convergence, which generates a localized high-pressure zone after the transmitted shock passes through the focal point. When this shock subsequently impacts the downstream interface, it induces a bulge that evolves into a pronounced jet structure. As the Atwood number increases, the outer widths expand driven by downstream jet formation, while the outer heights contract due to the inward convergence of the inner cylinder. For the inner cylinder, the height reduction is caused by its inherent convergent flow. Following the passage of the IS over the UI_2, higher magnitudes of Atwood number in the dilatation term, baroclinic term and viscous term are greater than other cases. The summation of the SZ and PB model can predict the circulation of cases for $A_2 > 0$, while the summation of the SZ and PB model or the SZ and SZ model can be applied effectively for $A_2 < 0$. Analysis of mean mass fraction histories demonstrates that increased mixing of ambient gas into the gas ring leads to the dilution of SF_6 and promotes gas mixing as the magnitude of Atwood number rises, especially when the incident shock wave passes over the gas cylinder.

CHAPTER 4 Evolution of a reactive double-layer gas cylinder

In this chapter, the computational setups for different Mach numbers and radius ratios are introduced first. The grid independence study is verified by temperature contours shortly after ignition, along with temperature and pressure distributions. Subsequently, the impacts of varying Mach numbers and radius ratios are then qualitatively analyzed. To identify the type of reaction waves, we qualitatively demonstrate time sequences of the temperature and pressure contours shortly after ignition and quantitatively analyze the pressure and temperature with radical H mass fraction across the reaction front. The evolution of both inert and reactive cases is characterized by tracking the transverse bubble diameter and bubble area. The influences of reaction waves on hydrodynamic properties are examined through the analysis of vorticity transport and mixing fraction.

4.1. Computational Setups

Figure 4-1 shows the 2-D computational domain for the reactive and inert shock-double layer cylinder interactions. The left, right, upper, and lower boundaries are set as inlet, outlet, slip wall boundary and symmetry conditions, respectively. For the baseline case, an IS with a Mach number of 2.3 propagates from left to right. The physical time t = 0 μs is defined as the moment when the IS reaches the UI_1 of the double-layer gas cylinder. The center of the gas cylinder is located at the coordinate origin (0,0). The radii of the outer and inner cylinders are 0.02 m and 0.01 m, respectively, for the baselined case. To enhance computational efficiency, local grid refinement is applied to the region of bubble evolution with 19.5R x 3.5R. The ambient gas and the gas in the inner cylinder are pure N_2, while the gas in the ring is a mixture of H_2, O_2, and Xe in a ratio of 2:1:3.67 molar fractions. The initial pressure and temperature are set as 0.5 atm and 350 K, and the corresponding densities of N_2 and the mixture are 1.352 kg/m³ and 0.488 kg/m³, following the initial conditions used in Diegelmann's study [56]. This study investigates the effects of varying Mach numbers ($M = 2.13-2.9$) and inner-to-outer radius ratios ($\lambda = 0.25-0.75$) on the evolution and mixing of both reactive and inert double-layer gas cylinders, where identical initial physical conditions are maintained for both reactive and inert cases.

To independently track the evolution of the outer and inner cylinders, N_2 in the inner cylinder is replaced by a hypothetical gas, N_2v, which retains identical physical properties. By monitoring the Y_{N_2} and the hypothetical gas Y_{N_2V} within the inner cylinder, the distinct

physical characteristics and behaviours of the outer and inner cylinders can be effectively identified. The interfaces between the inner cylinder and the gas ring, as well as between the gas ring and the ambient gas, are defined in terms of the molar fraction of N_2 and N_2v:

$$X_{N^2} = \frac{1 + \tanh\left(\left(\sqrt{x^2 + y^2} - R\right) \cdot \sigma\right)}{2}$$
$$X_{N_2v} = \frac{1 - \tanh\left(\left(\sqrt{x^2 + y^2} - r\right) \cdot \sigma\right)}{2} \quad \textbf{(4-1)}$$

Here, the molar fraction of the mixture within the gas ring is then given by $X_{\text{mixture}} = 1 - X_{N_2} - X_{N_2v}$. The same value of σ is used as in the previous chapter.

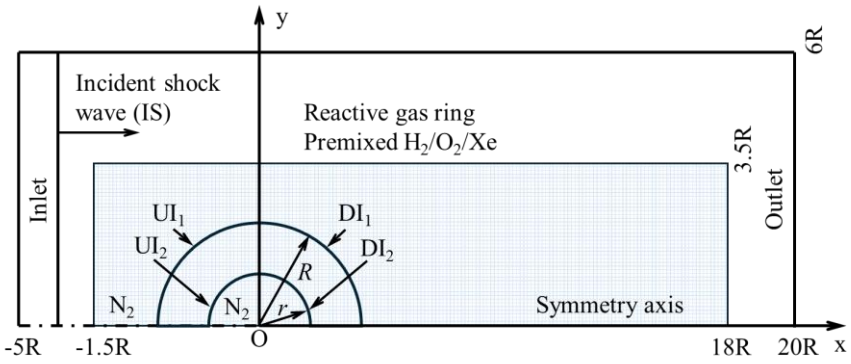

Figure 4-1. Schematic of the computational domain for inert and reactive double-layer gas cylinder.

4.2. Grid independence study

The grid convergence study uses four different uniform grids with minimum sizes of 200 μm, 100 μm, 50 μm and 25 μm, corresponding to 100, 200, 400, and 800 grid points across the radius of the outer interface. Figure 4-2 presents the temperature contours for various grid resolutions shortly after ignition for the baseline case. The results indicate that while grid resolution does not affect large-scale vortex structures, it is closely related to small-scale vortex structures at the interfaces. The coarse grids fail to simulate the ignition phenomenon and result in blurred outer and inner interfaces, suppressing KH instability. In contrast, finer grids capture the ignition location near the DI_1 and reveal the development of KH instabilities with detailed small-scale vortex structures. DDT is highly sensitive to grid resolution, ignition followed by a detonation wave can be simulated for scenarios of both finer grid resolutions. Figure 4-3 shows the temperature and pressure distributions across flame fronts. As grid resolution increases, the rapid rises in temperature and pressure across the reaction wave are sharply resolved, and the peak values for the two finest grids are nearly identical. As a result,

the second finer grid resolution of 50 μm, in which the total number of grid cells is 24 million, is sufficient to capture the essential properties of the reaction wave with promising computational efficiency.

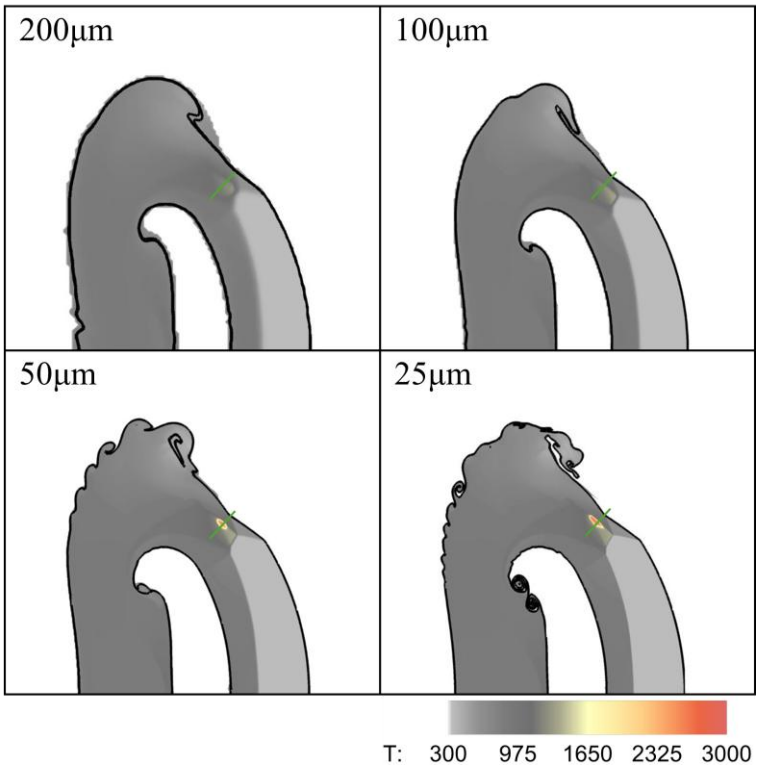

Figure 4-2. Temperature contours after ignition for different grid resolutions at t = 50.0 μs.

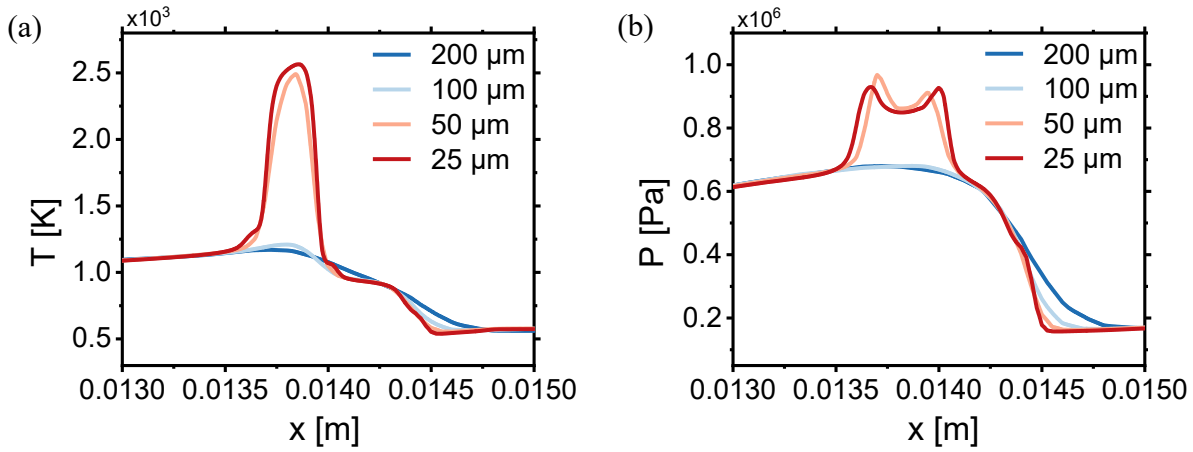

Figure 4-3. The temperature and pressure distributions over the reaction front for different grid resolutions.

4.3. Effects of Mach number on RSBI scenarios

4.3.1. Evolution of RSBI and ISBI

To investigate the effects of the incident shock intensity (M = 2.13, 2.3, 2.5, and 2.9) on reactive and inert double-layer gas cylinders, the temperature contours for $Y_{\mathrm{Xe}} > 0.1$ under four different Mach numbers are analyzed, as listed in Figure 4-4.

For the inert case at M = 2.13, the impact of IS on the upstream interface of the UI_1 induces the RM instability and compresses the UI_1 (τ = 0.37). The large-scale primary vortex pair caused by RM instability develops near the diametral plane of the outer cylinder, while the small-scale vortex structures induced by secondary KH instability emerge at UI_1 close to the primary vortex pair (τ = 1.22). Complex shock structures within the gas ring interact with the DI_1, leading to the formation of a secondary vortex pair (τ = 1.87). Similarly, the transmitted shock wave interacting with the UI_2 triggers RM instability, resulting in the formation of large-scale vortex pairs near the diametral plane of the inner interface that propagate upstream. At the late stage of evolution (τ = 8.94), the primary vortex pairs of the outer and inner cylinders become fully mixed, and the bubble material connecting the counter-rotating vortex pair becomes thinner, referred to as the bridge region by Tonkins et al. [21]. With the Mach number increasing, similar wave patterns and interface morphologies of the double-layer gas cylinder can be observed. At higher Mach numbers M = 2.5 (τ = 1.19) and M = 2.9 (τ = 1.05), a distinct high-temperature region appears near DI_1.

For the reactive case at M = 2.13, the combustible gas mixture is ignited near DI_1 at τ = 1.22. A deflagration wave is initiated, propagating at subsonic speed and reaching the UI_1 in the long-term evolution. The deflagration wave has minimal impact on the bubble dynamics, with the morphology of the reactive case remaining consistent with that of the inert case. At the late stage of evolution (τ = 8.94), the vortices of the reactive case exhibit a larger scale compared to the inert case due to the heat release leading to the expansion of the gas mixture. At a Mach number of 2.3, the gas mixture is ignited near the DI_1 at τ = 1.10, with the ignition time occurring earlier. Instead of a deflagration wave, a detonation wave propagating upstream is formed, reaching the UI_1 at τ = 1.36. Strong heat release and density reduction caused by the detonation wave, compared to the deflagration wave, lead to a more rapid expansion of the bubble. The reactive gas cylinder exhibits a faster growth rate of the outer interface and a larger area in the gas ring than the inert cases (τ = 3.29). At τ = 8.77, a secondary vortex pair near the symmetry axis appears instead of the bridge region.

As the Mach number rises to 2.5, the gas mixture is ignited near the diametral plane of the inner gas cylinder at $\tau = 0.81$, subsequently propagating through the entire gas ring by $\tau = 1.19$.

With a further increase to 2.9, the shock waves ignite the gas mixture near the upstream pole of the outer interface. The ignition time occurs earlier with increasing Mach number. The detonation wave is generated, moving downstream at supersonic speed through the entire gas ring. In the long-term evolution, a jet structure travelling upstream forms near the symmetry axis, and the jet propagation is consistent with "vortex ring projectile" as described in Zabusky and Zeng [90].

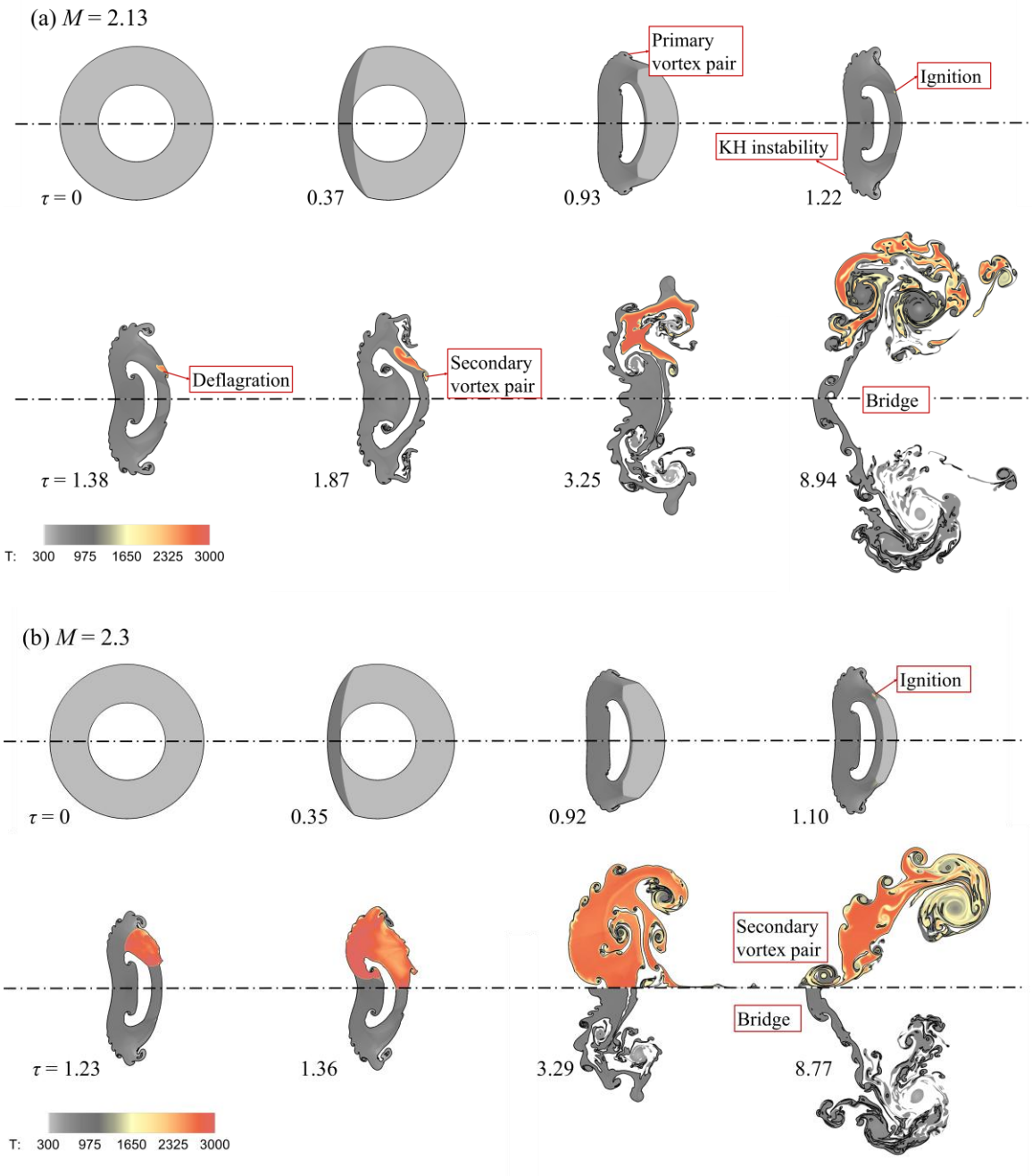

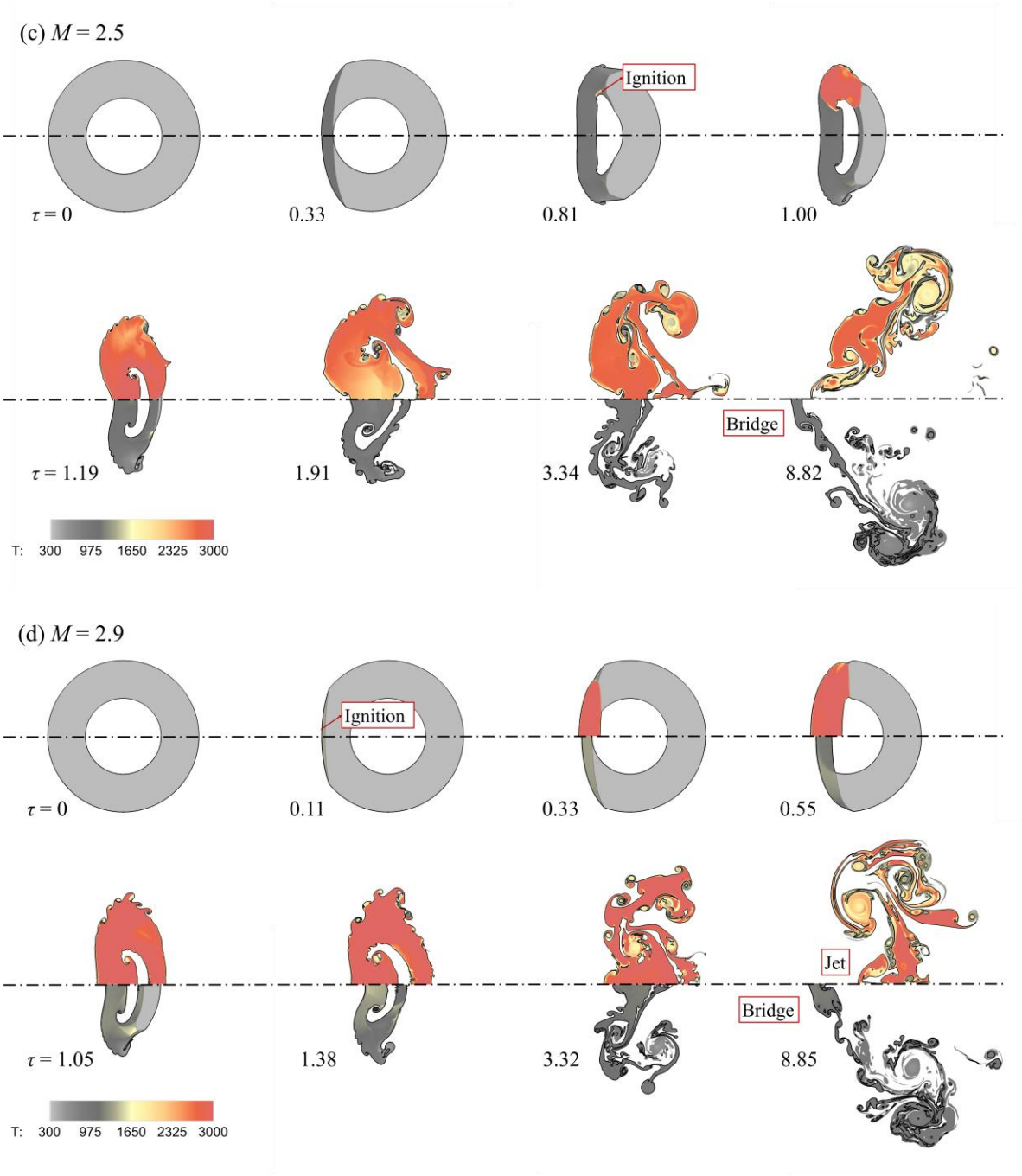

Figure 4-4. Temperature contours for RSBI and ISBI cases with different Mach numbers, (a) Mach 2.13, (b) Mach 2.3, (c) Mach 2.5, and (d) Mach 2.9. The upper regions depict the reactive scenarios, and the lower regions depict the inert scenarios.

4.3.2. Ignition characteristics

To investigate the process and mechanism of hotspot formation at various Mach numbers, the time sequence of the normalized pressure gradient magnitude (*DP*), the enhanced density gradient, the pressure and temperature contours are presented. Here, the enhanced density gradient is obtained using $\log_{10}(\nabla\rho - 1)$.

Figure 4-5 illustrates the scenario at a Mach number of 2.13. The interaction between the IS and UI_1 results in the formation of the TS_1, with the generation of the RS_1 propagating upstream. As TS_1 moves downstream and encounters UI2, the TS_2 is generated, accompanied by the emergence of an RRW at $\tau = 0.45$. By $\tau = 0.85$, IS traverses the diametral plane of the outer interface, resulting in the formation of a DS. Upon crossing the outer interface, the DS undergoes refraction, generating an RDS and an attached shock wave S_2 along the outer interface. The convergence of RDS, S_2, and the downstream-propagating TS_1 leads to the formation of a TP. Due to the faster propagation speed of TS_2 relative to TS_1, an FPS and an attached shock wave S_1 develop near the inner interface. As TS_2 continues to propagate downstream, the increasing inclination angle between TS_2 and the inner interface induces the formation of the RS_2. TS_1, RS_2, S_1, and FPS are interconnected through a Mach stem, accompanied by the emergence of two TPs and a localized rise in temperature and pressure. Additionally, the convergence of two shear layers upstream of the Mach stem further amplifies the temperature and pressure, giving rise to the generation of a triangular HT_1 and HP_1 region bounded by the Mach stem and the shear layers. As TS_2 transmits across DI_2, it generates the TS_3. RS_2 propagates along the trajectory of TS_1 toward S_2 until the two TPs collide at $\tau = 0.93$, further elevating the temperature and pressure, thereby generating the HT_2 and HP_2 region upstream of the merging of RS_2 and S_2 (Merged-$shock_1$) at $\tau = 1.04$. To match the high temperature and pressure post of the Merged-$shock_1$, a shock wave S_3 is formed. S_3 propagates toward S_1 along the direction of the MS, the collision of two TPs giving rise to the HT_3 and HP_3 region at $\tau = 1.13$. By $\tau = 1.17$, the merging of S_3 and S_1 (Merged-$shock_2$), TS_3, Merged-$shock_1$, and RDS are interconnected through the Mach stem, along with the emergence of two TPs. The subsequent collision of these two TPs further amplifies temperature and pressure due to complex shock-shock interaction, resulting in the formation of the HT_4 and HP_4 region. Ultimately, the hotspot occurs in this stage.

At a Mach number of 2.3, the wave structures and morphologies of double-layer gas cylinder for $\tau < 1.06$ exhibit agreement consistent with that observed at $M = 2.13$ (see Figure 4-6). Following two stages of temperature and pressure elevation, the conditions within the HT_2 and HP_2 regions are sufficient to ignite the combustible mixture, leading to the formation of a hotspot upstream of Merged-$shock_1$. The location of this hotspot closely aligns with that observed in a single-layer bubble, as reported in [56].

When the Mach number is increased to 2.5, similar wave structures and morphologies are observed for $\tau < 0.79$ (see Figure 4-7). The increased shock intensity results in higher post-shock temperature and pressure in the HT_1 and HP_1 regions after the first stage of

heating and compression, reaching a threshold sufficient to ignite the combustible mixture. The hotspot forms at the intersection of the two shear layers upstream of the Mach stem. For a single-layer bubble at Mach 2.5 as documented in [56], the first hotspot appears near the downstream pole of the bubble. The presence of the inner gas cylinder in the double-layer configuration promotes the early formation of a Mach stem and two converging shear layers near its diametral plane, leading to ignition at this location. This causes differences in both the ignition position and timing compared to the single-layer bubble scenario.

As the Mach number further increases to 2.9, the calculated ignition delay time is 4.2 μs, which is shorter than the time required for TS_1 to reach UI_1 (see Figure 4-8). The strong shock wave directly ignites the gas mixture at the upstream pole of the outer interface at τ = 0.11, followed by a detonation wave, which is consistent with the findings of the single-layer bubble at Mach 2.9 in [56]. The detonation wave merges with the TS_1 and subsequently propagates downstream. After the detonation wave transmitted through DI_2, the combustible mixture is ignited due to its strong shock intensity.

At a Mach number of 2.13, the shock wave intensity is relatively low, and the resulting increase in temperature and pressure is insufficient to directly ignite the gas mixture. Instead, the gas mixture is gradually heated through four stages of shock-shock interactions until the ignition conditions are met, leading to the formation of a subsonic deflagration wave. As the Mach number increases, the stages of heating and compression required for hotspot formation decrease, and the ignition time shortens. When the Mach number reaches 2.9, the shock wave intensity increases significantly, causing a rapid rise in temperature and pressure, which is sufficient to trigger autoignition and initiate a detonation wave.

4.3.3. Identification of reaction wave type

To identify the type of reaction waves following ignition at Mach numbers of 2.3 and 2.5, Figure 4-9 and Figure 4-11 present the time sequence of temperature contours and pressure contours for $Y_{\mathrm{Xe}} > 0.1$ shortly after ignition. For the case of Mach 2.3, the combustible mixture ignites upstream of DI_1, followed by a subsonic deflagration at t = 50.0 μs. By t = 50.8 μs, the lower portion of the deflagration front transits into a supersonic detonation, showing rapid growth of the detonation emerging from the deflagration front (see Figure 4-9). According to the classic Chapman–Jouguet (C–J) detonation theory, the C-J detonation speed is 1091.9 m/s, while the speed of detonation wave across the reaction front is 997.5 m/s. Figure 4-10 illustrates the time sequence of temperature, pressure, and radical H concentration distributions during the DDT. The increase in temperature and pressure as x decreases indicates that the detonation wave propagates upstream. Within the reaction zone,

the decline in the mass fraction of radical H coincides with a pressure rise, which is a hallmark of DDT. The transition to detonation is indicated by the rise in temperature. In the deflagration phase, radicals are distributed smoothly within the reaction front, whereas the steepening of radicals can be observed following DDT. These observations are consistent with the findings in the literature [91].

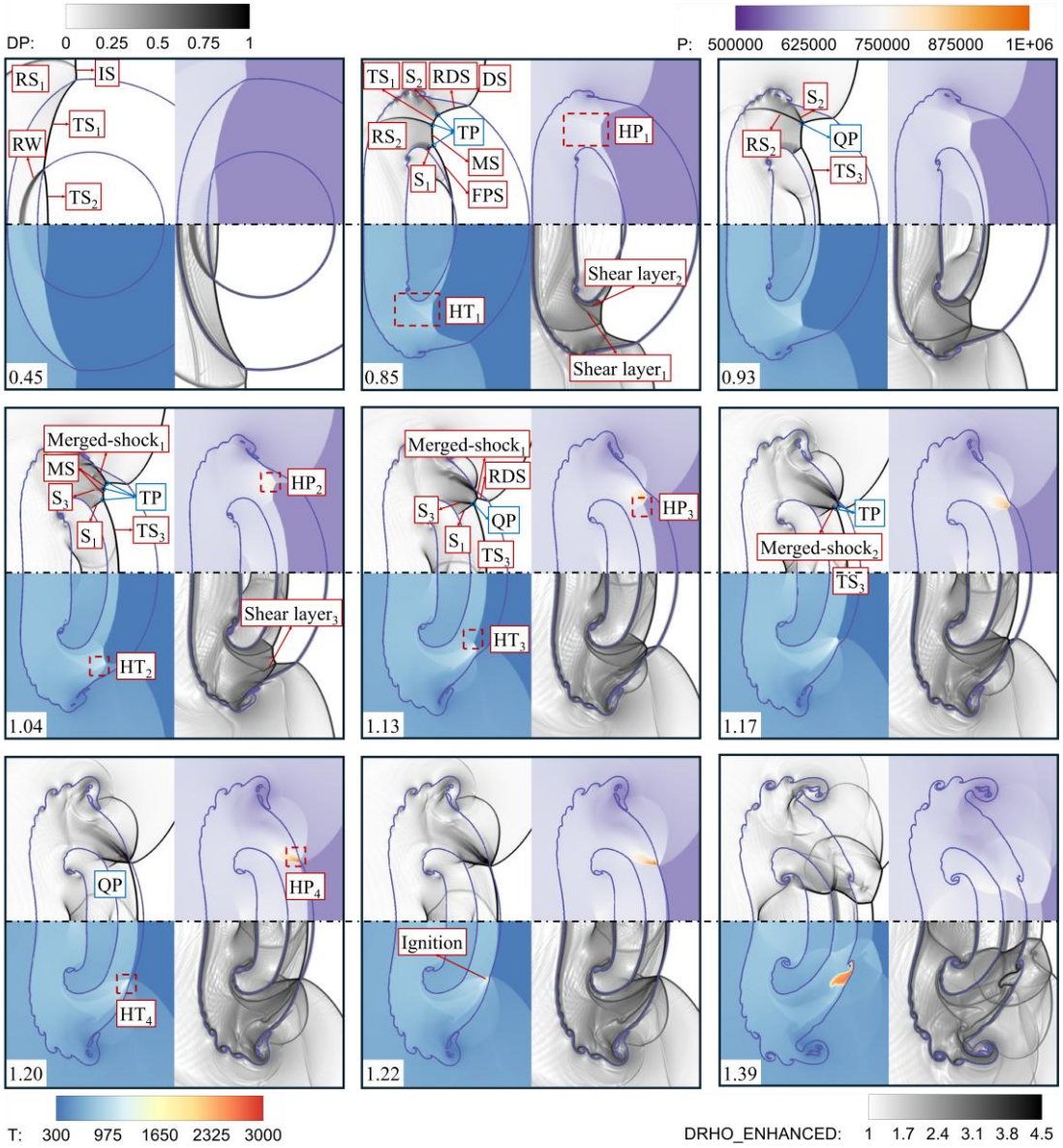

Figure 4-5. Time sequences of the normalized pressure gradient magnitude, the enhanced density gradient, the pressure and temperature contours at the moments surrounding the generation of the hot spot when M = 2.13. IS, incident shock wave; TS_1, the first transmitted shock wave; TS_2, the second transmitted shock wave; TS_3, the third transmitted shock wave; RW, the reflected rarefaction wave; RS_1, the first reflected shock wave; RS_2, the second reflected shock wave; DS, diffracted shock

wave; RDS, refracted diffracted shock wave; FPS, free-precursor shock wave; MS, Mach stem; S_1, S_2, S_3, shock waves; TP, triple point; QP, quadruple point; HP_1, HT_1, the first high-temperature and high-pressure; HP_2, HT_2, the second high-temperature and high-pressure; HP_3, HT_3, the third high-temperature and high-pressure; HP_4, HT_4, the fourth high-temperature and high-pressure.

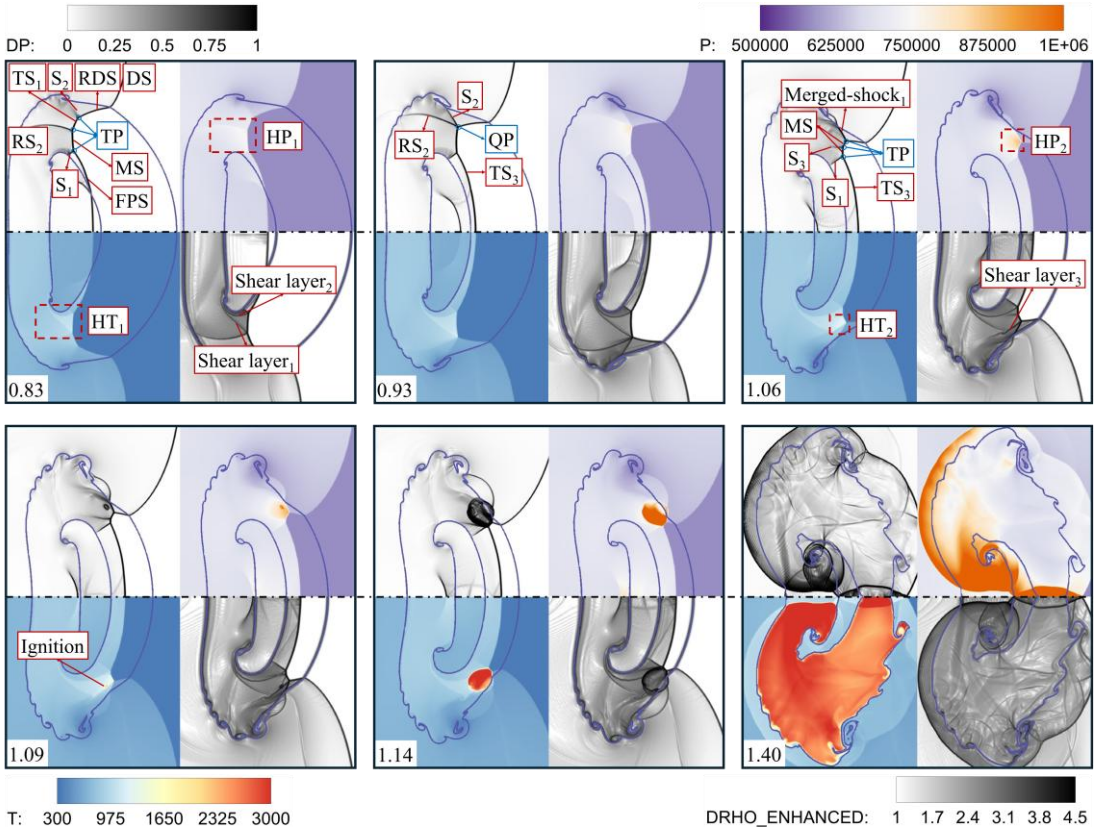

Figure 4-6. Time sequences of the normalized pressure gradient magnitude, the enhanced density gradient, the pressure and temperature contours at the moments surrounding the generation of the hot spot when M = 2.3.

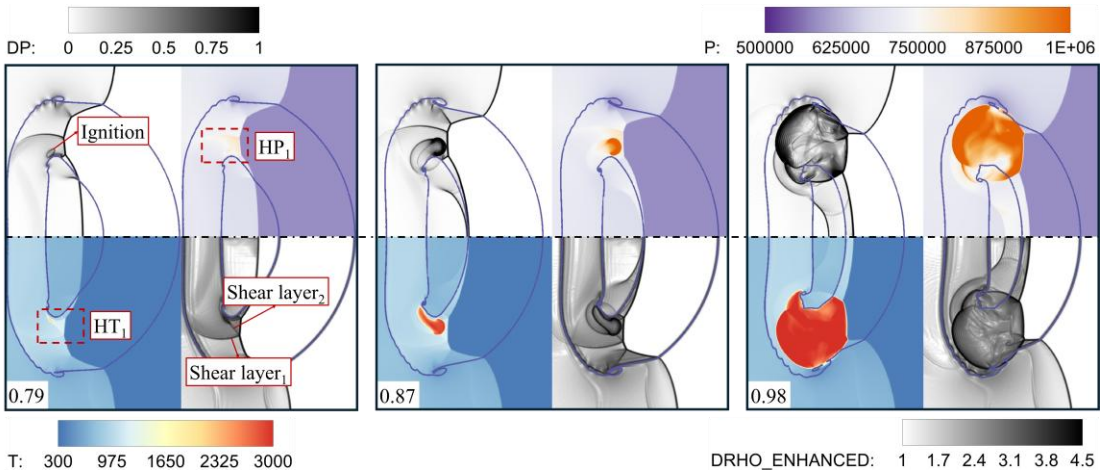

Figure 4-7. Time sequences of the normalized pressure gradient magnitude, the enhanced density gradient, the pressure and temperature contours at the moments surrounding the generation of the hot spot when $M = 2.5$.

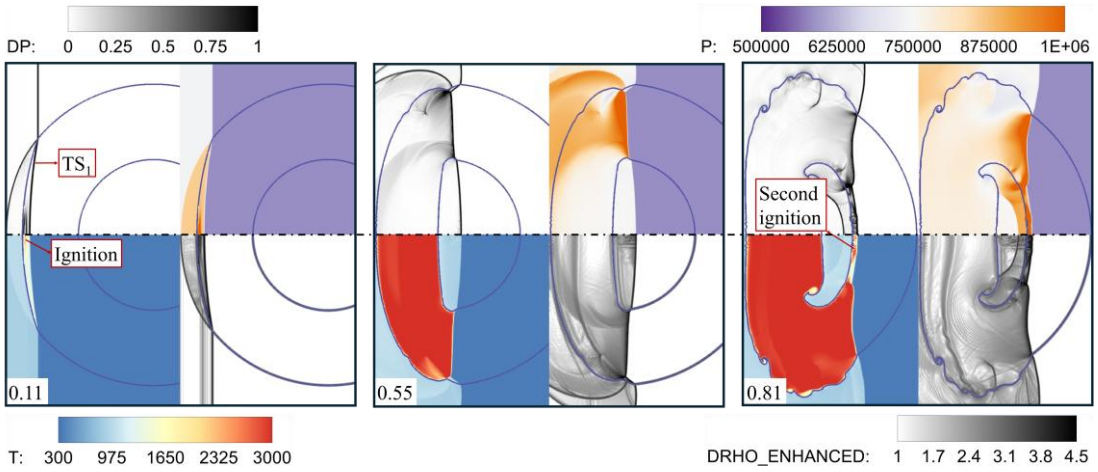

Figure 4-8. Time sequences of the normalized pressure gradient magnitude, the enhanced density gradient, the pressure and temperature contours at the moments surrounding the generation of the hot spot when $M = 2.9$.

For the case of Mach 2.5, ignition occurs near the diametral plane of the inner gas cylinder at t = 33.0 μs, with the deflagration wave propagating toward both UI_1 and DI_1. By t = 36.2 μs, the reaction front moving toward DI_1 transits into a detonation wave, exhibiting rapid growth of a detonation front out of the deflagration front (see Figure 4-11). The transition process is further examined in Figure 4-12, which presents the time sequence of temperature, pressure, and radical H concentration distributions. A decrease in mass fraction of radical H accompanies rising pressure and temperature, with a pronounced steepening of the radicals at the reaction front. These findings confirm the occurrence of DDT following ignition.

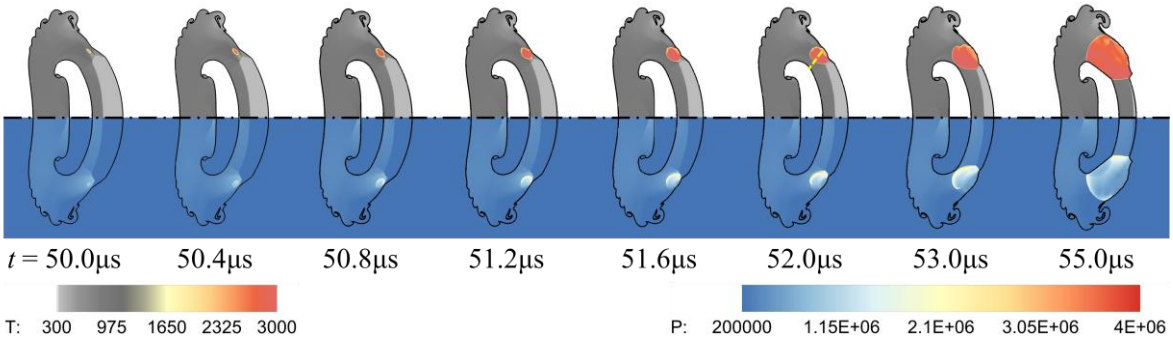

Figure 4-9. Time sequences of the temperature and pressure contours shortly after ignition when $M = 2.3$. The upper regions are temperature contours, and the lower

regions are pressure contours.

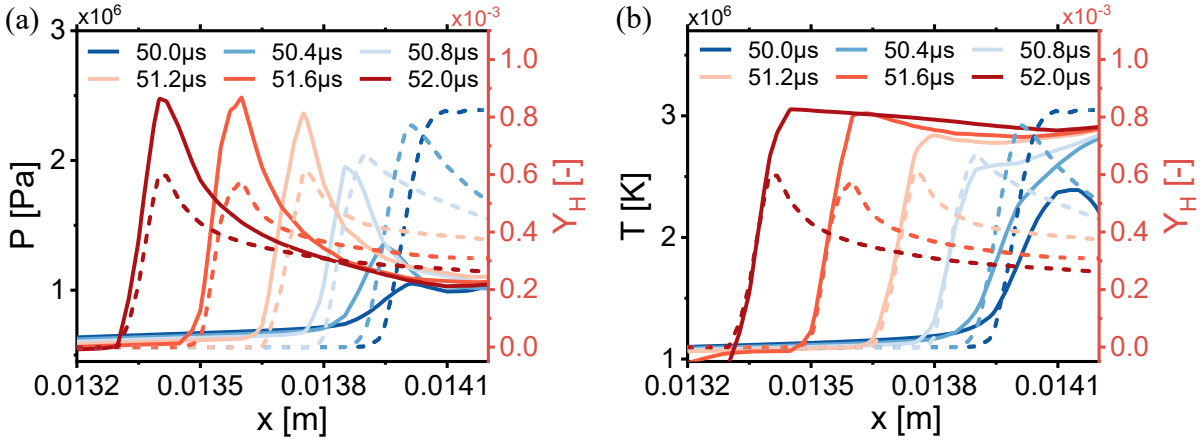

Figure 4-10. (a)Pressure and (b)temperature with radical H mass fraction across the reaction front during DDT (see yellow dashed line in Figure 4-9) for various time sequences when $M = 2.3$. Solid lines represent the pressure and temperature distributions, dashed lines denote the mass fraction of H.

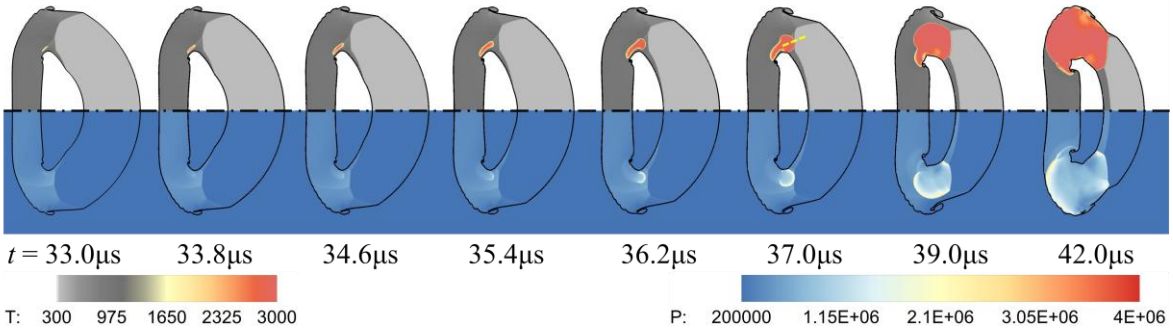

Figure 4-11. Time sequences of the temperature and pressure contours shortly after ignition when $M = 2.5$. The upper regions are temperature contours and the lower regions are pressure contours.

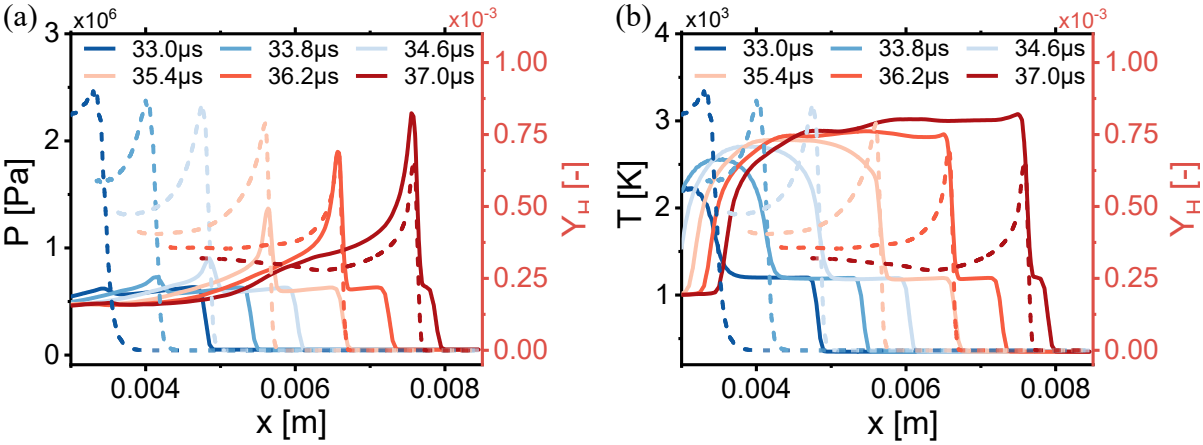

Figure 4-12. (a)Pressure and (b)temperature with radical H mass fraction across the reaction front during DDT (see yellow dashed line in Figure 4-11) for various time sequences when $M = 2.5$. Solid lines represent the pressure and temperature distributions, dashed lines denote the mass fraction of H.

4.3.4. Transverse diameter and area of gas cylinders

4.3.4.1. Transverse bubble diameter

Figure 4-13 illustrates the transverse bubble diameters, which are normalized by the diameters of the outer and inner interfaces. For the inner gas cylinders with inert mixture, a higher incident shock Mach number accelerates the onset of RM instability along the diametral plane of the inner interface, leading to the earlier formation of the primary vortex pair. Vortex roll-up causes curling of the inner interface, leading to portions of the mixture rotating around the vortex core, which slows down the growth rate of the inner gas cylinder as the shock Mach number increases ($\tau > 1.25$). Following ignition, the transverse diameter decreases compared to inert scenarios due to compression by the detonation wave. The occurrence of detonation enhances secondary instabilities in the inner gas cylinder, promoting further development of the vortex pair. Consequently, the transverse diameter experiences a more significant increase compared to inert cases until the mid-stage evolution, where the mixture within the gas ring is fully mixed with N_2 in the inner cylinder.

For the outer gas cylinders with an inert mixture, the DS compresses the outer interface, leading to a reduction in the transverse bubble diameter as the IS passes through the diametral plane. As the primary vortex pair induced by RM instability develops, the transverse diameter increases. The increase in Mach number accelerates the development of the primary vortex pair and curling of the outer interface caused by vortex roll-up, which slows down the growth rate of the outer gas cylinder. For the case of $M = 2.13$, the deflagration wave slightly affects the transverse diameter compared to the inert counterpart after ignition due to the density increase over the reaction front accompanied by spatial ($\tau > 2$). In the cases of $M = 2.3$ and $M = 2.5$, the strong heat release leads to rapid expansion of the gas ring, resulting in a 60% increase in the transverse diameter following detonation. When the Mach number further increases to 2.9, the higher intensity of TS_1 directly ignites the combustible mixture at UI_1. The detonation wave formed by the merging of TS_1 propagates through the diametral plane of the outer interface, causing a 60% increase in the transverse diameter. In the long-term evolution, the evolution levels off much earlier as the shock strength increases. The primary vortices are fully developed, and the bubble gas rotates around the vortex cores, leading to a

slight reduction in the transverse bubble diameter. This trend of curve is consistent with the findings in [56].

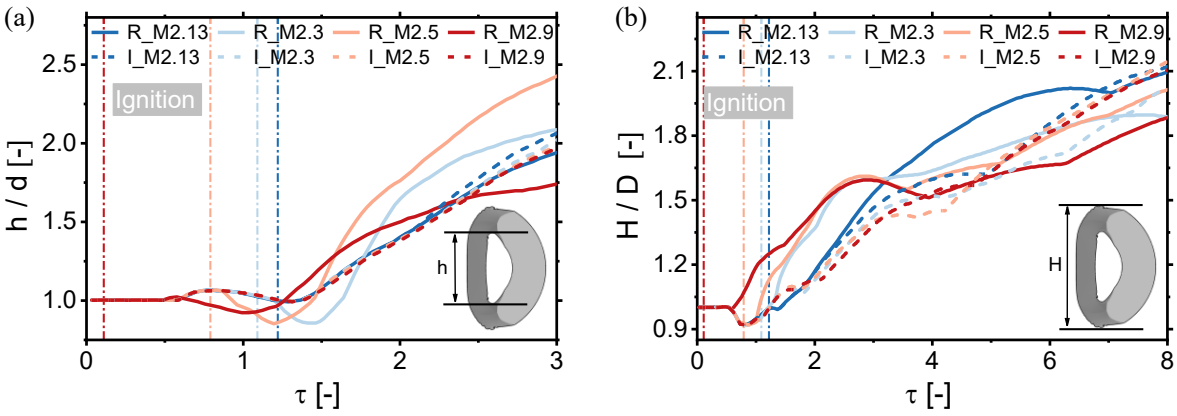

Figure 4-13. Transverse bubble diameters of (a) inner cylinder and (b) outer cylinder for RSBI and ISBI cases.

4.3.4.2. Bubble area

Figure 4-14 shows the areas of the inner cylinder and gas ring, which are normalized by the initial areas of the inner cylinder and gas ring, respectively. The areas of the inner cylinder and gas ring are defined as the regions where $Y_{N_2V} > 0.5$ and $Y_{Xe} > 0.5$, respectively.

The area of the inner gas cylinder decreases under the compression of TS_1. The compression effect becomes more pronounced as the incident shock Mach number increases. At Mach 2.13, the propagation velocity of the deflagration front is lower compared to the evolution of the hydrodynamic instabilities, resulting in a slight compression on DI_2. For higher Mach numbers at 2.3 and 2.5, the supersonic detonation wave induces a significantly stronger compression effect on DI_2 compared to the inert counterparts following ignition. Further increase to Mach 2.9, the faster propagation velocity of the detonation wave relative to TS1 in the inert counterpart causes it to pass over the diametral plane of the inner interface earlier, further compressing the area of the inner cylinder. As the detonation front propagates through the entire inner cylinder, the generation of secondary instabilities promotes the development of the vortex pair, leading to a slight increase in area.

The area of the gas ring filled with an inert mixture initially decreases due to the compression of IS on UI_1. As the primary vortex pair develops under the influence of RM instability, the area gradually increases. Following ignition, the deflagration wave induces a slow expansion of the gas ring area, whereas the strong heat release and density reduction associated with the detonation wave cause rapid expansion in the area. As the Mach number decreases, the hotspot shifts closer to DI_1, increasing the induction time for which the

detonation front sweeps across the gas ring, thereby leading to the most significant expansion in area. In the long-term evolution, the gas ring area levels off much earlier with increasing Mach numbers. With the full development of primary vortices, the bubble gas rotates around the vortex cores, leading to a slight reduction in bubble area.

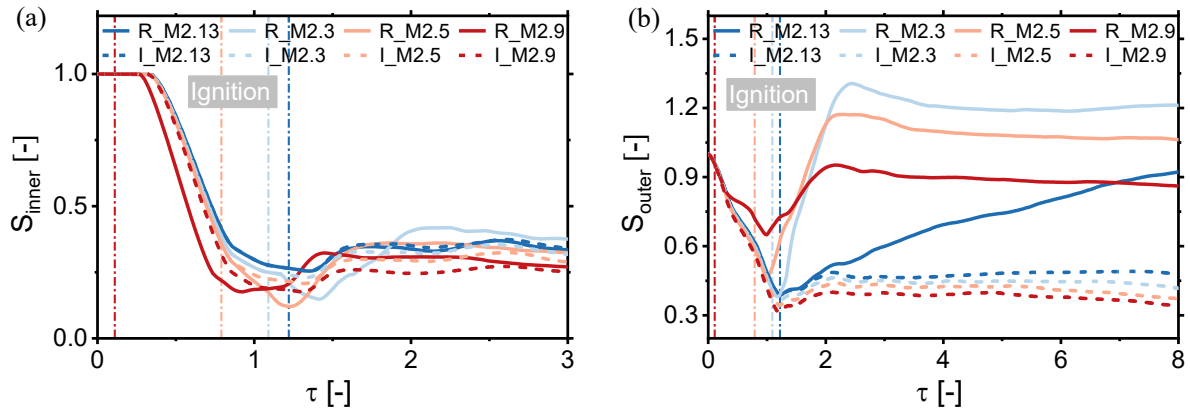

Figure 4-14. Bubble areas of (a) inner cylinder and (b) gas ring for RSBI and ISBI cases.

4.3.5. Combustion completeness

The combustion completeness η s defined to quantitatively analyze the ignition process across different scenarios, which is given by [58]:

$$\eta = 1 - \frac{m_{\mathrm{H_2}}}{m_{\mathrm{H_2},0}} \tag{4-2}$$

As noted in Figure 4-15, the curve of combustion completeness exhibits a sharp increase following ignition, driven by the fast propagation of the detonation wave. After the detonation wave traverses the entire gas ring, the residual reactions progress slowly toward equilibrium, resulting in the curve to level off in the long-term evolution. A similar trend in combustion completeness has been reported in reference [58].

For the scenario with M = 2.13, the curve of combustion completeness increases gradually after ignition under the impact of the deflagration wave. Since the deflagration wave propagates at subsonic speeds, the residual reactions remain in a nonequilibrium state even at the late stage of evolution. For scenarios where M = 2.3 and M = 2.5, the curve initially exhibits a slow rise during a short induction period but then surges rapidly with the onset of DDT.

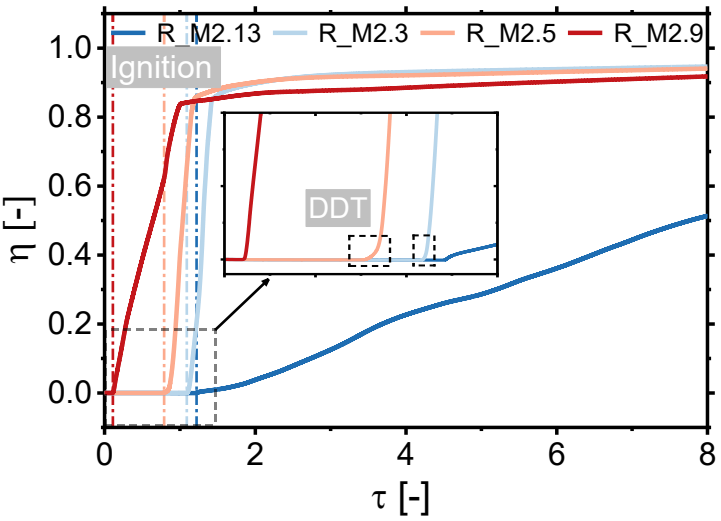

Figure 4-15. Combustion completeness of H_2 for RSBI cases.

4.3.6. Influences of reaction waves on hydrodynamical properties

4.3.6.1. Vorticity transport

Figure 4-16 presents the time sequence of vorticity for both reactive and inert scenarios at various Mach numbers. The initial densities of N_2 and the mixture are 0.49 kg/m^3 and 1.35 kg/m^3, respectively. UI_1 corresponds to a light/heavy interface where $\nabla\rho$ directs inwards radially, while UI_2 corresponds to a heavy/light interface where $\nabla\rho$ directs outwards radially. Since ∇p opposes the shock propagation direction, negative vorticity is deposited at the outer interface, while positive vorticity is deposited at the inner interface. As shown in Figure 4-16, both the deflagration wave front and the detonation wave front generate positive vorticity originating from the hotspot. Due to its relatively weak pressure gradient and lower propagation velocity, the deflagration wave exhibits a limited capacity to perturb DI_2, making it difficult to induce vortex structures at the inner interface. The morphologies of the inner interface remain nearly identical to inert scenarios at τ = 2.44. The detonation wave with a significantly strong pressure gradient acts on the inner interface where vorticity orientation aligns with the detonation, leading to enhanced baroclinic vorticity deposition and accelerating the development of RM instability. The supersonic detonation wave further amplifies velocity shear, inducing KH instability and promoting the formation of both large-scale and small-scale vortex structures at the inner interface. However, as the detonation wave interacts with the outer interface, where the vorticity orientation opposes that of the detonation, local cancellation of vorticity occurs, suppressing both RM instability and KH instability at the outer interface. At a Mach number of 2.9, the detonation wave merges with the TS_1 and propagates throughout the gas ring. Since the detonation wave travels at more

than twice the speed of TS_1, it significantly influences the evolution of the gas cylinder. As a result, KH instability is not aligned along the outer interface at τ = 0.83, and secondary RM instability arises from the KH instability at τ = 2.21.

4.3.6.2. Circulation

Figure 4-17 illustrates the negative, positive, and net vorticity of both inert and reactive gas cylinders. The magnitudes of positive and negative vorticity increase with the deposition of baroclinic vorticity on the outer and inner interfaces, respectively. Following ignition, the positive vorticity is deposited at the reaction front. As the reaction front sweeps through the inner interface, additional baroclinic vorticity is deposited, which leads to a further increase in the magnitude of positive vorticity. The growth rate of positive vorticity accelerates with higher Mach numbers. Under the effect of primary RM instability, the magnitude of negative vorticity at the outer interface rises with increasing Mach numbers. After the reaction front with positive vorticity passes through the entire gas ring, the cancellation of vorticity occurs at the outer interface, resulting in a reduction of both positive and negative vorticity. Then the magnitudes of positive and negative circulation grow mildly. At Mach numbers 2.9, both positive and negative vorticity show a significant growth in both reactive and inert scenarios.

4.3.6.3. Mixing fraction

The interaction between shock waves and the gas cylinder creates a complex flow field, where RM instability and KH instability induce local regions of high mixing fractions. To assess the influences of the reaction waves on the mixing, the molecular mixing fraction defined by Danckwert [92] is employed. The expressions for the mixing fractions among various gas layers can be extended as follows:

$$\Sigma_{\text{outer}} = \frac{\langle X_{\text{N}_2} X_{\text{Xe}} \rangle}{\langle X_{\text{N}_2} \rangle \langle X_{\text{Xe}} \rangle}$$
$$\Sigma_{\text{inner}} = \frac{\langle X_{\text{Xe}} X_{\text{N}_2\text{V}} \rangle}{\langle X_{\text{Xe}} \rangle \langle X_{\text{N}_2\text{V}} \rangle} \quad \textbf{(4-3)}$$

where $\langle \cdot \rangle$ is the spatial average over the computational domain. It can be interpreted as the ratio of molecular mixing to large-scale entrainment by convective motion [56]. Figure 4-18 plots the mixing fractions of both reactive and inert gas cylinders with different Mach numbers. Tomkins referred to three mixing regions: the bridge region, the vortex core and the KH secondary instability region [21].

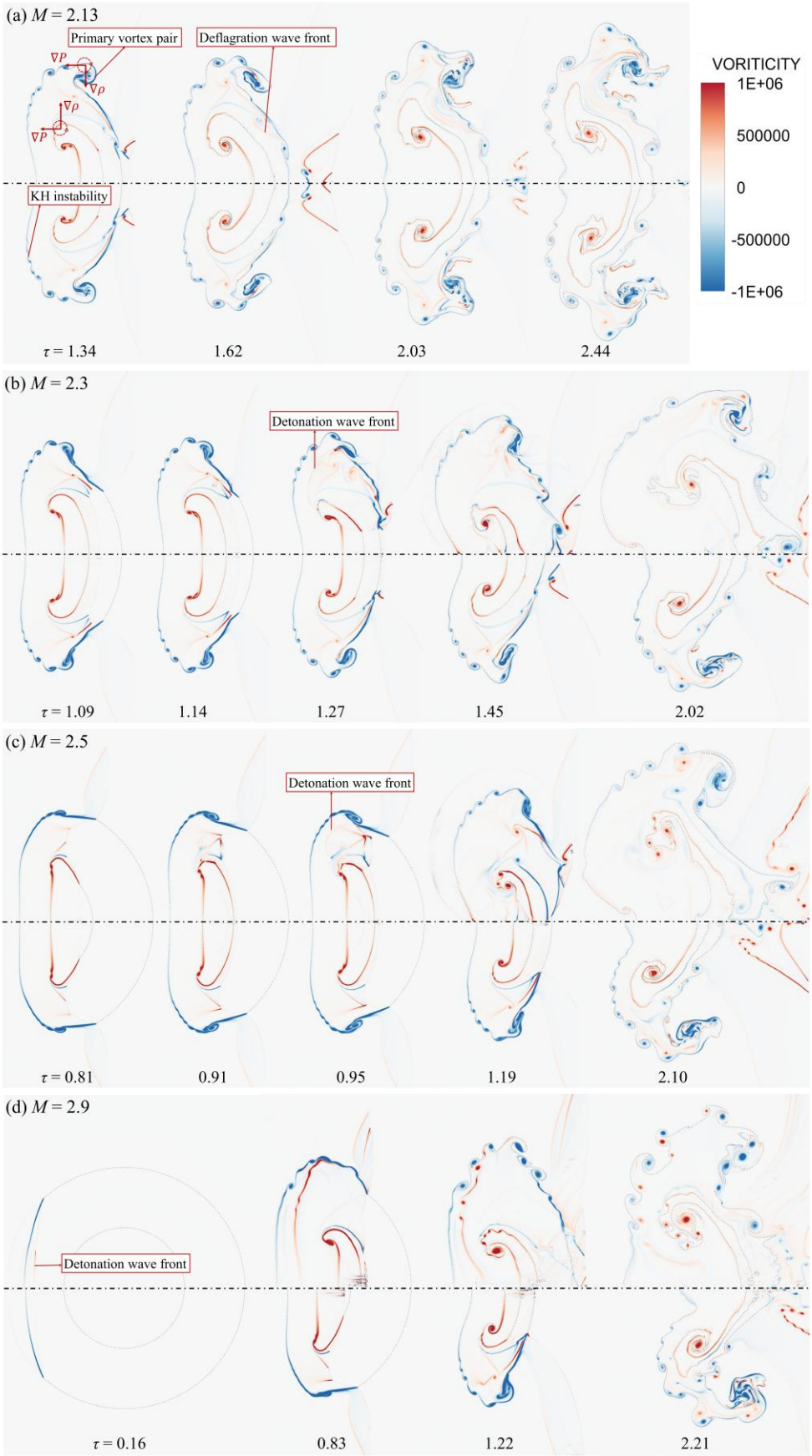

Figure 4-16. Time sequences of vorticity distribution for different Mach numbers.

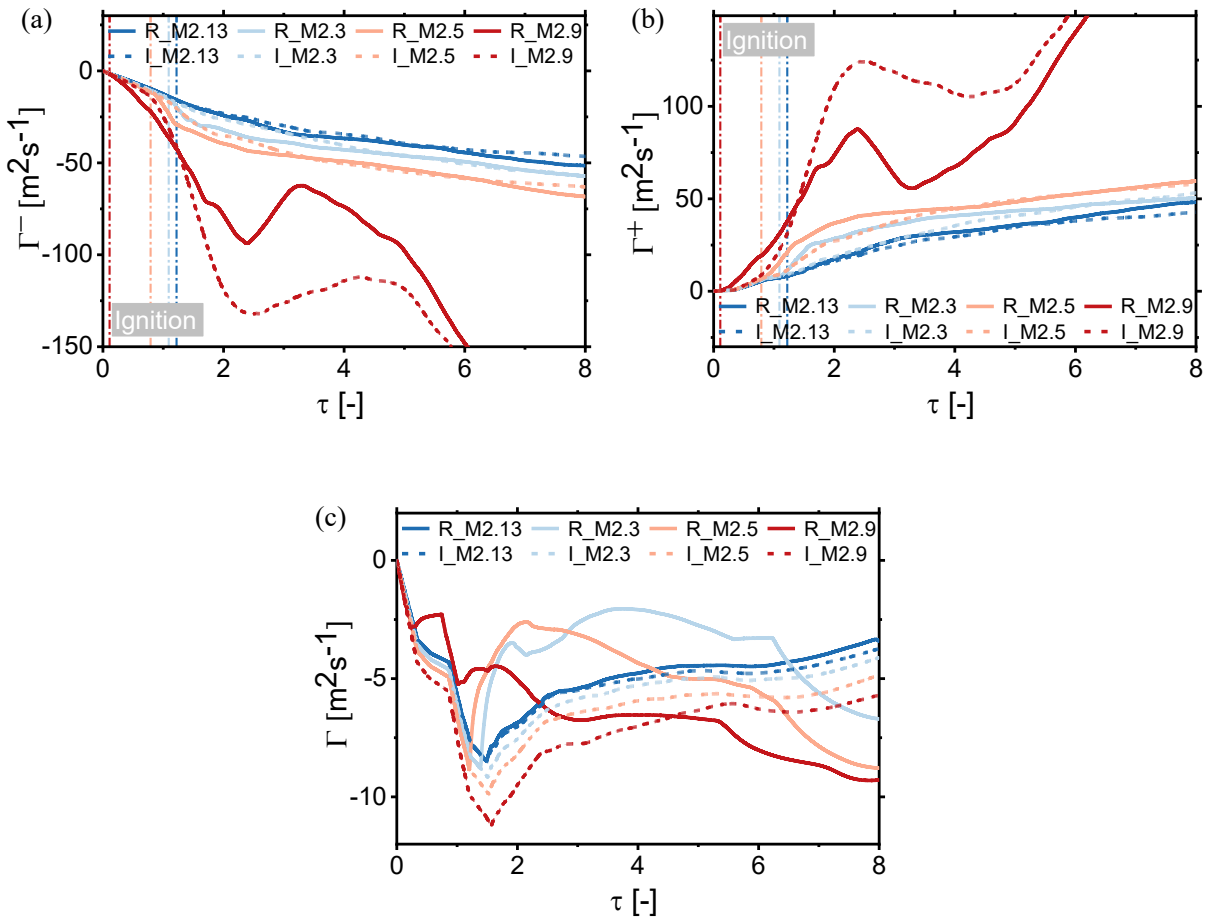

Figure 4-17. The (a) negative, (b) positive, and (c) net component of the circulation for RSBI and ISBI cases.

For the inner gas cylinders, the mixing fraction is examined before the mid-stage of evolution, as the premixed gas in the ring has already sufficiently mixed with the inner N_2. An increase in the incident shock Mach number strengthens TS_1. When TS_1 reaches UI_2, it accelerates the development of RM instability at the interface. This leads to a more rapid formation of vortex cores along the diametral plane of the inner interface, enhancing the mixing fraction. Following ignition, the reaction wave interacts with the inner interface, where the vorticity aligns with its own. This results in increased baroclinic vorticity deposition at the inner interface, further accelerating both RM instability and the growth of secondary KH instability, leading to a higher mixing fraction compared to inert scenarios. At Mach 2.13, the deflagration wave propagates at a much lower velocity and has minimal impact on the instability of the inner interface, causing the mixing fraction to remain nearly identical to the inert counterpart.

For the outer gas cylinders, vortex cancellation occurs at the outer interface after the reaction wave propagates through it which presents opposite vorticity orientation with the reaction wave. This suppresses the development of both RM instability and KH instability, reducing the mixing fraction compared to inert scenarios. At the late stage of evolution, the bridge region disappears under the effects of the detonation wave, weakening gradient intensification via rapid straining. As a result, the mixing fraction decreases by more than 49% compared to inert scenarios.

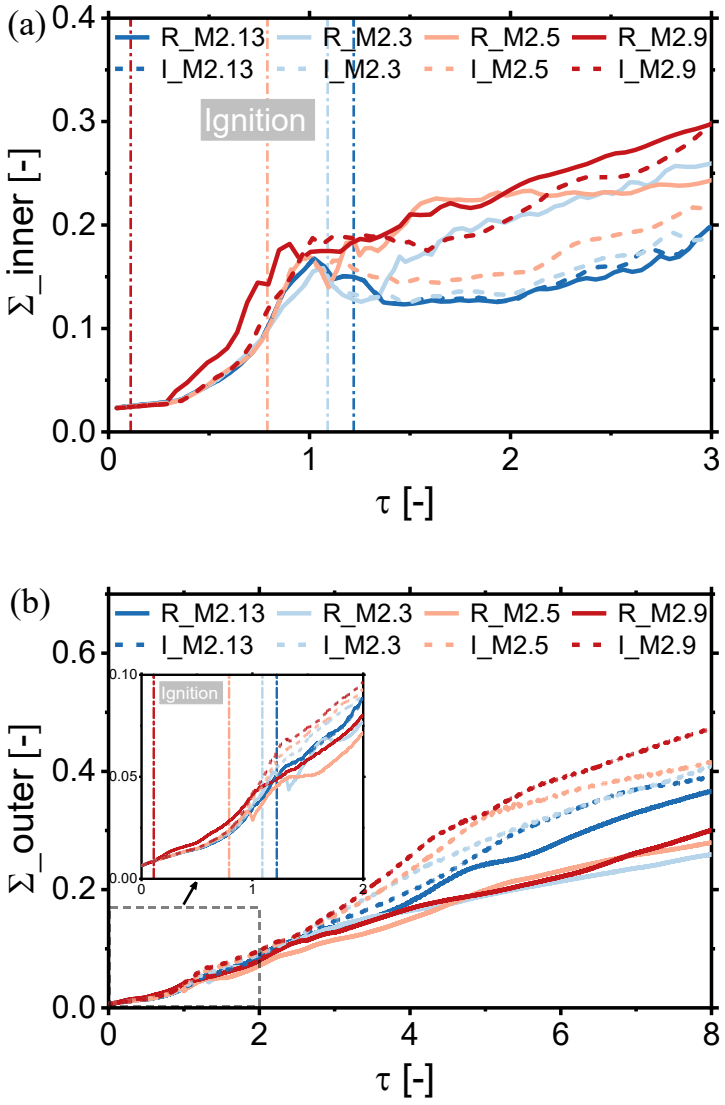

Figure 4-18. Molecular mixing fraction of (a) inner cylinder and (b) outer cylinder.

4.4. Effects of radius ratio on RSBI scenarios

4.4.1. Evolution of RSBI and ISBI

To investigate the impact of varying radius ratios (λ = 0.25, 0.5 and 0.75) on the evolution of both reactive and inert double-layer gas cylinders when the IS is 2.3, a qualitative analysis is performed for radius ratios of 0.25, 0.5, and 0.75. Figure 4-19 shows temperature contours for $Y_{\mathrm{Xe}} > 0.1$ under these different radius ratios.

For the inert cases, UI_1 experiences compression, inducing RM instability at τ = 0.35. Figure 4-20 illustrates that velocity shear differences across the diametral plane of the interface trigger secondary KH instability, with KH vortices fully developing at τ = 1.10. The evolution of KH instability aligns well with the experimental results [93]. The primary vortex pair induced by RM instability emerges near the diametral plane of the outer interface, and the secondary vortex pair appears at the DI_1 at τ = 1.53. A similar interface evolution occurs in single-layer gas cylinders at the early stage [56]. During long-term evolution, the gas in the ring mixes extensively with the surrounding N_2, and the primary vortex structure fully develops. The bubble material connecting the counter-rotating vortex pair becomes thinner, referred to as the bridge region by Tomkins et al [21] near the upstream pole at τ = 8.77. With varying radius ratios, similar wave patterns and morphologies of double-layer gas cylinders are observed at the early stage of evolution. The spanwise distance (in the *y*-direction) between the secondary vortex structures at the outer interface increases with the increasing radius ratio. When λ = 0.75 (see Figure 4-19 (c)), a noticeable jet structure which is produced by the vorticity interacting with the surrounding fluid [15] forms near the upstream pole instead of the bridge region during long-term evolution.

For the reactive case with λ = 0.25 (see Figure 4-19 (a)), the morphologies of the inert and reactive gas cylinders remain identical until τ = 1.23, as ignition has not yet occurred. At τ = 1.23, the shock waves ignite the gas mixture, generating a reaction wave that propagates upstream and passes through UI_1. The strong heat release and reduction in density lead to a rapid expansion of the gas cylinder. At τ = 1.53, the reaction wave reaches UI_1, generating positive vorticity and suppressing the development of secondary KH instability at the interface. The reactive gas cylinder shows distinct growth and characteristics of the interface compared to the inert case. At τ = 8.77, a bridge region connecting the primary vortex pair forms.

For the case with $\lambda = 0.5$ (see Figure 4-19 (b)), the reaction wave propagates upstream to UI_1 following ignition at $\tau = 1.10$, which aligns with the case where $\lambda = 0.25$. At $\tau = 8.77$, a secondary vortex pair structure is generated near the symmetry axis of the gas cylinder.

Further increasing λ to 0.75 (see Figure 4-19 (c)) shortens the ignition time to $\tau = 0.92$. At $\tau = 1.49$, a second ignition occurs near the UI_2, generating a reaction wave that propagates upstream rapidly and reaches UI_1 before $\tau = 1.75$. This causes the gas in the ring to fully react. A jet structure develops near the upstream pole and propagates upstream by $\tau = 3.29$.

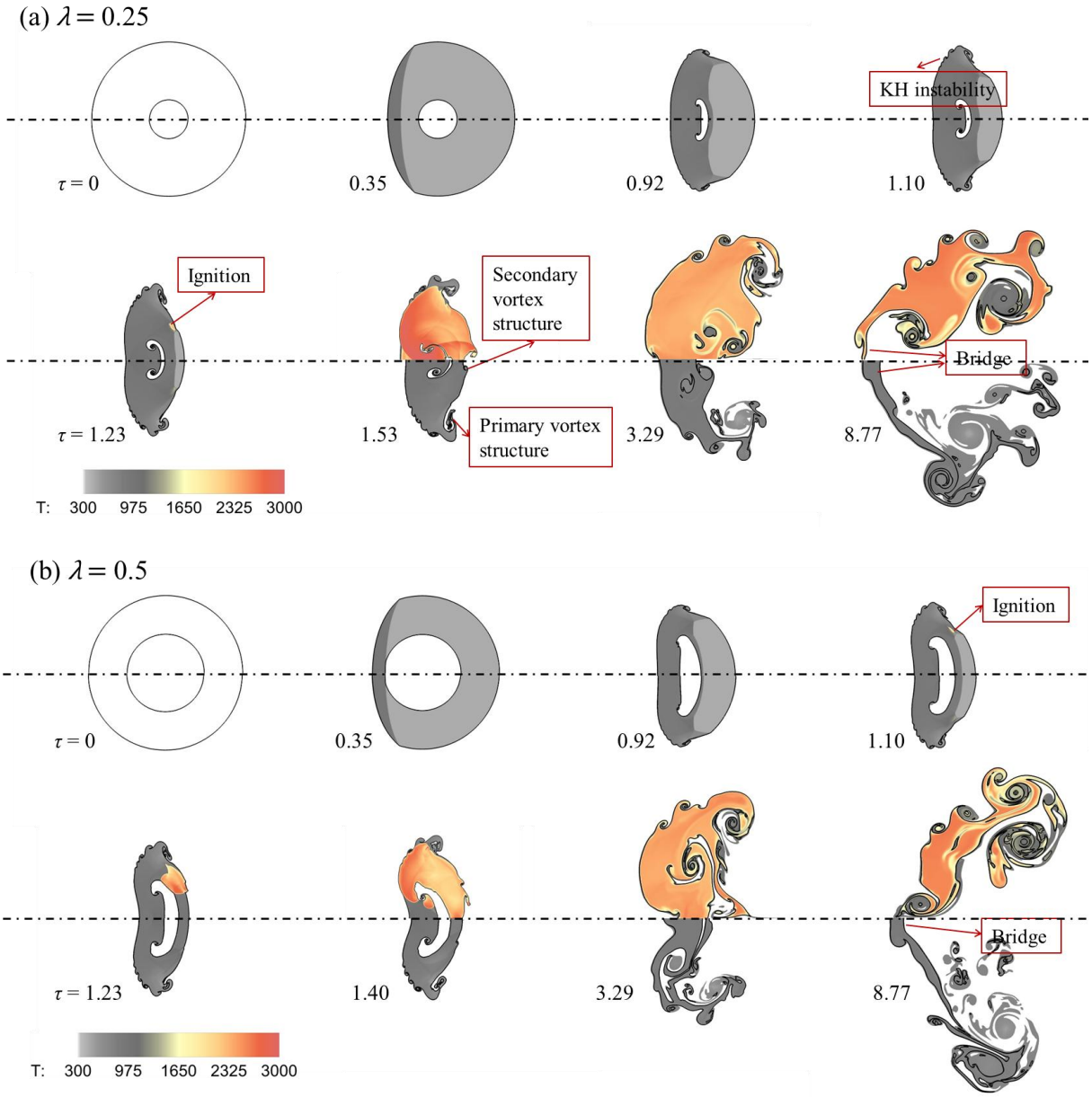

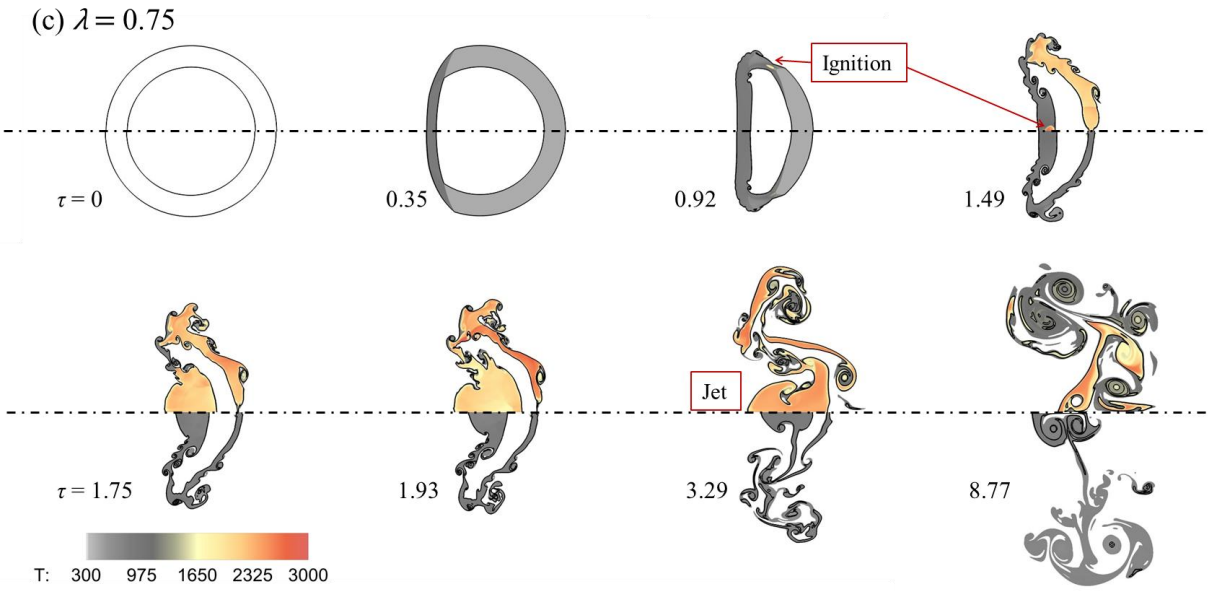

Figure 4-19. Temperature contours for RSBI and ISBI cases with different radius ratios at Mach 2.3, (a) $\lambda = 0.25$, (b) $\lambda = 0.5$, (c) $\lambda = 0.75$. The upper regions depict the reactive scenarios, and the lower regions depict the inert scenarios.

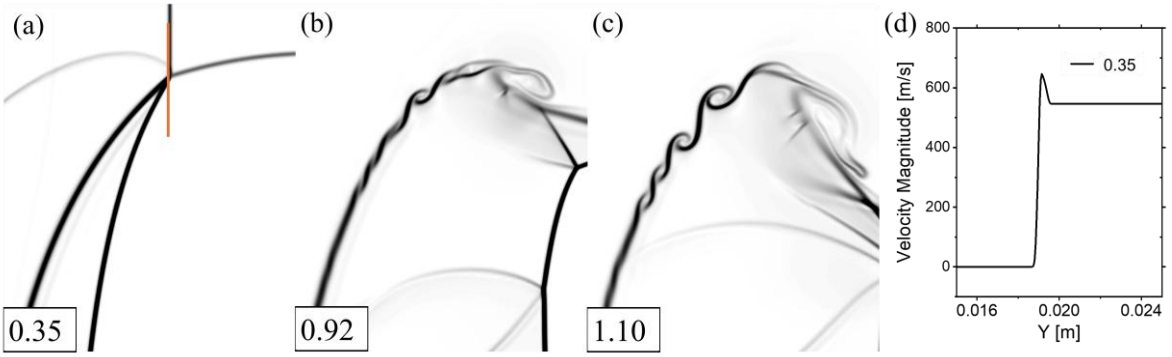

Figure 4-20. Evolution of double-layer gas cylinder with $\lambda = 0.25$ at (a) $\tau = 0.35$, (b) $\tau = 0.92$, (c) $\tau = 1.10$. (d) Velocity magnitude across the outer cylinder following the incident shock at $\tau = 0.35$.

4.4.2. Ignition characteristics

To investigate the process of hot spot generation near DI_1 and identify the types of reaction waves following ignition at different radius ratios, the normalized pressure gradient magnitude *DP* and temperature contours at the moments near hot-spot formation are presented. Figure 4-21 depicts the scenario for $\lambda = 0.25$, where the hotspot formation progresses through two stages of increasing temperature and pressure, consistent with the case of $\lambda = 0.5$. At the first stage ($\tau = 0.75$), TS_1, RS_2, S_1, and FPS are interconnected through

an MS, accompanied by the emergence of two TPs and a localized rise in temperature and pressure. Additionally, the convergence of two shear layers upstream of the MS further amplifies the temperature and pressure, giving rise to the generation of a triangular high-temperature and high-pressure region bounded by the MS and these shear layers. As RS_2 propagates along the direction of TS_1 toward S_2, the collision of two TPs further elevates the temperature and pressure. This results in the formation of a second high-temperature and high-pressure region upstream of the merging shock wave of RS_2 and S_2 at $\tau = 1.11$.

When λ increases to 0.75 Figure 4-23, the first hotspot appears upstream of the Mach stem within the triangular high-temperature and high-pressure region after undergoing the initial stage of amplifying temperature and pressure. The reaction wave transmitted through the inner interface is designated as S_4. When the two S4s collide at the symmetry axis, the RSS_4 is generated with high temperature and pressure. As illustrated in Figure 4-24, RSS_4 moves upstream and transmits through UI_2, forming the $TRSS_4$ at $\tau = 1.40$. As $TRSS_4$ moves upstream, the post-shock temperature increases, resulting in a reduced ignition delay time. The calculated ignition delay time is 2.8 μs, which is shorter than the time for $TRSS_4$ to reach UI_1, leading to the second ignition near UI_2 at $\tau = 1.47$ approximately. After transmitting through DI_2, the detonation wave collides and reflects at the symmetry axis, forming a high-temperature and high-pressure region. This region interacts with UI_2 and propagates toward UI_1 at larger radius ratios, leading to the formation of a second hot spot upstream of UI_2. For smaller radius ratios, the detonation wave generated near DI_1 propagates upstream faster than the reflected reaction wave that forms the high-temperature and high-pressure region, thereby inhibiting the occurrence of the second ignition.

4.4.3. Identification of reaction wave type

To identify the type of reaction wave following ignition, we investigate combustion properties across flame fronts along the yellow lines in Figure 4-21, Figure 4-22, and Figure 4-23. For the scenario with $\lambda = 0.25$, the time sequences of pressure and temperature contours following ignition are captured. As shown in Figure 4-25, the shock waves ignite the combustible mixture upstream of DI_1, leading to the formation of a deflagration wave at t = 55.2 μs. The lower portion of this deflagration front transits into a detonation front, which rapidly propagates towards UI_1 after t = 56.8 μs. Figure 4-26 illustrates the pressure, temperature and radical mass fraction distributions, exhibiting similar trends to those observed in the scenario with λ = 0.5 (see Figure 4-10), which suggests the occurrence of DDT.

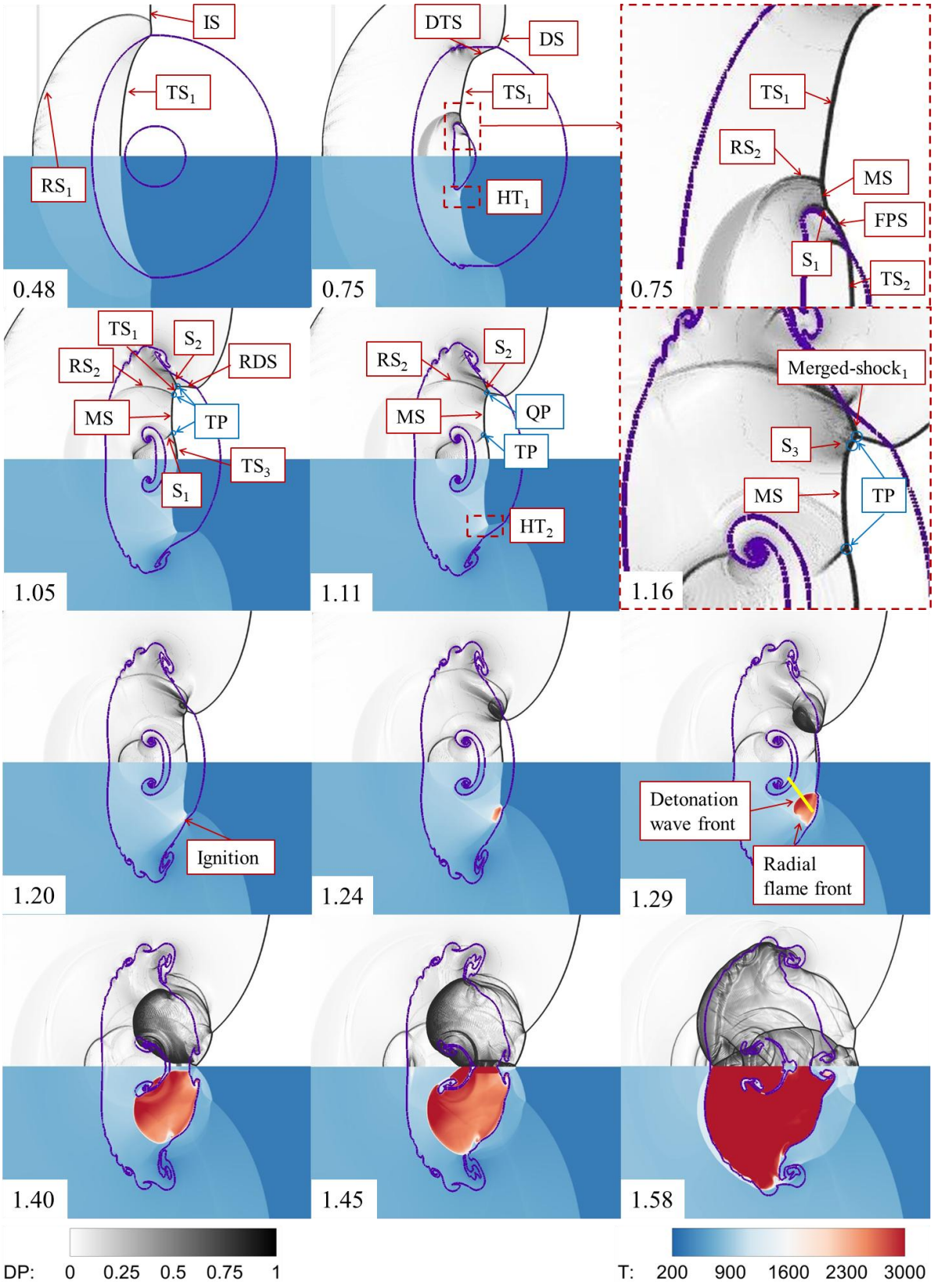

Figure 4-21. Time sequences of the pressure gradient images and temperature contours at the moments surrounding the generation of the hot spot when $\lambda = 0.25$. IS, incident shock wave; TS_1, the first transmitted shock wave; TS_2, the second transmitted shock

wave; TS_3, the third transmitted shock wave; RS_1, the first reflected shock wave; RS_2, the second reflected shock wave; DS, diffracted shock wave; DTS, diffracted transmitted shock wave; FPS, free-precursor shock wave; MS, Mach stem; S_1, S_2, S_3, shock waves; TP, triple point; QP, quadruple point.

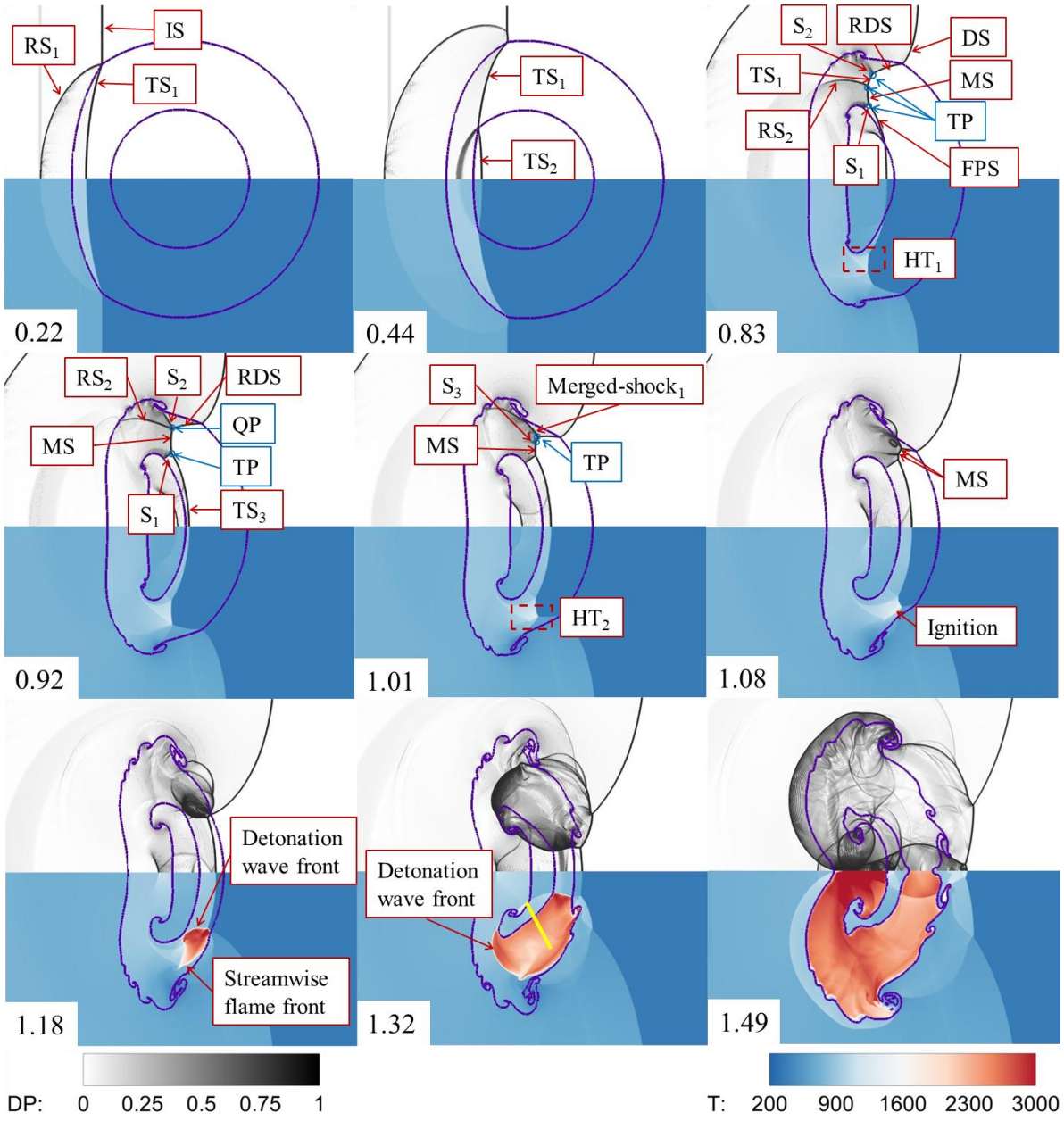

Figure 4-22. Time sequences of the pressure gradient images and temperature contours at the moments surrounding the generation of the hot spot when $\lambda = 0.5$.

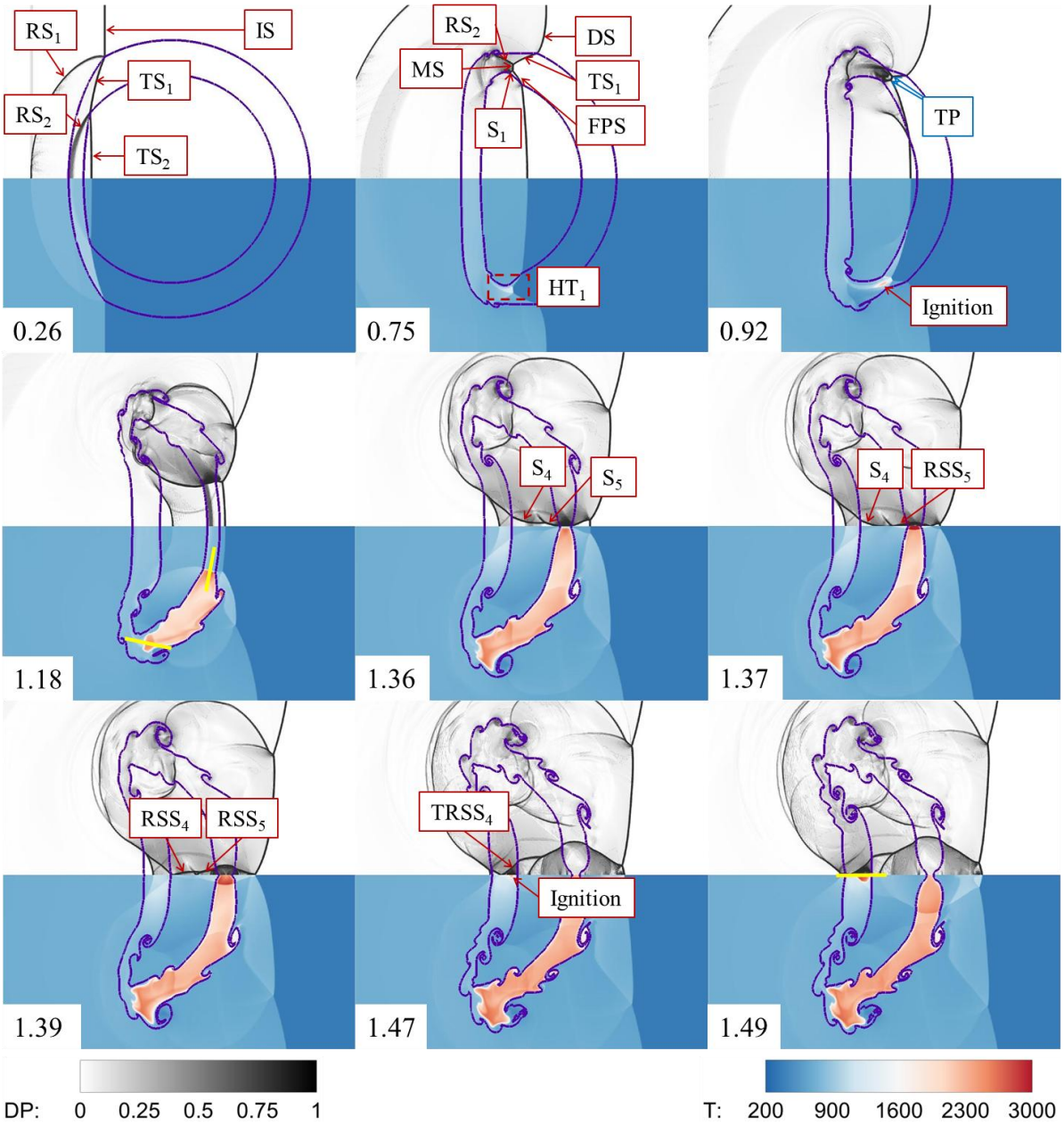

Figure 4-23. Time sequences of the pressure gradient images and temperature contours at the moments surrounding the generation of the hot spot when $\lambda = 0.75$. S_4, S_5, shock waves; RSS_4, reflected S_4; RSS_5, reflected S_5; $TRSS_4$, transmitted reflected S_4.

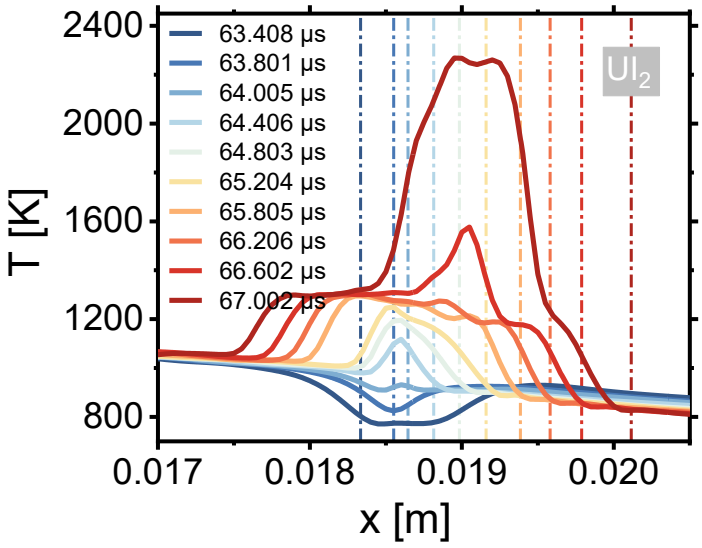

Figure 4-24. Temperature distributions across the symmetry axis at the moment around second ignition for $\lambda = 0.75$. The dash lines represent the UI_2 at different times.

For the case with λ = 0.75, we analyze the pressure, the mass fraction of the radical OH and the product gas H_2O across the fully developed reaction front, as illustrated in Figure 4-27. Following the first ignition at 54.0 μs (see Figure 4-23), the larger radius of the inner inert gas cylinder causes the reaction waves to propagate towards the symmetry axis and UI_1, respectively. For the reaction wave advancing to the symmetry axis, the coupling of an increase in the mass fraction of H and OH with a peak in pressure suggests a detonation wave, resulting in a strong reflected detonation wave from the collision at the symmetry axis within the gas ring. This observation aligns with the pressure and gas composition curves at a Mach number of 2.3 reported in reference [56]. For the reaction wave moving towards UI_1, the mass fractions of H and OH across the reaction front increase while the pressure remains constant, which indicates the presence of a deflagration wave, which is consistent with the observation at Mach 2.13 from the reference [56]. This deflagration wave advances upstream to UI_1 over a longer induction time until the formation of the second hot spot at $\tau = 1.47$. The increase in the mass fractions of H and OH is coupled with the pressure peak, suggesting that the reaction wave is a detonation wave shortly after the second ignition. It rapidly expands in a short induction time and merges with the deflagration front around $\tau = 1.93$ (see Figure 4-19 (c)), leading to a complete reaction within the gas ring.

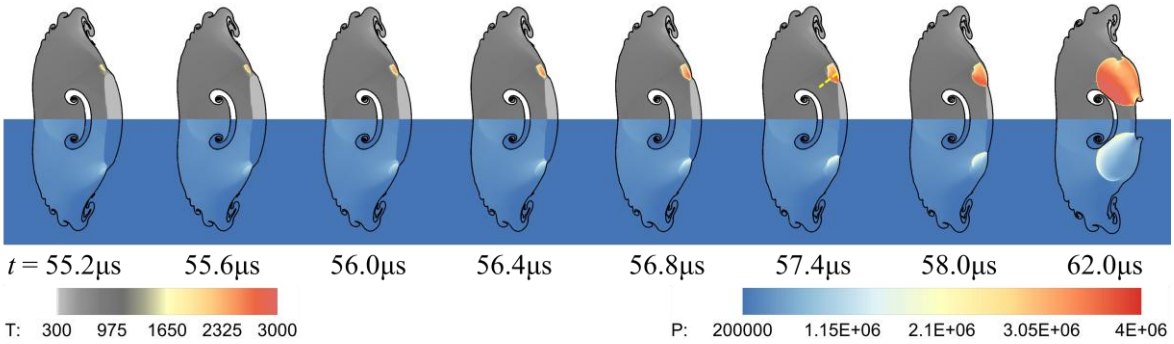

Figure 4-25. Time sequences of the temperature and pressure contours shortly after ignition when $\lambda = 0.25$. The upper regions are temperature contours, and the lower regions are pressure contours.

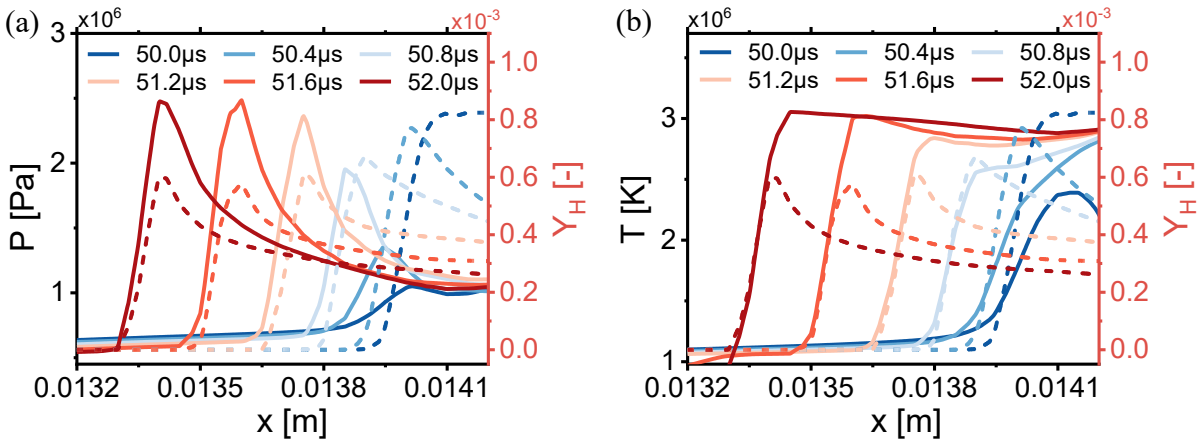

Figure 4-26. (a) Pressure, (b) temperature, and radical H mass fraction across the reaction front during DDT (see yellow dashed line in Figure 4-25) for various time sequences when $\lambda = 0.25$. Solid lines represent the pressure and temperature distributions, dashed lines denote the mass fraction of H.

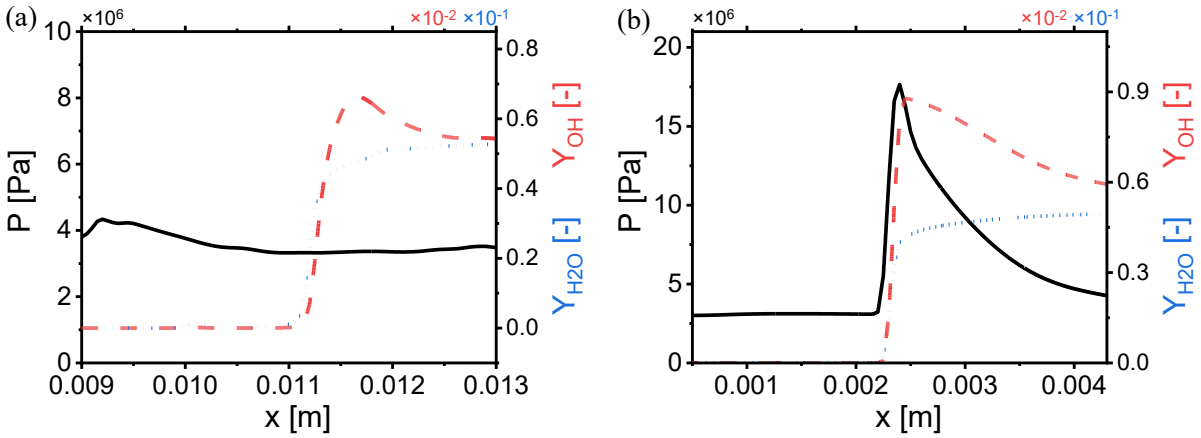

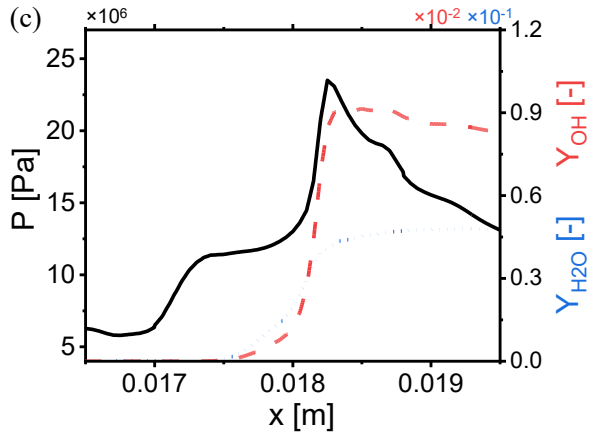

Figure 4-27. Pressure and gas composition across the fully developed reaction front along the yellow lines at (a) τ = 1.18, (b) τ = 1.18, and (c) τ = 1.49 (see Figure 4-23) when λ = 0.75. Solid lines represent the pressure distributions, dashed lines denote the mass fraction of OH and H_2O.

4.4.4. Transverse diameter and area of gas cylinders

4.4.4.1. Transverse bubble diameter

The transverse bubble diameters are normalized by the respective diameters of the outer and inner gas cylinders. For the inner cylinders in Figure 4-28 (a), the interaction between the TS_1 and the UI_2 induces RM instability, leading to the formation of a large-scale primary vortex pair at the diametral plane of the interface. This initially results in a slight growth in the transverse bubble diameter at τ = 0.66, followed by a reduction as λ increases. This behaviour is consistent with the evolution of inert inner gas cylinders at the early stage under various radius ratios in reference [43]. Following the first ignition, the bubble diameter is reduced by the compression of the reaction waves propagating upstream. As λ decreases, the compression of the detonation wave on the diametral plane of interfaces of the inner cylinders becomes more significant, leading to a greater reduction in the radius. After the detonation waves pass through the UI_1, the vortex pairs continue to develop in the diametral plane under the effect of RM instability until the N_2 in the inner cylinder is thoroughly mixed with the gas in the gas ring during the mid-stage of evolution.

For the outer cylinders in Figure 4-28 (b), the morphologies of inert and reactive gas cylinders remain nearly identical before ignition, resulting in similar outer diameters. These diameters remain unchanged until the IS passes over the diametral plane of the interface. As the IS moves through these points, the DS is generated at the outer interface, resulting in compression of the diametral plane of the interface and a decrease of the transverse diameter.

Subsequently, the primary vortex pair continues to develop, causing an increase in the outer diameters. In the inert gas cylinder scenarios, the development of the primary vortex pair of inner cylinders further promotes the expansion of the outer diameters. Over the long-term evolution, the roll-up of the primary vortex pair contributes to the further increase in outer diameters. For the reactive gas cylinders when λ = 0.25 and λ = 0.5, the detonation waves propagate upstream following ignition, reaching the UI_1 within a short induction time. The intense heat release causes the outer cylinders to expand transversely, resulting in a rapid increase up to around 164% in diameter compared to the initial diameter. When λ = 0.75, the deflagration wave has minimal impact on the outer diameters until a second ignition occurs, generating an upstream-propagating detonation wave that subsequently leads to a rapid increase in outer diameter up to 177% of the initial outer diameter compared to inert cases around τ = 4.40. In the long-term evolution, the primary vortex pair fully develops with bubble gas rotating around the vortex cores, resulting in a gradual increase in the transverse diameter of the reactive bubble, which remains smaller than that of the inert cases.

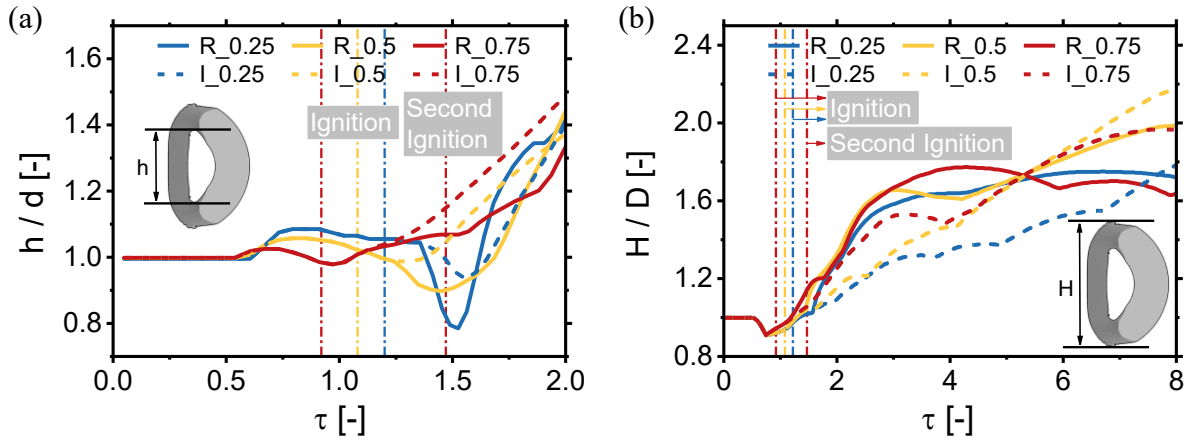

Figure 4-28. Transverse bubble diameters of (a) inner cylinder and (b) outer cylinder for RSBI and ISBI cases.

4.4.4.2. Bubble area

Figure 4-29 shows the areas of the inner cylinder and gas ring, which are normalized by the initial areas of the inner cylinder and gas ring, respectively. The area of the inner cylinder and gas ring is defined as the total area where the mass fractions of N_2v (Y_{N_2V}) and Xe (Y_{Xe}) exceed 0.5, indicating that the grids of $Y_{N_2V} > 0.5$ and $Y_{Xe} > 0.5$ are contained within the inner cylinder and gas ring, respectively.

For the area of the inner cylinder, cases with λ = 0.25 and λ = 0.5 generate an upstream-propagating detonation wave following ignition. As the detonation wave moves over the inner

cylinder, it compresses the DI_2, leading to a reduction in area. In the case where $\lambda = 0.75$, a deflagration wave advances upstream after the first ignition. Due to lower pressure at the reaction front compared to the detonation wave, the variation of area remains unchanged. With the occurrence of the second hotspot near the UI_2, a detonation wave is generated, rapidly causing the upstream area of the gas ring to expand due to its strong heat release and reducing the area of the inner gas cylinder.

For the outer cylinder, the area initially decreases due to compression from IS. The slight volume variation occurs in the inert cases due to the secondary shock reflections. The final bubble area reaches approximately 0.22 for $\lambda = 0.75$, while it stabilizes around 0.41 for $\lambda = 0.25$ and $\lambda = 0.5$. In contrast to the inert cases, the reaction wave greatly dilates the bubble area following detonation, which increased by 173% compared to the inert case. This phenomenon has also been documented in a previous study [58]. The detonation wave generates significantly higher pressure and temperature when compared with the deflagration wave. Consequently, the growth rate of the gas ring area for cases where $\lambda = 0.25$ and $\lambda = 0.5$ is higher than the case where $\lambda = 0.75$. In the latter, the growth rate increases after the second ignition due to a detonation wave being formed. During the long-term stage of evolution, the area of the gas ring decreases for reactive and inert cases due to gas mixing.

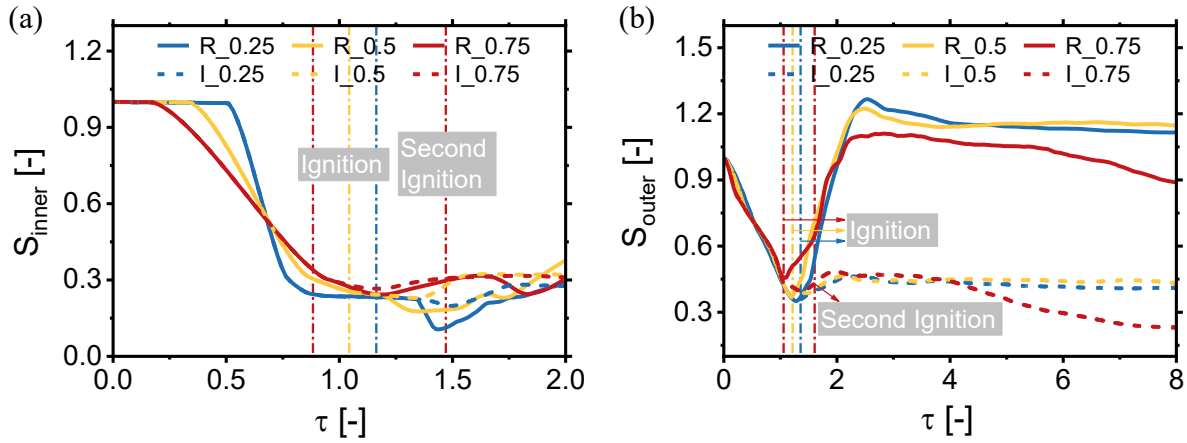

Figure 4-29. Bubble areas of (a) inner cylinder and (b) gas ring for RSBI and ISBI cases.

4.4.5. Combustion completeness

As illustrated in Figure 4-30, the combustion completeness rises rapidly after ignition due to the fast propagation of the reaction wave. For cases where $\lambda = 0.25$ and $\lambda = 0.5$, the detonation wave generated after ignition rapidly propagates toward the upstream interface, resulting in a steeper increase in the combustion completeness compared to the case where λ

= 0.75, where a deflagration wave develops instead. However, a second ignition occurs upstream of UI_2 at τ = 1.47, causing the reaction wave to propagate rapidly as a detonation wave, thereby accelerating the growth of the combustion completeness. After the detonation waves sweep through the entire gas cylinder, the residual reactions proceed slowly towards their equilibrium state, causing combustion completeness to level off eventually. The similar curvatures of combustion completeness are noted in reference [58].

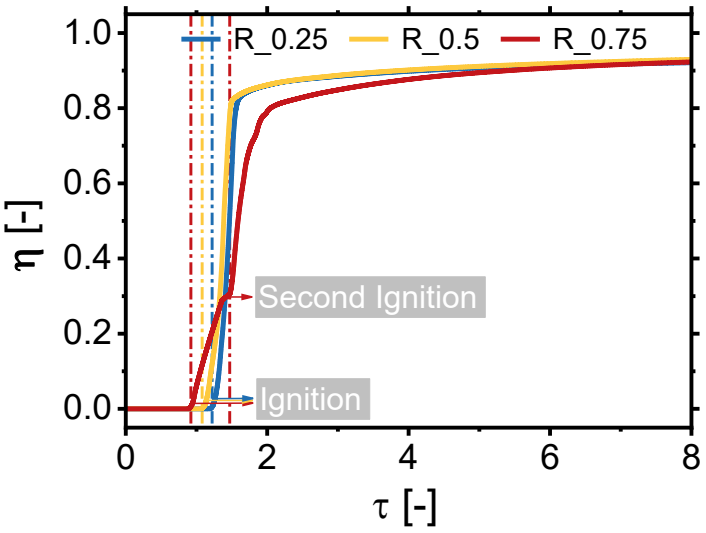

Figure 4-30. Combustion completeness of H_2 for RSBI cases.

4.4.6. Influences of reaction waves on hydrodynamical properties

4.4.6.1. Vorticity transport

Figure 4-31 shows the time sequence of vorticity for both reactive and inert scenarios at various radius ratios. When the IS sweeps through the double-layer gas cylinder, negative vorticity is deposited at the outer interface, while positive vorticity is deposited at the inner interface. The detonation wave propagating upstream carries positive vorticity for cases where λ = 0.25 and λ = 0.5. When it interacts with the inner interface, which aligns with the vorticity orientation, more baroclinic vorticity is deposited on DI_2, accelerating the development of RM instability at the inner interface. After the detonation wave reaches UI_1, which is in the opposite orientation of vorticity, vorticity cancellation occurs, suppressing the KH instability at the interface. When the radius ratio increases to 0.75, the reaction wave propagates toward UI_1 and the symmetry axis as a deflagration wave front and detonation wave front, respectively. As the detonation wave front propagates along the symmetry axis, it interacts with DI_2, which aligns with the vorticity orientation, further enhancing velocity shear and inducing KH instability at the interface (τ = 1.49). Due to the second ignition, the

following detonation wave front propagates upstream through UI_1, suppressing KH instability at the interface and preventing the vortices from aligning along the outer interface.

4.4.6.2. Circulation

Figure 4-32 shows the negative, positive, and net circulation of inert and reactive gas cylinders. Before ignition, the magnitude of negative and positive circulation increases due to the development of secondary KH instability, while the magnitude of positive vorticity rises as a result of RM instability [59]. After ignition, the positive vorticity is deposited at the reaction front. As the reaction front sweeps through the inner interface, additional baroclinic vorticity is deposited, leading to a significant increase in the magnitude of positive circulation compared to inert scenarios. Upon reaching UI_1, the magnitude of positive circulation grows mildly. For reactive gas cylinders with λ = 0.25 and λ = 0.5, the detonation wave with positive vorticity rapidly propagates upstream to reach the UI_1, which suppresses the growth of the secondary KH instability at the interface and results in a slower increase in negative circulation compared to the case with λ =0.75. As time proceeds, the detonation occurs upstream of UI_2 for the λ = 0.75. When this detonation wave acts on the UI_1, it similarly suppresses the development of KH instability and slows down the growth rate of negative circulation. Additionally, the growth rate of positive vorticity for cases where λ = 0.25 and λ = 0.5 is initially higher than that for λ = 0.75 due to the development of the detonation with positive vorticity. Regarding the net vorticity, the rate of decline is slower with increasing radius ratio after ignition.

4.4.6.3. Mixing fraction

Figure 4-33 plots the mixing fraction of reactive and inert gas cylinders among various radius ratios. Since the N_2v in the inner cylinder is well-mixed with the mixture in the gas ring before the mid-stage of evolution, we focus on the mixing fraction of the inner cylinder at this stage. For λ =0.25 and λ = 0.5, it can be observed that the mixing fraction of N_2v in the inner cylinder with the mixture in the gas ring significantly increases compared to the inert gas cylinders. This is due to the detonation wave sweeping across the inner interface, generating more small-scale vortex structures (see Figure 4-19 (a) and Figure 4-19 (b)), which enhances the mixing fraction. When λ = 0.75 (see Figure 4-19 (c)), the shorter distance between the UI_1 and UI_2 allows the TS_1 to quickly act on the UI_2, inducing RM instability at an earlier stage. This promotes the formation of large-scale vortices at the interface, while secondary KH instability further accelerates the development of small-scale vortices. After ignition, the deflagration wave passes over the inner cylinder, disrupting the large-scale

vortex structures but simultaneously increasing the presence of small-scale vortices. Consequently, the difference in mixing fractions between the reactive and inert cylinders is minimal.

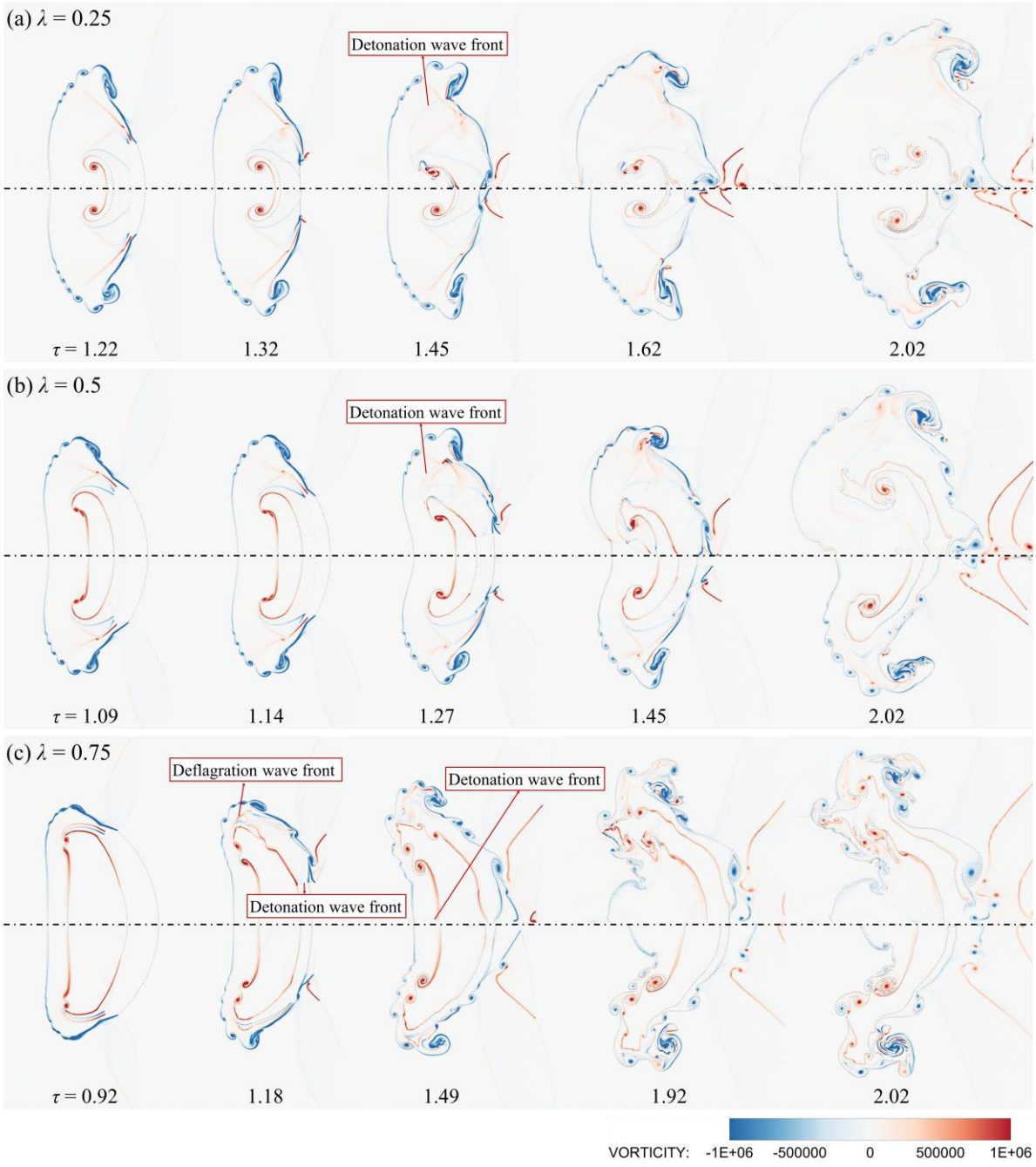

Figure 4-31. Time sequences of vorticity distribution for different radius ratios.

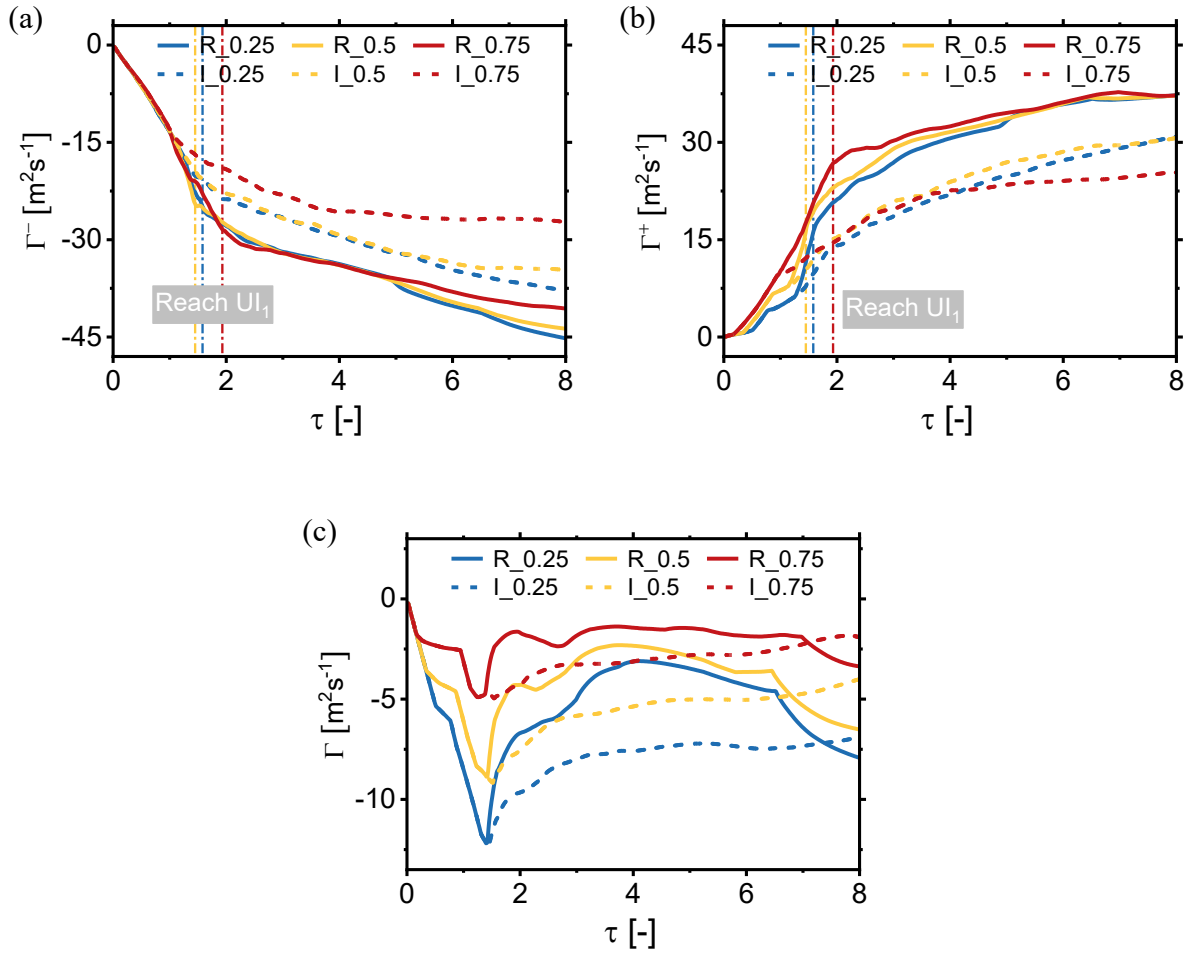

Figure 4-32. The (a) negative, (b) positive, and (c) net component of the circulation for RSBI and ISBI cases.

The mixing fraction between the mixture in the gas ring and the ambient gas is influenced by the reaction wave, which is reduced by 34%−50% for λ =0.25 and λ = 0.5. After ignition, the reaction wave propagates toward UI_1 as a detonation or deflagration wave. The vorticity of the reaction front, having an opposite sign to that of UI_1, affects the mixing in the vortex core region as it sweeps across UI_1. The reduced stretching of bubble gas around the vortex cores at UI_1 leads to a decrease in the mixing fraction. The reaction waves decelerate the growth of secondary instabilities, particularly for smaller radius ratios. The damping of small-scale vortices, as noted in Figure 4-19, accounts for a greater reduction in mixing fractions compared to inert cases. Similar findings have been observed from Diegelmann [56].

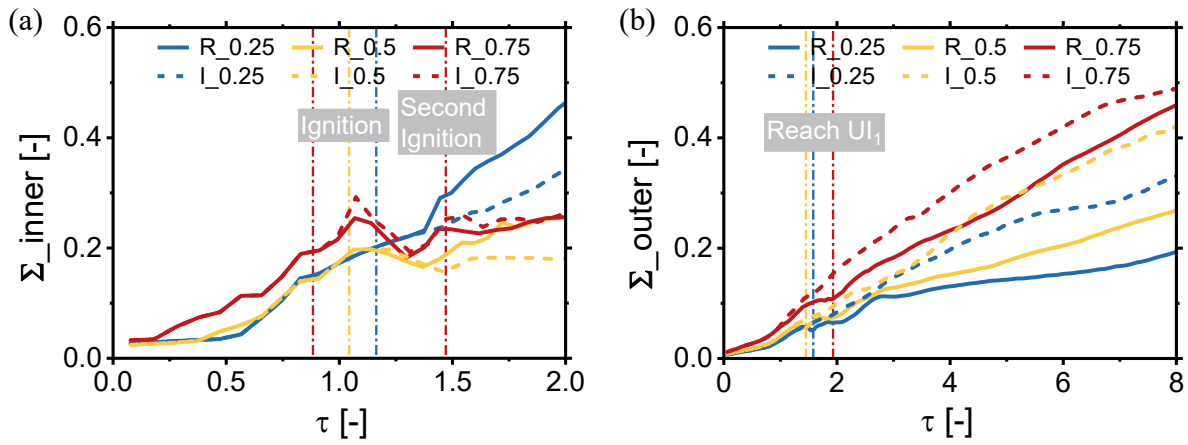

Figure 4-33. Molecular mixing fraction of (a) inner cylinder and (b) outer cylinder.

4.5. Remark

The impacts of initial conditions involving shock intensities and radius ratios on the evolution of the reactive double-layer cylinder are investigated qualitatively and quantitatively.

For the scenarios of shock Mach numbers (M = 2.13, 2.3, 2.5, and 2.9), the temperature contours analysis reveals that when the incident shock traverses the outer cylinder's upstream interface, it induces RM instability, generating primary vortex pairs. Simultaneously, the velocity differences across the equatorial interface produce KH instability. For inert cases, the primary vortex pair is connected by a bridge region in the long-term evolution. However, reactive cases exhibit distinct combustion behaviours: at Mach 2.13, the gas mixture is ignited near DI_1, accompanied by a subsonic deflagration wave. As the Mach number increases, ignition timing advances and location shifts upstream, transitioning to detonation waves that cause rapid outer interface expansion. Notably, at Mach 2.9, the shock waves ignite the gas mixture near the upstream pole of the outer interface. The scenario of Mach 2.13 presents a four-stage hotspot development process with increasing temperature and pressure. For the first stage, TS_1, RS_2, S_1, and FPS are interconnected through a Mach stem, accompanied by the emergence of two TPs and a localized rise in temperature and pressure. Additionally, the convergence of two shear layers upstream of the Mach stem further amplifies the temperature and pressure, giving rise to the generation of a triangular HT_1 and HP_1 region bounded by the Mach stem and the shear layers. When RS2 propagates along the direction of TS_1 toward S_2 until the two TPs collide, further elevating the temperature and pressure, thereby generating the HT_2 and HP_2 region upstream of the merging of RS_2 and S_2. To match the high temperature and pressure of the post Merged-$shock_1$, a shock wave S_3 is formed. S_3

propagates toward S_1 along the direction of the MS, the collision of two TPs giving rise to the HT_3 and HP_3 region. Merged-shock$_2$, TS_3, Merged-shock$_1$, and RDS are interconnected through the Mach stem, accompanied by the emergence of two TPs. The subsequent collision of these two TPs further amplifies temperature and pressure due to complex shock-shock interaction, resulting in the formation of the HT_4 and HP_4 region. Finally, the hotspot occurs in this stage. The hotspot of Mach 2.3 is formed at the second stage, and the hotspot of Mach 2.5 is formed at the first stage. For Mach 2.9, the strong shock wave directly ignites the gas mixture at the upstream pole of the outer interface. Following transmission of the detonation wave through DI_2, the high shock strength leads to immediate ignition of the mixture. DDT can be observed at Mach 2.3 and 2.5. For the outer cylinder, the intense heat release following detonation causes rapid expansion of the gas ring, resulting in a 60% increase in its transverse diameter. However, the hotspot shifts closer to DI_1, which prolongs the induction time required for the detonation front to traverse the gas ring, thereby contributing to the area expansion. In the long-term evolution, the evolution levels off much earlier as the shock strength increases. The ignition process is quantitatively assessed using combustion completeness, where detonation produces a more rapid rise in completeness compared to deflagration. Negative vorticity is deposited at the outer interface while positive vorticity is deposited at the inner interface. Following ignition, both the deflagration and detonation wave fronts generate positive vorticity. However, due to the relatively weak pressure and velocity gradients associated with the deflagration wave, its ability to perturb DI_2 is limited. In contrast, the detonation wave, interacting with the inner interface where has the same vorticity orientation, enhances the development of RM instability and KH instability. When the detonation wave reaches the outer interface, where vorticity is oppositely oriented, vortex cancellation occurs, leading to suppression of interfacial instabilities. As the Mach number increases, the reaction front promotes enhanced mixing at the inner interface. The mixing fraction at the outer interface decreases compared to the inert case after the reactive wave traverses the entire gas cylinder. At the late stage of evolution, the bridge region vanishes under the influence of the detonation wave, which inhibits gradient intensification through rapid straining. Consequently, the mixing fraction is reduced by more than 49% relative to the inert scenario.

For the scenarios of radius ratios (λ = 0.25, 0.5 and 0.75), the spanwise distance between secondary vortex pairs at the outer interface rises with increasing λ. A jet structure forms near the upstream pole of the outer interface during the long-term evolution, replacing the bridge region with inert cases. For reactive cases, ignition occurs earlier near the DI_2 as the radius

ratio increases. At the late stage of evolution, the bridge region disappears and an upstream-propagating jet emerges. Regarding ignition characteristics, the hotspot of $\lambda = 0.25$ and $\lambda = 0.5$ the hotspot forms during the second stage due to cumulative increases in temperature and pressure. For $\lambda = 0.75$, a rapid increase in pressure and temperature at the triple point region leads to the generation of the first hotspot, and the formation of $TRSS_4$ with high temperature and pressure contributes to the appearance of the second hotspot. DDT can be observed in cases where $\lambda = 0.25$ and $\lambda = 0.5$ following the initial ignition. When $\lambda = 0.75$, the detonation wave is constrained by the larger inner cylinder and propagates perpendicular to the symmetry axis. A detonation later reaches UI_1 after the second hotspot is generated. For the outer cylinder, intense heat release following ignition causes substantial transverse expansion, resulting in a more rapid increase in diameter compared to inert scenarios. During long-term evolution, the primary vortex pair fully develops, further increasing the outer diameter, although this increase remains lower than in inert cases. The reaction wave greatly dilates the bubble area following ignition compared to the inert cases. Detonation results in more expansion of the bubble area than deflagration. At the later stages of evolution, the overall area of the gas ring decreases in both inert and reactive cases due to mixing processes. Regarding the mixing fraction, reaction waves inhibit the development of secondary instabilities at the outer interface, particularly at lower radius ratios. The cancellation of small-scale vortices suppresses instability growth, leading to a 34%–50% reduction in mixing fraction compared to inert cases.

CHAPTER 5 Conclusions

This thesis mainly focuses on the application of RM instability involving shock-induced evolution of inert and reactive double-layer gas cylinders. Numerical simulations are conducted using a multi-block parallel finite-volume CFD code based on a reactive compressible multi-component model. To investigate the effects of initial conditions on the evolution and gas mixing of inert double-layer gas cylinders, varying Mach numbers (M = 1.27, 1.5, 1.7, and 2.1) and Atwood numbers with an A/B/A-type gas layer (A_1 = 0.50, 0.39, 0.19, and −0.20) and an A/B/C-type gas layer (A_2 = −0.50, −0.25, −0.06, 0.06 and 0.17) are conducted. For the reactive counterparts, the initial conditions involving shock intensities and radius ratios concerning the subsequent evolution and ignition characteristics for different Mach numbers (M = 2.13, 2.3, 2.5, and 2.9) and radius ratios (λ = 0.25, 0.5 and 0.75) are considered in this work.

For the shock-induced evolution of inert double-layer gas cylinders at different Mach numbers and Atwood numbers:

i. The shock Mach number indicates the intensity of the shock wave, which determines the significance of compressibility. The increased intensity of the IS and TS_1 leads to intense compression on the UI_1 and UI_2. The interaction with intense shock waves leads to a substantial quantity of baroclinic vorticity deposited on the interface, accelerating the generation and development of the vortex pairs. In addition, the jet forms earliest at a Mach number of 2.1, and its length is shorter than other scenarios due to the higher-pressure difference upstream of the jet head after the reflected shock with a high-pressure region in the downstream direction passes through the UI_1. Negative vorticity is deposited at the outer interface, while positive vorticity is deposited at the inner interface. In the long-term evolution, the rolled-up vortical structures become more prominent at higher Mach numbers. The dilatation and baroclinic terms play a dominant role in vorticity production. An increase in Mach numbers amplifies the dilatational term, baroclinic term and viscous term. The summation of the SZ model and PB model provides an accurate prediction of the net circulation, with a relative error is under 2%. Moreover, the summation of the PB model and PB model has a better prediction under the scenarios of higher Mach numbers. For the analysis of mean mass fraction histories, an intense shock wave can promote the mixing of SF_6 and air.

ii. The Atwood number is associated with nonlinear acoustic effects, which quantifies the density ratio between the gas inside the bubble and its surrounding ambient gas. Flow patterns converge as the Atwood numbers exceed 0, while they diverge for negative Atwood numbers.

For the scenario of an A/B/A-type gas cylinder, when $A_1 > 0$, the amount of baroclinic vorticity deposited on the interface of the outer cylinder diminishes, thereby slowing down the development of primary and secondary vortex pairs with decreasing Atwood number. The decrease in the Atwood number contributes to the reduction in the dilatation term, baroclinic term and viscous term. The first peak values of the dilatation term appear due to the generation of vortex pairs and stretched structures around the vortex core. In addition, the summation of the SZ model and PB model has a better prediction of net circulation, where the relative error remains under 3%. When $A_1 < 0$, the flow patterns exhibit different shapes. A vortex pair emerges and propagates in the upstream direction at the upper and lower poles of the outer interface, while another vortex pair moving downstream is generated originating from the DI_2.

The A/B/C-type gas cylinder with different concentrations of SF_6 (ranging from 5% to 80% in volume fraction) in the inner cylinder is constructed to further investigate the dependence of the interface evolution on the Atwood number. In scenarios of $A_2 < 0$, secondary vortex pairs emerge at the downstream interface of the outer cylinder due to a large amount of baroclinic vorticity deposition at the interface following the interaction of a high-pressure triple point with the downstream interface. The distance between secondary vortex pairs decreases as the Atwood number is increased. Conversely, a jet is generated at the downstream interface for positive Atwood numbers. A notably higher-pressure zone is generated after the transmitted shock wave traverses the convergence point due to the convergence of the shock waves. As the transmitted shock wave propagates and collides with the downstream interface, a bulge forms, subsequently giving rise to a jet. Following the passage of the IS over the UI_2, higher magnitudes of Atwood number in the dilatation term, baroclinic term and viscous term are greater than other cases. The summation of the SZ and PB model can predict the circulation of cases where $A_2 > 0$, while the summation of the SZ and PB model or the SZ and SZ model can predict the circulation of cases where $A_2 < 0$. Based on analysis of the mean mass fraction histories of the outer and inner cylinders shows that increased mixing of ambient gas

into the gas ring leads to the dilution of SF_6 and promotes gas mixing as the magnitude of the Atwood number rises, especially when the incident shock wave passes over the gas cylinder.

For the shock-induced evolution of reactive double-layer gas cylinders at different Mach numbers and radius ratios:

i. For the scenarios of shock Mach numbers, the temperature contours indicate that RM instability is induced when the incident shock passes through the UI_1, which leads to the generation of the primary vortex pair. The velocity differences across the equatorial interface also result in the generation of KH instability. For inert cases, primary vortex pairs are connected by a bridge region in the long-term evolution. For reactive cases at Mach 2.13, the gas mixture is ignited near DI_1, initiating a deflagration wave that propagates at subsonic speed. As the Mach number increases, the ignition occurs earlier and shifts upstream, and the onset of a detonation wave leads to a rapid expansion of the outer interface. At Mach 2.9, the shock waves ignite the gas mixture near the upstream pole of the outer interface. As the Mach number increases, the stages involved in amplifying temperature and pressure during hotspot formation are reduced. For Mach 2.9, the strong shock wave directly ignites the gas mixture at the upstream pole of the outer interface. After the detonation wave transmitted through DI_2, the combustible mixture is ignited due to its strong shock intensity. DDT can be observed at Mach 2.3 and 2.5 based on the distributions of pressure, temperature, and radical H mass fraction in the reaction front. Transverse bubble diameter and bubble area are analyzed to quantify the evolution of the gas cylinder. For the outer cylinder, the strong heat release leads to rapid expansion of the gas ring, resulting in a 60% increase in the transverse diameter following detonation. However, the hotspot shifts closer to DI_1, increasing the induction time for which the detonation front sweeps across the gas ring, thereby leading to the most significant expansion in area. In the long-term evolution, the evolution levels off much earlier as the shock strength increases. The ignition process is quantitatively characterized by combustion completeness, with detonation leading to a faster increase in combustion completeness compared to deflagration. Negative vorticity is deposited at the outer interface while positive vorticity is deposited at the inner interface. Both the deflagration and detonation wave fronts generate positive vorticity following ignition. Due to the relatively weak pressure and velocity gradients of the deflagration wave, its ability to perturb DI_2 is limited. In contrast, the interaction between the detonation

wave and inner interface in the same orientation of vorticity accelerates the development of RM instability and KH instability. Upon reaching the outer interface having the opposite vorticity orientation, vortex cancellation leads to the suppression of interface instability. The reaction wave promotes mixing for the inner interface as Mach number increases. The mixing fraction of the outer interface reduces compared to inert counterpart following the passage of the reaction wave over the entire gas cylinder. At the late stage of evolution, the bridge region disappears under the effects of the detonation wave, weakening gradient intensification via rapid straining. As a result, the mixing fraction decreases by more than 49% compared to inert scenarios.

ii. For the scenarios of radius ratios, the spanwise distance between secondary vortex pairs at the outer interface increases with increasing radius ratio. A jet structure is formed near the upstream pole of the outer interface instead of the bridge region during the long-term evolution for inert cases. For reactive cases, ignition occurs earlier near the DI_2 with an increasing radius ratio. At the late stage of evolution, the bridge region disappears, and a jet propagating upstream is generated. For the ignition characteristics, the hotspot of $\lambda = 0.25$ and $\lambda = 0.5$ is formed at the second stage for amplifying temperature and pressure. For $\lambda = 0.75$, a rapid increase in pressure and temperature at the triple point region leads to the generation of the first hotspot, and the formation of $TRSS_4$ with high temperature and pressure contributes to the generation of the second hotspot. DDT can be observed in cases where $\lambda = 0.25$ and $\lambda = 0.5$ after the first ignition. When $\lambda = 0.75$, the detonation wave is constrained by the larger inner cylinder, causing it to propagate perpendicular to the symmetry axis. Subsequently, a detonation propagates to the UI_1 following the second hot spot. Transverse bubble diameter and bubble area are analyzed to quantify the evolution of the gas cylinder. For the outer cylinder, intense heat release after ignition causes a significant transverse expansion, leading to a rapid increase in diameter compared to inert cases. During long-term evolution, the primary vortex pair fully develops, further contributing to the increase in the outer diameters, contributing to the increase in outer diameters, although this increase remains lower than in inert cases. The reaction wave greatly dilates the bubble area following ignition compared to the inert cases. Detonation results in more expansion of the bubble area than deflagration. At the later stages of evolution, the gas ring area decreases for both inert and reactive cases due to gas mixing. Regarding the mixing fraction, the reaction waves decelerate the growth

of secondary instabilities at the outer interface, particularly for smaller radius ratios. The damping of small-scale vortices due to vortex cancellation leads to a 34%−50% reduction in mixing fractions compared to inert cases.

Numerical limitations and future work:

i. Expanding on the research about ISBI scenarios in ICF and scramjet engines, it is observed that an increase in the Mach number and the magnitude of the Atwood number can promote the mixing of different materials, thereby decreasing the energy gain of the inner fuel, which may result in ignition failure. For RSBI scenarios, the mixing fraction between the gas within the gas ring and the surrounding ambient gas decreases accordingly with a reduction in radius ratio and an increase in Mach number, which offers a framework for simulating and optimizing capsule design and scramjet engines. However, the developed model is constrained by the exclusion of the pressure-dependent H_2/O_2 reaction mechanism. Additionally, the 2-D SBI captures the early stage of evolution with good accuracy but deviates in the long-term evolution due to the omission of the vortex-stretching term, which restricts its ability to represent transition phenomena and turbulent mixing in later stages. To address these limitations, future work will incorporate the 3-D model coupled with a detailed chemical mechanism, thereby providing a more comprehensive framework for simulating long-term evolution and predicting ignition performance.

References

[1] R. D. Richtmyer, “Taylor instability in shock acceleration of compressible fluids,” *Commun Pure Appl Math*, vol. 13, no. 2, pp. 297–319, 1960, doi: 10.1002/cpa.3160130207.

[2] E. E. Meshkov, “Instability of the interface of two gases accelerated by a shock wave,” *Fluid Dynamics*, vol. 4, no. 5, pp. 151–157, 1969, doi: 10.1007/BF01015969.

[3] M. Brouillette, “The Richtmyer-Meshkov instability,” *Annu Rev Fluid Mech*, vol. 34, no. 1, pp. 445–468, 2002, doi: 10.1146/annurev.fluid.34.090101.162238.

[4] J. D. Lindl *et al.*, “Erratum: ‘Review of the national ignition campaign 2009-2012’ [Phys. Plasmas 21, 020501 (2014)],” *Phys Plasmas*, vol. 21, no. 12, Dec. 2014, doi: 10.1063/1.4903459.

[5] J. Yang, T. Kubota, and E. E. Zukoski, “Applications of shock-induced mixing to supersonic combustion,” *AIAA Journal*, vol. 31, no. 5, pp. 854–862, 1993, doi: 10.2514/3.11696.

[6] J. Shimoda, T. Inoue, Y. Ohira, R. Yamazaki, A. Bamba, and J. Vink, “On cosmic-ray production efficiency at su0pernova remnant shocks propagating into realistic diffuse interstellar medium,” *Astrophys J*, vol. 803, no. 2, Apr. 2015, doi: 10.1088/0004-637X/803/2/98.

[7] P. E. Dimotakis and R. Samtaney, “Planar shock cylindrical focusing by a perfect-gas lens,” *Physics of Fluids*, vol. 18, no. 3, 2006, doi: 10.1063/1.2186553.

[8] P. A. Thompson, “Compressible-fluid Dynamics,” 1988.

[9] L. F. Henderson, “On the refraction of shock waves,” *J Fluid Mech*, vol. 198, pp. 365–386, 1989, doi: 10.1017/S0022112089000170.

[10] L. F. Henderson, E. G. Puckett, and E. G. Puckett, “On the refraction of shock waves at a slow—fast gas interface,” *J Fluid Mech*, vol. 224, pp. 1–27, 1991, doi: 10.1017/S0022112091001623.

[11] D. Ranjan, J. Oakley, and R. Bonazza, “Shock-bubble interactions,” *Annu Rev Fluid Mech*, vol. 43, pp. 117–140, Jan. 2011, doi: 10.1146/annurev-fluid-122109-160744.

[12] G. H. Markstein and W. Squire, “On the Stability of a plane flame front in oscillating flow,” *J Acoust Soc Am*, vol. 27, no. 3, pp. 416–424, May 1955, doi: 10.1121/1.1907918.

[13] J. F. Haas, “Interaction of weak shock waves with cylindrical and spherical gas inhomogeneities,” *J Fluid Mech*, vol. 181, pp. 41–76, 1987, doi: 10.1017/S0022112087002003.

[14] K. H. A. Winkler, J. W. Chalmers, S. W. Hodson, P. R. Woodward, and N. J. Zabusky, “A numerical laboratory,” *Phys Today*, vol. 40, no. 10, pp. 28–37, 1987, doi: 10.1063/1.881118.

[15] J. M. Picone and J. P. Boris, “Vorticity generation by shock propagation through bubbles in a gas,” *J Fluid Mech*, vol. 189, pp. 23–51, 1988, doi: 10.1017/S0022112088000904.

[16] J. Yang, T. Kubota, and E. E. Zukoski, “A model for characterization of a vortex pair formed by shock passage over a light-gas inhomogeneitv,” *J Fluid Mech*, vol. 258, pp. 217–244, 1994, doi: 10.1017/S0022112094003307.

[17] R. Samtaney and N. J. Zabusky, “Circulation deposition on shock-accelerated planar and curved density-stratified interfaces: models and scaling laws,” *J Fluid Mech*, vol. 269, pp. 45–78, 1994, doi: 10.1017/S0022112094001485.

[18] J. H. J. Niederhaus, J. A. Greenough, J. G. Oakley, D. Ranjan, M. H. Anderson, and R. Bonazza, “A computational parameter study for the three-dimensional shock-bubble interaction,” *J Fluid Mech*, vol. 594, pp. 85–124, Jan. 2008, doi: 10.1017/S0022112007008749.

[19] J. W. Jacobs, “Shock-induced mixing of a light-gas cylinder,” *J Fluid Mech*, vol. 234, pp. 629–649, 1992, doi: 10.1017/S0022112092000946.

[20] J. W. Jacobs, “The dynamics of shock accelerated light and heavy gas cylinders,” *Physics of Fluids A*, vol. 5, no. 9, pp. 2239–2247, 1992, doi: 10.1063/1.858562.

[21] C. Tomkins, S. Kumar, G. Orlicz, and K. Prestridge, “An experimental investigation of mixing mechanisms in shock-accelerated flow,” *J Fluid Mech*, vol. 611, pp. 131–150, 2008, doi: 10.1017/S0022112008002723.

[22] A. Bagabir and D. Drikakis, “Mach number effects on shock-bubble interaction,” 2001.

[23] Z. G. Zhai, T. Si, L. Y. Zou, and X. S. Luo, “Jet formation in shock-heavy gas bubble interaction,” *Acta Mechanica Sinica/Lixue Xuebao*, vol. 29, no. 1, pp. 24–35, Feb. 2013, doi: 10.1007/s10409-013-0003-8.

[24] Y. Zhu, L. Yu, J. Pan, Z. Pan, and P. Zhang, “Jet formation of SF6 bubble induced by incident and reflected shock waves,” *Physics of Fluids*, vol. 29, no. 12, Dec. 2017, doi: 10.1063/1.4996422.

[25] J. Ou, J. Ding, X. Luo, and Z. Zhai, “Effects of Atwood number on shock focusing in shock–cylinder interaction,” *Exp Fluids*, vol. 59, no. 2, Feb. 2018, doi: 10.1007/s00348-018-2492-5.

[26] B. Guan, H. Yang, H. Yang, and G. Wang, “On the irregular jet formation of shock-accelerated spherical heavy gas bubbles,” *Physics of Fluids*, vol. 34, no. 12, Dec. 2022, doi: 10.1063/5.0130382.

[27] E. Fan, B. Guan, C. Y. Wen, and H. Shen, “Numerical study on the jet formation of simple-geometry heavy gas inhomogeneities,” *Physics of Fluids*, vol. 31, no. 2, Feb. 2019, doi: 10.1063/1.5083636.

[28] Z. Deng, B. Guan, D. Li, G. Wang, and B. Zhang, “On the circulation prediction of shock-accelerated polygonal heavy gas cylinders,” *Physics of Fluids*, vol. 36, no. 12, Dec. 2024, doi: 10.1063/5.0243259.

[29] G. I. Taylor, “The instability of liquid surfaces when accelerated in a direction perpendicular to their planes. I,” *Proc R Soc Lond A Math Phys Sci*, vol. 201, no. 1065, pp. 192–196, 1950, doi: 10.1098/rspa.1950.0052.

[30] E. Ott, “Nonlinear evolution of the Rayleigh-Taylor instability of a thin layer,” *Phys Rev Lett*, vol. 29, no. 21, pp. 1429–1432, 1972, doi: 10.1103/PhysRevLett.29.1429.

[31] K. O. Mikaelian, “Richtmyer-Meshkov instabilities in stratified fluids,” *Phys Rev A (Coll Park)*, vol. 31, no. 1, Jan. 1985, doi: 10.1103/PhysRevA.31.410.

[32] M. T. Henry de Frahan, P. Movahed, and E. Johnsen, “Numerical simulations of a shock interacting with successive interfaces using the Discontinuous Galerkin method: the multilayered Richtmyer–Meshkov and Rayleigh–Taylor instabilities,” *Shock Waves*, vol. 25, no. 4, pp. 329–345, Nov. 2015, doi: 10.1007/s00193-014-0539-y.

[33] D. G. Jenkins, D. L. Klein, and R. F. Benjamin, “Nonlinear growth of the shock-accelerated instability of a thin fluid layer,” *J Fluid Mech*, vol. 295, pp. 23–42, 1995, doi: 10.1017/S002211209500187X.

[34] Y. Liang, L. Liu, Z. Zhai, T. Si, and C. Y. Wen, “Evolution of shock-accelerated heavy gas layer,” *J Fluid Mech*, vol. 886, 2020, doi: 10.1017/jfm.2019.1052.

[35] Y. Liang and X. Luo, “On shock-induced heavy-fluid-layer evolution,” *J Fluid Mech*, vol. 920, 2021, doi: 10.1017/jfm.2021.438.

[36] Y. Liang and X. Luo, “On shock-induced light-fluid-layer evolution,” *J Fluid Mech*, vol. 933, Feb. 2022, doi: 10.1017/jfm.2021.1066.

[37] Y. Liang and X. Luo, “On shock-induced evolution of a gas layer with two fast/slow interfaces,” *J Fluid Mech*, vol. 939, May 2022, doi: 10.1017/jfm.2022.213.

[38] Y. Liang and X. Luo, “Hydrodynamic instabilities of two successive slow/fast interfaces induced by a weak shock,” *J Fluid Mech*, vol. 955, Jan. 2023, doi: 10.1017/jfm.2023.3.

[39] Y. Liang and X. Luo, “Shock-induced dual-layer evolution,” *J Fluid Mech*, vol. 929, Dec. 2021, doi: 10.1017/jfm.2021.903.

[40] G. Xiang and B. Wang, “Numerical study of a planar shock interacting with a cylindrical water column embedded with an air cavity,” *J Fluid Mech*, vol. 825, pp. 825–852, Aug. 2017, doi: 10.1017/jfm.2017.403.

[41] W. Wu, B. Wang, and G. Xiang, “Impingement of high-speed cylindrical droplets embedded with an air/vapour cavity on a rigid wall: Numerical analysis,” *J Fluid Mech*, vol. 864, pp. 1058–1087, Apr. 2019, doi: 10.1017/jfm.2019.55.

[42] G. Wang, Y. Wang, D. Li, and B. Guan, “Numerical study on shock-accelerated gas rings,” *Physics of Fluids*, vol. 32, no. 2, Feb. 2020, doi: 10.1063/1.5135762.

[43] L. Feng, J. Xu, Z. Zhai, and X. Luo, “Evolution of shock-accelerated double-layer gas cylinder,” *Physics of Fluids*, vol. 33, no. 8, Aug. 2021, doi: 10.1063/5.0062459.

[44] L. Feng, Z. Zhai, T. Si, and X. Luo, “Eccentric effect on evolution of shock-accelerated double-layer gas cylinder,” *Physics of Gases*, vol. 7, no. 2, 2022, doi: 10.19527/j.cnki.2096-1642.0959.

[45] M. Liberman, “Introduction to physics and chemistry of combustion: explosion, flame, detonation”, *Springer Science & Business Media*, 2008.

[46] J. H. S. Lee, “The detonation phenomenon”, *Cambridge University Press*, 2014.

[47] G. H. Markstein, “Nonsteady flame propagation: AGARDograph”, vol. 75. *Elsevier*, 2014.

[48] G. Thomas, R. Bambrey, and C. Brown, “Experimental observations of flame acceleration and transition to detonation following shock-flame interaction,” *Combustion Theory and Modelling*, vol. 5, no. 4, pp. 573–594, 2001, doi: 10.1088/1364-7830/5/4/304.

[49] G. A. Batley, J. Brindley, and S. A. E. G. Falle, “A Numerical study of the vorticity field generated by the baroclinic effect due to the propagation of a planar pressure wave through a cylindrical premixed laminar flame,” *J Fluid Mech*, vol. 279, pp. 217–237, 1994, doi: 10.1017/S0022112094003897.

[50] Y. Ju, A. Shimano, and O. Inoue, “Vorticity generation and flame distortion induced by shock flame interaction,” *Symposium (International) on Combustion*, pp. 735–741, 1998, doi: 10.1016/S0082-0784(98)80467-0.

[51] E. S. Oran and V. N. Gamezo, “Origins of the deflagration-to-detonation transition in gas-phase combustion,” *Combust Flame*, vol. 148, no. 1–2, pp. 4–47, Jan. 2007, doi: 10.1016/j.combustflame.2006.07.010.

[52] M. Gui, B. Fan, G. Dong, and J. Ye, “Interaction of a reflected shock from a concave wall with a flame distorted by an incident shock,” *Shock Waves*, vol. 18, no. 6, pp. 487–494, Feb. 2009, doi: 10.1007/s00193-008-0177-3.

[53] G. Bakalis, K. C. Tang-Yuk, X. Mi, N. Nikiforakis, and H. D. Ng, “Numerical simulation of deflagration-to-detonation transition via shock–multiple flame kernels interactions,” *Computers and Mathematics with Applications*, vol. 83, pp. 111–126, Feb. 2021, doi: 10.1016/j.camwa.2020.05.016.

[54] N. Haehn, D. Ranjan, C. Weber, J. Oakley, D. Rothamer, and R. Bonazza, “Reacting shock bubble interaction,” *Combust Flame*, vol. 159, no. 3, pp. 1339–1350, Mar. 2012, doi: 10.1016/j.combustflame.2011.10.015.

[55] F. Diegelmann, V. Tritschler, S. Hickel, and N. Adams, “On the pressure dependence of ignition and mixing in two-dimensional reactive shock-bubble interaction,” *Combust Flame*, vol. 163, pp. 414–426, Jan. 2016, doi: 10.1016/j.combustflame.2015.10.016.

[56] F. Diegelmann, S. Hickel, and N. A. Adams, “Shock Mach number influence on reaction wave types and mixing in reactive shock–bubble interaction,” *Combust Flame*, vol. 174, pp. 85–99, Dec. 2016, doi: 10.1016/j.combustflame.2016.09.014.

[57] F. Diegelmann, S. Hickel, and N. A. Adams, “Three-dimensional reacting shock–bubble interaction,” *Combust Flame*, vol. 181, pp. 300–314, 2017, doi: 10.1016/j.combustflame.2017.03.026.

[58] D. D. Li, G. Wang, B. Zhang, Z. B. Wang, and B. Guan, “Geometry effect in reactive shock-elliptic bubble interactions,” *Acta Mechanica Sinica/Lixue Xuebao*, vol. 37, no. 11, pp. 1624–1636, Nov. 2021, doi: 10.1007/s10409-021-01132-9.

[59] E. Fan, J. Hao, B. Guan, C. yung Wen, and L. Shi, “Numerical investigation on reacting shock-bubble interaction at a low Mach limit,” *Combust Flame*, vol. 241, Jul. 2022, doi: 10.1016/j.combustflame.2022.112085.

[60] J. Nuckolls, L. Wood, A. Thiessen, and G. Zimmerman, “Laser compression of matter to super-high densities: thermonuclear (CTR) applications pressure: implosion, ablation,” *Nature*, vol. 239, Sep. 1972, doi: 10.1038/239139a0.

[61] K. A. Brueckner and J. Siebe, “Laser-driven fusion,” *Rev Mod Phys*, vol. 46, no. 2, p. 325, 1974, doi: 10.1103/RevModPhys.46.325.

[62] Y. Zhou, W. H. Cabot, and B. Thornber, “Asymptotic behavior of the mixed mass in Rayleigh-Taylor and Richtmyer-Meshkov instability induced flows,” *Phys Plasmas*, vol. 23, no. 5, May 2016, doi: 10.1063/1.4951018.

[63] J. D. Lindl *et al.*, “The physics basis for ignition using indirect-drive targets on the national ignition facility,” *Phys Plasmas*, vol. 11, pp. 339–491, Jan. 2004, doi: 10.1063/1.1578638.

[64] S. Haan *et al.*, “Point design targets, specifications, and requirements for the 2010 ignition campaign on the national ignition facility,” *Phys Plasmas*, vol. 18, no. 5, 2011, doi: 10.1063/1.3592169.

[65] S. P. Regan *et al.*, “Hot-spot mix in ignition-scale implosions on the national ignition facility (NIF),” *Phys Plasmas*, 2012, doi: 10.1063/1.3694057.

[66] D. S. Montgomery *et al.*, “Design considerations for indirectly driven double shell capsules,” *Phys Plasmas*, vol. 25, no. 9, Sep. 2018, doi: 10.1063/1.5042478.

[67] B. M. Haines *et al.*, “Constraining computational modeling of indirect drive double shell capsule implosions using experiments,” *Phys Plasmas*, vol. 28, no. 3, Mar. 2021, doi: 10.1063/5.0040290.

[68] A. Castrogiovanni, “Review of ‘The Scramjet Engine, Processes and Characteristics,’” *AIAA Journal*, vol. 48, no. 9, pp. 2173–2174, Sep. 2010, doi: 10.2514/1.50210.

[69] T. Shigeyama and K. Nomoto, “Theoretical light curve of SN 1987A and mixing of hydrogen and nickel in the ejecta,” *Astrophys J*, vol. 360, pp. 242–256, 1990.

[70] A. Burrows, “Supernova explosions in the Universe,” *Nature*, vol. 403, pp. 727–733, 2000, doi: 10.1038/35001501.

[71] B. Müller, T. Melson, A. Heger, and H. T. Janka, “Supernova simulations from a 3D progenitor model - Impact of perturbations and evolution of explosion properties,” *Mon Not R Astron Soc*, vol. 472, no. 1, pp. 491–513, 2017, doi: 10.1093/MNRAS/STX1962.

[72] P. A. Gnoffo, R. N. Gupta, and J. L. Shinn, “Conservation equations and physical models for hypersonic air flows in thermal and chemical nonequilibrium”, *National Aeronautics and Space Administration, Office of Management, Scientific and Technical Information Division*, 1989.

[73] J. P. Appleton and K. N. C. Bray, “The conservation equations for a non-equilibrium plasma,” *J Fluid Mech*, vol. 20, no. 4, pp. 659–672, 1964, doi: 10.1017/S0022112064001458.

[74] B. J. Mcbride, M. J. Zehe, and S. Gordon, *NASA Glenn coefficients for calculating thermodynamic properties of individual species*. National Aeronautics and Space Administration, John H. Glenn Research Center at Lewis Field, 2002. [Online]. Available: http://www.sti.nasa.gov

[75] J. W. Buddenberg1 and C. R. Wilke, "Calculation of Gas Mixture Viscosities," *Ind Eng Chem*, vol. 41, no. 7, pp. 1345–1347, 1949, doi: 10.1021/ie50475a011.

[76] S. Chapman and D. Burnett, "The mathematical theory of non-uniform gases: an account of the kinetic theory of viscosity, thermal conduction and diffusion in gases", *Cambridge University Press*, 1990.

[77] P. D. Neufeld, A. R. Janzen, and R. A. Aziz, "Empirical equations to calculate 16 of the transport collision integrals Ω(l,s)* for the lennard-jones (12-6) potential," *J Chem Phys*, vol. 57, no. 3, pp. 1100–1102, 1972, doi: 10.1063/1.1678363.

[78] R. J. Kee, M. E. Coltrin, and P. Glarborg, "Chemically reacting flow: theory and practice", *John Wiley & Sons*, 2005.

[79] B. E. Poling *et al.*, "The properties of gases and liquids", vol. 5. *New York: Mcgraw-hill*, 2001. doi: 10.1036/0070116822.

[80] S. Yungster and K. Radhakrishnan, "Computational study of near-limit propagation of detonation in hydrogen-air mixtures," *38th AIAA/ASME/SAE/ASEE Joint Propulsion Conference & Exhibit*, 2002, [Online]. Available: www.sti.nasa.gov

[81] J. Hao and C. Y. Wen, "Numerical investigation of oxygen thermochemical nonequilibrium on high-enthalpy double-cone flows," *Int J Heat Mass Transf*, vol. 127, pp. 892–902, Dec. 2018, doi: 10.1016/j.ijheatmasstransfer.2018.07.132.

[82] J. Hao, J. Wang, and C. Lee, "Numerical simulation of high-enthalpy double-cone flows," *AIAA Journal*, vol. 55, no. 7, pp. 2471–2475, 2017, doi: 10.2514/1.J055746.

[83] J. Hao, C. Y. Wen, and J. Wang, "Numerical investigation of hypervelocity shock-wave/boundary-layer interactions over a double-wedge configuration," *Int J Heat Mass Transf*, vol. 138, pp. 277–292, Aug. 2019, doi: 10.1016/j.ijheatmasstransfer.2019.04.062.

[84] E. F. Toro, M. Spruce, and W. Speares, "Restoration of the contact surface in the HLL-Riemann solver," *Shock Waves*, vol. 4, pp. 25–34, 1994, doi: 10.1007/BF01414629.

[85] B. van Leer, "Towards the ultimate conservative difference scheme. II. Monotonicity and conservation combined in a second-order scheme," *J Comput Phys*, vol. 14, no. 4, pp. 361–370, 1974, doi: 10.1016/0021-9991(74)90019-9.

[86] S. Gottlieb and C.-W. Shu, “Total variation diminishing Runge-Kutta schemes,” *Math Comput*, vol. 67, no. 221, pp. 73–85, Jan. 1998, doi: 10.1090/S0025-5718-98-00913-2.

[87] Y. Liang and X. Luo, “On shock-induced evolution of a gas layer with two fast/slow interfaces,” *J Fluid Mech*, vol. 939, May 2022, doi: 10.1017/jfm.2022.213.

[88] P. G. Drazin, “Introduction to hydrodynamic stability”, vol. 32. *Cambridge University Press*, 2002.

[89] S. Singh, “Contribution of Mach number to the evolution of the Richtmyer-Meshkov instability induced by a shock-accelerated square light bubble,” *Phys Rev Fluids*, vol. 6, no. 10, Oct. 2021, doi: 10.1103/PhysRevFluids.6.104001.

[90] N. J. Zabusky and S. M. Zeng, “Shock cavity implosion morphologies and vortical projectile generation in axisymmetric shock-spherical fast/slow bubble interactions,” *J Fluid Mech*, vol. 362, pp. 327–346, May 1998, doi: 10.1017/S0022112097008045.

[91] M. A. Liberman, M. F. Ivanov, A. D. Kiverin, M. S. Kuznetsov, A. A. Chukalovsky, and T. V. Rakhimova, “Deflagration-to-detonation transition in highly reactive combustible mixtures,” *Acta Astronaut*, vol. 67, no. 7–8, pp. 688–701, Oct. 2010, doi: 10.1016/j.actaastro.2010.05.024.

[92] P. V Danckwerts, “The definition and measurement of some characteristics of mixtures,” *Applied Scientific Research, Section A*, vol. 3, pp. 279–296, 1952, doi: 10.1007/BF03184936.

[93] D. Olmstead, P. Wayne, J. H. Yoo, S. Kumar, C. R. Truman, and P. Vorobieff, “Experimental study of shock-accelerated inclined heavy gas cylinder,” *Exp Fluids*, vol. 58, no. 6, Jun. 2017, doi: 10.1007/s00348-017-2358-2.